


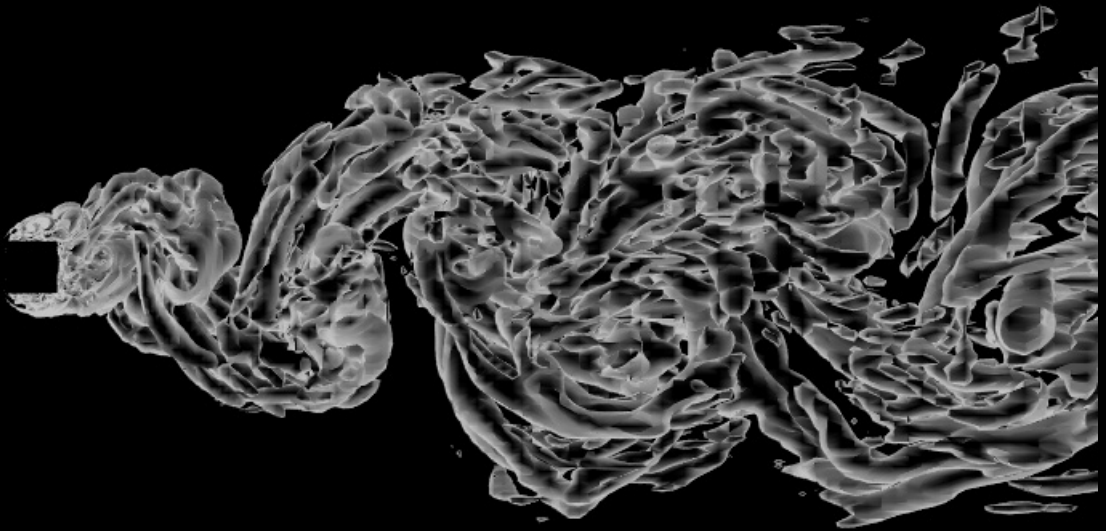


VON KARMAN INSTITUTE FOR FLUID DYNAMICS
ENVIRONMENTAL AND APPLIED FLUID DYNAMICS DEPARTMENT

UNIVERSITY OF TWENTE
FACULTY OF ENGINEERING TECHNOLOGY

UNIVERSITY OF TWENTE 

Large Eddy Simulation of cross-flow around a square rod at incidence with application to tonal noise prediction



Anna Mueller

**LARGE EDDY SIMULATION OF CROSS-FLOW AROUND A
SQUARE ROD AT INCIDENCE WITH APPLICATION TO TONAL
NOISE PREDICTION**

PROEFSCHRIFT

ter verkrijging van
de graad van doctor aan de Universiteit Twente,
op gezag van de rector magnificus,
prof. dr. H. Brinksma,
volgens besluit van het College voor Promoties
in het openbaar te verdedigen
op vrijdag 20 januari 2012 om 16.45 uur

door

Anna Agata Mueller
geboren op 24 september 1978
te Cieszyn, Polen

Dit proefschrift is goedgekeurd
door de promotor:
prof. dr. ir. A. Hirschberg
en de assistent - promotor:
dr. P. Rambaud

University of Twente
Faculty of Engineering Technology

von Karman Institute for Fluid Dynamics
Environmental and Applied Fluid Dynamics Department

Large Eddy Simulation of cross-flow around a square rod at incidence with application to tonal noise prediction

Cover art: Flow over a square rod. Coherent structures, Q criterion.

Thesis presented by Anna Mueller in order to obtain the degree of "Doctor in Engineering", University of Twente, January 2012.

Promoter: Prof. Dr. Ir. A. Hirschberg (University of Twente, Netherlands)

Supervisor: Prof. P. Rambaud (von Karman Institute for Fluid Dynamics, Belgium)

Doctoral Committee:

Prof.dr.ir. H.W.M. Hoeijmakers (University of Twente, Netherlands),
Prof. dr. ir. A. De Boer (University of Twente, Netherlands),
Dr. ir. E.T.A. Van Der Weide (University of Twente, Netherlands),
Prof. dr. ir. I. Lopez Arteaga (Eindhoven University of Technology, Netherlands),
Prof. dr. F. Scarano (Delft University of Technology, Netherlands),
Prof. dr. F. Eising (University of Twente, Netherlands),

A selection of doctoral theses published by the von Karman Institute:

Coupled flow field and heat transfer in an advanced internal cooling scheme
(F. Coletti, University of Stuttgart, October 2010, Germany)

Non-intrusive assessment of transport phenomena at gas-evolving electrodes
(F. Tomasoni, Vrije Universiteit Brussel, Belgium, June 2010)

Dispersion of fine and ultrafine particles in urban environment. Contribution towards an improved modeling methodology for computational fluid dynamics
(C. Górlé, Universiteit Antwerpen, Belgium, February 2010)

Adaptive resolution in PIV image analysis - Application to complex flows and interfaces
(R. Theunissen, Technische Universiteit Delft, The Netherlands & Vrije Universiteit Brussel, Belgium, February 2010)

On Antarctic wind engineering
(J. Sanz Rodrigo, Université Libre de Bruxelles, Belgium, January 2010)

High order discretisation by Residual Distribution schemes (N. Villedieu, Université Libre de Bruxelles, Belgium, November 2009)

Modeling and simulation of dispersed two-phase flow transport phenomena in electrochemical processes
(Th. Nierhaus, VUB, Belgium & RWTH Aachen, Germany, October 15, 2009)

Characterization of a transitional hypersonic boundary layer in wind tunnel and flight conditions
(S. Tirtey, Université Libre de Bruxelles, Belgium, December 2008)

A full catalogue of publications is available from the library

Large Eddy Simulation of cross-flow around a square rod at incidence with application to tonal noise prediction

Keywords: square cylinder, square rod, angle of attack, tonal sound, Computational Aero-acoustics, Large Eddy Simulation

©2011 by Anna Mueller
D/2011/0238/585, T. Magin, Editor-in-Chief

Published by the von Karman Institute for Fluid Dynamics with permission.

All rights reserved. Permission to use a maximum of two figures or tables and brief excerpts in scientific and educational works is hereby granted provided the source is acknowledged. This consent does not extend to other kinds of copying and reproduction, for which permission requests should be addressed to the Director of the von Karman Institute.

ISBN 978-2-87516-022-5

Contents

1	Introduction	1
1.1	Goal of the thesis	1
1.2	Framework	3
1.3	Outline of the thesis	4
2	Flow around square rod at incidence - literature review	5
2.1	Definitions	5
2.1.1	Nondimensional parameters	5
2.2	Critical angle of attack α_{cr} and flow regime classification	7
2.2.1	Value of critical angle of attack α_{cr}	13
2.3	Flow in the wake	13
2.3.1	Instantaneous flow visualisations	13
2.3.2	Average flow pattern	13
2.4	Pressure on the rod surface at different angles of attack	13
2.5	Lift and drag coefficients	15
2.5.1	Average lift and drag coefficients at different angles of attack	15
2.5.2	Oscillating lift and drag coefficients at different angles of attack	18
2.6	Sound produced by a square rod at incidence	20
2.7	Conclusion	22
3	Flow modeling based on LES	25
3.1	Governing equations	25
3.1.1	DNS	25
3.1.2	u-RANS	26
3.1.3	Large Eddy Simulation formulation	27
3.2	Model Problem	30
3.2.1	Blockage effects	30
3.2.2	Grid topology	31
3.2.3	Boundary conditions	31
3.2.4	Discretisation	33
3.2.5	Experiment at UTwente	34

3.3	The influence of wall resolution and use of wall functions . . .	34
3.3.1	Parameters for the study of wall mesh refinement . . .	37
3.3.2	Discussion of Numerical Results	38
3.3.3	Conclusion	39
3.4	The influence of domain size in spanwise direction	44
3.4.1	Study parameters	44
3.4.2	Discussion of Numerical Results	44
3.4.3	Conclusion	49
3.5	The influence of end-plates and their wall resolution	51
3.5.1	Study parameters	51
3.5.2	Discussion of Numerical Results	51
3.5.3	Conclusion	56
3.6	General conclusion	56
4	Flow around square rod at incidence - LES results and comparison with PIV	61
4.1	Computational model	62
4.1.1	Mesh & near wall resolution	63
4.2	Average flow	64
4.3	Flow statistics	66
4.4	Instantaneous flow pattern	67
4.5	Conclusion	88
5	Aerodynamic tonal sound generated by square rod at incidence - experiment and numerical prediction	89
5.1	Introduction	89
5.2	Experimental set-up	91
5.3	Numerical simulations	95
5.4	Flow properties	97
5.4.1	Steady flow	97
5.4.2	Steady Pressure	98
5.4.3	Two wake modes	100
5.4.4	Mean lift and drag	102
5.4.5	Fluctuating part of lift and drag	102
5.5	Sound propagation - theory	115
5.6	Sound pressure level	119
5.7	Conclusion	124
5.7.1	Flow prediction	124
5.7.2	Tonal noise	125
5.7.3	General conclusion	125

6 Concluding remarks	127
Bibliography	131
Glossary	137
Summary	143
Curriculum Vitae	145
Aknowledgements	147

Chapter 1

Introduction

1.1 Goal of the thesis

The flow around bluff bodies such as cylinders or rods in cross-flow is intrinsically unstable at high Reynolds numbers found in industrial installations. Practical examples are fences (architectural engineering), cables in suspended bridges (civil engineering), landing gears (aeronautical engineering), train pantographs (automotive) and heat exchanger pipe bundles (process engineering and energy conversion) [11, 12].

The flow instability leads to fluctuations in the aerodynamic forces. In most cases this phenomenon is dominated by periodic vortex shedding, which is coherent with the structure's axis orthogonal to the flow over distances of several reference lengths. The vibrations that result from these oscillating forces are a threat to the mechanical integrity of the structures. Moreover, the unsteadiness of the flow generates acoustic waves, which is an environmental nuisance.

There is a substantial interest in predicting such phenomena during the design phase by means of numerical simulations. The main goal of the present project is to predict the sound radiated by the flow over a simplified bluff-body model in order to evaluate a possible methodology to use in industrial applications. As a simplified model we use a rod with square cross section in a uniform cross flow. We solved the problems using a commercial off-the-shelf software and moderate computing power. Our aim is to identify the most crucial model parameters that make these simulations industrially applicable.

The aerodynamicists are mostly interested in the source region and near field where the lift and drag forces are acting. This, at high Reynolds numbers, requires highly refined meshes close to the body surface to resolve the near-wall viscous layers. Aeroacousticians, on the contrary, are mainly interested in the far-field sound level. Together these requirements lead to very large computational domains. At low Mach numbers the computa-

tional domain should be several times the typical wavelength. For issues of computational cost, Direct numerical solution (DNS) of the compressible Navier-Stokes equations is limited to low Reynolds numbers and large Mach numbers. Therefore we consider Large Eddy Simulation (LES), which combines direct simulation at large scales with a sub-grid turbulence model for small scales. This allows reaching larger Reynolds numbers for the same computational cost. Still a direct prediction of the sound radiation involves a very large computational effort. Such compressible flow simulation involves advanced higher order numerical integration schemes that minimize damping and dispersion of propagating acoustic waves. Moreover, avoiding spurious numerical sounds and instabilities in those methods poses a very big challenge. Numerical boundaries also necessitate special attention to avoid acoustic reflections or spurious sound generation by vortical structures.

We are interested in the sound observed at large distances from the source compared to the wavelength. Very large calculation domains are needed to predict this far field radiation at low Mach numbers corresponding to large wave length compared to the rod diameter. However the low Mach number and large wave length imply that the flow is locally incompressible in the source region where non-linear effects are dominant. We therefore consider a hybrid approach in which the flow in the source region is assumed to be incompressible. We limit the LES calculations to this relatively small region around the rod. We assume that the feedback influence of acoustic waves on the flow is negligible. The sound radiation is estimated analytically by means of the aeroacoustical analogy of Lighthill [37, 38] as implemented by Curle [15]. Our aim is to assess the potential of commercially available software as currently used in industry. The LES simulation method used is the one implemented in Fluent [1]. Originally we also explored the DNS potential of Fluent [42] at very low Reynolds numbers. We however soon left this option as too costly for the Reynolds numbers present in industrial applications. One of the main questions is whether a two dimensional model would be sufficient. In the LES we considered the option of quasi-two dimensional flow in which a slice of a few rod diameters' thickness is considered bounded laterally by periodic boundary conditions. The key idea is to obtain a high resolution of the flow in the viscous boundary layers near the walls without extremely large grids. In industry it is common practice to go one step further: the so called Reynolds Averaged Navier-Stokes approximation is used. When using a two dimensional computational domain the numerical simulations become quite accessible compared to three dimensional incompressible LES. We therefore compare our results with the unsteady RANS option (uRANS).

We restrict ourselves to the prediction of the dominating periodic sounds (whistling). The same approach can be used to predict broad band noise, but this is more difficult as it involves much lower sound levels and more extreme frequencies. This subject is left for further research.

Since the pioneer work of Strouhal in 1878 [59] most of the attention has focused on cylinders with circular cross sections. We consider here the rod with a square cross section. This geometry is a generic model for rods used widely in civil engineering. We limit ourselves to rods with sharp edges. In this case flow separation obviously remains fixed at these edges. This makes flow prediction easier than for flow separation from smooth surfaces. However we observe complex flow behavior such as reattachment and secondary flow separation, which are strongly dependent on the turbulence. This depends strongly on the angle of attack of the cross flow relative to the side walls of the rod. Predicting such phenomena is another goal of our project.

1.2 Framework

The present work has been carried out within the framework of the European project Aether (Marie Curie project MRTN-CT-2006-035713). The project aims at strengthening the fundamental scientific work in the multidisciplinary engineering field of aero- and thermo-acoustical coupling in energy conversion processes. This means promoting innovative designs for production of energy at low cost and low pollutant levels. Evaluating the potential of commercial LES for prediction of noise production is part of this project.

The Aether network is composed of six universities (Instituto Superior Técnico, Lisbon; Katholieke Universiteit Leuven; Luleå University of Technology; Technische Universiteit Eindhoven; Technische Universität München; University of Cambridge), three research centres (Centre Européen de Recherche et Formation Avancée en Calcul Scientifique-CERFACS, TNO Science and Industry, von Kàrmàn Institute for Fluid Dynamics) and five industrial partners (Arcelor Steel Belgium N.V., Alstom Switzerland Ltd., Gasunie Engineering and Technology, LMS Internal, Rolls-Royce plc.). The project was coordinated by Dr. C. Schram of LMS.

The work at the VKI has been initiated under the supervision of Dr. J. Anthoine. The numerical work has been carried out at the von Kàrmàn Institute (VKI) under daily supervision of Dr. P. Rambaud. The LES simulations have been carried out on a cluster financed by LMS. The uRANS calculations used as reference have been provided by Dr. E. van der Weide

of the University of Twente (UT). The PIV data of Roosenboom [52] obtained in the group of prof. F. Scarano at the Technische Universiteit Delft (TUDelft) has been used for comparison of the flow predicted by the LES and uRANS calculations. The static wall pressure measurements and acoustic radiation measurements have been carried out by Dorneanu [16] in the silent wind tunnel of UT under supervision of prof. A. Hirschberg.

1.3 Outline of the thesis

Chapter 2 of the thesis provides a review of literature on the flow around a square rod placed in cross flow at various angles of attack. This is the angle between the incoming uniform flow and the side wall of the rod. Chapter 3 describes the LES and uRANS methods used. For the particular case of zero angle of attack, a study of the effect of various numerical parameters in the LES calculation is carried out. In particular we consider the use of a coarse mesh at the walls of the rod in combination with a so called “law of the wall” [56]. This corresponds to a non-resolved LES. In order to reduce the calculation costs, a quasi-two dimensional approach is evaluated in which we consider a limited length of the rod bounded by lateral periodic boundary conditions. In the case of a cavity flow Larchevêque et al. [36] observed that periodic lateral boundary conditions promoted the so-called cavity periodic vortex shedding mode. This mode is not observed when the more realistic side-wall boundary conditions are used. We observe then a shear layer oscillation mode. In the case of the rod, side-walls are used to hold the rod in the flow. Based on this numerical study a numerical model is chosen. The LES calculations are carried out at Reynolds 5000 for three angles of attack (0° , 13° , 45°), which correspond to interesting cases identified in chapter 2. The predicted flow is compared in detail with the PIV data of Roosenboom [52] in chapter 4. In chapter 5 the static wall pressure measurement and acoustical radiation measured by Dorneanu [16] are compared with the numerical results and data from the literature. This includes lift coefficients and the dominating vortex shedding frequency characterized by a Strouhal number. Chapter 6 provides an overview of our main conclusions.

Chapter 2

Flow around square rod at incidence - literature review

Bluff body wake flows are of significant engineering interest. The aerodynamic forces acting on a bluff body are correlated with the properties of the wake. The alternate vortex shedding in the near wake leads to large fluctuating pressure forces in a direction transverse to the flow and may cause structural vibrations, which under certain conditions can cause damage of the structure. Associated flow-induced noise can be a significant nuisance. Understanding the interdependence between the geometry, the wake and the forces exerted on a body is very important and has been extensively studied over many years [13, 19, 24, 26, 33, 45, 60, 64]. We focus on a square rod as a generic geometry. In this chapter we present a literature review of experimental and numerical studies of square rod placed in the cross-flow.

The authors who report the experimental mean lift and drag coefficients in function of angle of attack α are: Vickery [64], Igarashi [26], Knisely [33], Norberg [45], Chen [13], Tamura [60], Dutta [19], Roosenboom [52]. There are considerably less numerical studies reporting varying angle of attack and solving the details of the turbulent flow. In an early paper Taylor [61] presents numerical results obtained using a discrete vortex method.

At zero angle of attack there is an extensive ERCOFTAC database available for Laser Doppler Velocimetry (LDV) measurements at $Re_D = U_o D / \nu = 22000$ by Lyn [39]. This is now the main benchmark test case for testing numerical solvers, see for example Rodi [51] and Sohankar [58].

In the present chapter we discuss these data, focusing on the aspects which will be considered in the following chapters.

2.1 Definitions

2.1.1 Nondimensional parameters

We use the following non-dimensional numbers:

- Reynolds number Re_D - it characterises the ratio of inertia force to viscous forces in the bulk of the flow and in consequence quantifies the relative importance of these two types of forces. It is based on the upstream mean velocity U_o and the rod width D :

$$Re_D = \frac{\rho U_o D}{\mu} \quad (2.1)$$

In majority of LES cases solved in this work $Re_D = 5000$ was used.

- Strouhal number St_D - is a non-dimensional parameter measuring the ratio of characteristic length to distance travelled during an oscillation period T . It is used when analysing oscillating unsteady flow problems.

$$St_D = \frac{fD}{U_o} \quad (2.2)$$

where f is the dominating frequency

- Pressure coefficient C_p - it describes the relative pressure in each point of the flow.

$$C_p = \frac{p - p_o}{\frac{1}{2}\rho U_o^2} \quad (2.3)$$

where subscript $_o$ values correspond to upstream pressure and velocity.

- Correlation coefficient γ - the peak value of coherence as a function of spanwise separation can be fitted with gaussian distribution. The value of parameter γ is determined as a width of the gaussian curve at level 0.5 divided by the rod width D .

The total force component F_i on a wall along the specified direction n_i is computed by summing the projection of the pressure and viscous forces on each face on that direction. The direction $i = 1$ corresponds to the main flow direction. Direction $i = 2$ is normal to $i = 1$ and to the axis $i = 3$ of the rod. When $i = 1$ we speak about drag, when $i = 2$ the force is called lift.

$$F_i = \vec{n}_i \cdot (\vec{F}_v + \vec{F}_p) \quad (2.4)$$

We distinguish here the force \vec{F}_v due to the viscous shear stress and force \vec{F}_p due to the pressure. Formally, both types of wall forces are due to viscosity: if the body was moving through an inviscid fluid there would be no drag at all. Pressure forces are the result of symmetry breaking due to flow separation. Flow separation is a viscous phenomenon. Frictional (viscous) force is

important for attached flows, and it is related to the surface area exposed to the flow. Pressure (form) force is important for separated flows, and it is related to the cross-sectional area of the body. We furthermore distinguish the force normal the flow, which is called the lift force $(0, F_2, 0)$ and the drag force in the flow direction $(F_1, 0, 0)$.

- Coefficient of drag Cd - is a dimensionless quantity that is used to quantify drag

$$Cd = \frac{F_1}{\frac{1}{2}\rho U_0^2 DL}, \quad (2.5)$$

where L is the rod length

- Coefficient of lift Cl - is a dimensionless quantity that is used to quantify lift

$$Cl = \frac{F_2}{\frac{1}{2}\rho U_0^2 DL}, \quad (2.6)$$

It has to be stressed that throughout this thesis all the non-dimensional numbers are related to width D of the rod and not to the effective width of the area facing the flow (area projected on a surface normal to $i = 1$). The data from literature is often scaled on the projected area. When necessary we rescaled it to D .

The root mean square (*rms*) values of Cl and Cd are calculated using the Parseval theorem. We integrate the Power Spectrum Distribution (PSD) for the full frequency content of the signal.

2.2 Critical angle of attack α_{cr} and flow regime classification

The definitions of angle of attack α and coordinate system can be seen in figure 2.1. The global coordinate system (x_1, x_2, x_3) is placed in the center of a square rod of width D . The third axis x_3 , along the rod axis, follows the right hand rule. The local coordinate system (x'_1, x'_2, x'_3) rotates with the rod. The angle of attack α is the angle between direction x_1 and the direction x'_1 normal to the rear face D of the rod. Flow around such a square rod at angle of attack α was classified by Igarashi [26] into four flow patterns that depend on angle of attack α :

- I - $0^\circ < \alpha < 5^\circ$ - perfect separation symmetric flow,

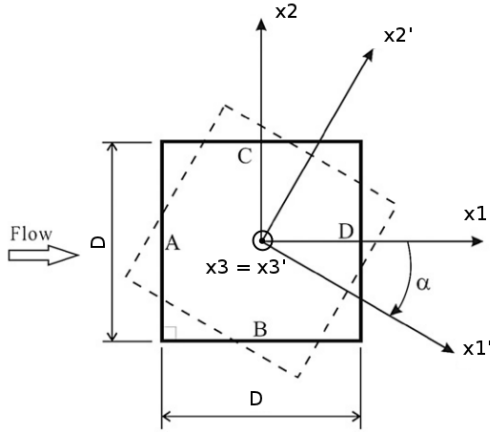


Figure 2.1: Definition of angle of attack α and rod dimensions. D is the rod width. (x_1, x_2, x_3) is the global coordinate system. (x'_1, x'_2, x'_3) is the local coordinate system associated with the rod. Solid line, $\alpha = 0^\circ$, dashed line $\alpha > 0^\circ$. A - leading face, B - lower face, C - upper face, D - rear face.

- II - $5^\circ < \alpha < \alpha_{cr}$ - perfect separation asymmetric flow,
- III - $\alpha_{cr} < \alpha < 35^\circ$ - reattachment flow type,
- IV - $35^\circ < \alpha < 45^\circ$ - wedge flow type.

Igarashi [26] measured the fluctuating pressure coefficients $Cp' = p'/0.5\rho U^2$ at the midpoints of the side (C) and rear (D) faces of the rod (see figure 2.2). The fluctuating pressure coefficient Cp' decreases from a high initial value at $\alpha = 0^\circ$ to a minimum value for $10^\circ < \alpha < 15^\circ$. In that region a critical value of the angle of attack $\alpha = \alpha_{cr}$ is observed for which Cp' has a minimum. Cp' on the side face is increasing monotonically with increasing α for angles $15^\circ < \alpha < 45^\circ$. The Cp' is substantially higher on side face than on the rear face for $\alpha < 5^\circ$. One can observe a higher pressure fluctuation on rear face with respect to the side face for angles $\alpha > 15^\circ$.

Huang [24] gives in his review the following classification merging the two first groups of Igarashi [26] into a single one:

- Subcritical flow - $0^\circ < \alpha < \alpha_{cr}$ - stagnation point at the leading face, two separation points (at the leading edges). Alternating vortex

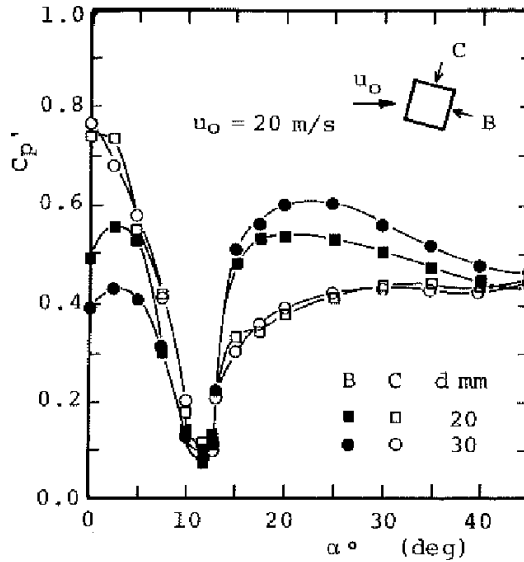


Figure 2.2: $C_{p'}$ at the midpoints of the side and rear faces vs. angle of attack α measured by Igarashi [26]. Squares $Re_D = 27000$, circles $Re_D = 41000$

shedding in the wake.

- Supercritical flow - $\alpha_{cr} < \alpha < 45^\circ$ - stagnation point is still at the leading face shifted downwards in direction of the lower edge. Most of the times a recirculation bubble is formed at the upper face. The reattachment is particularly strong around $\alpha = \alpha_{cr}$ separating the subcritical from supercritical regime.
- Wedge flow - $\alpha = 45^\circ$ - flow bifurcation at the leading edge, the flow follows the rod surface and separates at the top and bottom edges. This configuration is very sensitive to deviation from the symmetrical setting of the angle and possible inflow non-uniformity.

Sketches of the two-dimensional flow patterns in those groups can be seen in figure 2.3. Locations of separation and reattachment of the boundary layer on the rod surface can be identified by examining the positions of accumulated oil strips on the rod surface. In the experiment of Huang [24], those are the dark-blue traces whose normalised locations can be seen in

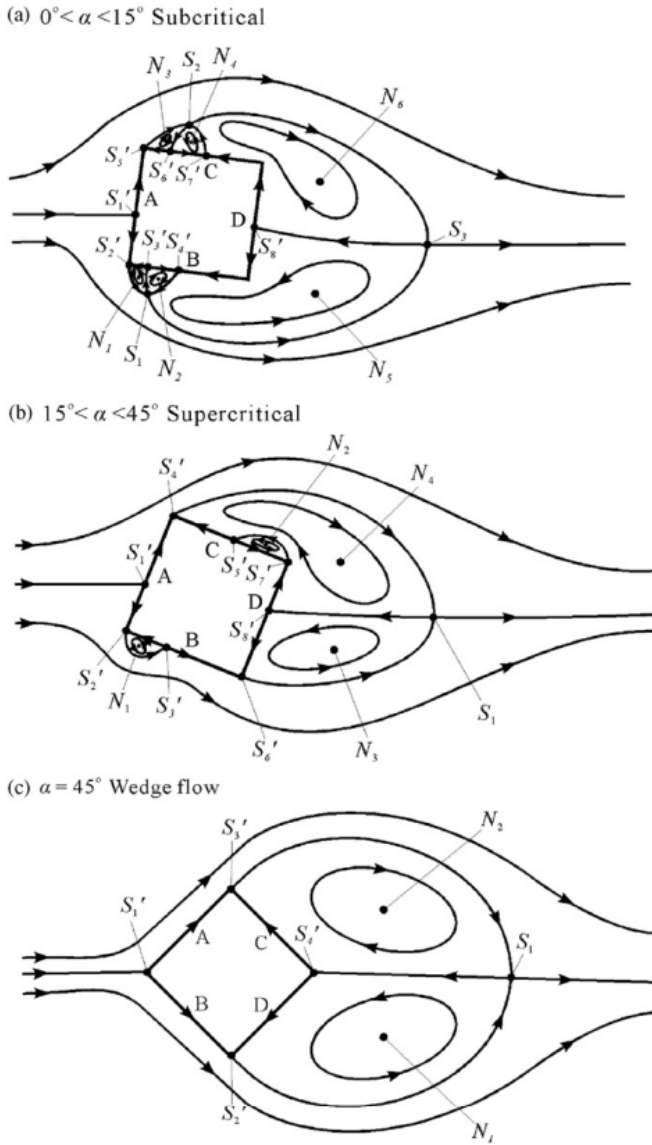


Figure 2.3: Two-dimensional flow patterns from Huang [24]. S denotes a saddle and N a node. Measurements at $Re_D = 5000$ to $Re_D = 120000$

figure 2.4. In the topological terminology a critical point is a point in the flow where the streamline slope cannot be identified for example a saddle (see points marked with S in figure 2.3). A separatrix is a streamline which leaves or terminates at a saddle.

Figure 2.4 (a) shows the position of the so called stagnation line or a three-way saddle. The free stream impinges on the face A and bifurcates at that line. The dark oil strip moves towards edge between faces A and B with the increasing angle of attack. The position of the stagnation point is not affected by changing the Reynolds number.

Apart from the leading wall we can see the significant discontinuities in position of oil strips occurring at the critical angle of attack.

Figure 2.4 (b) shows the position of critical points at side B. In subcritical range (below α_{cr}) there is a dual-ring bubble behind the leading edge, and the plot shows its downstream second oil strip position reaching the center of that face at zero angle of attack and then being reduced as the angle increases. This point is a three-way saddle. When in supercritical region only one oil strip is visible at the point of flow reattachment and it is plotted on that range. The reattachment bubble is getting smaller as angle approaches 45° , when it disappears. It can be seen that in subcritical regime the complicated recirculation zone is changing with Reynolds number, but the reattachment point position in supercritical range does not depend on Reynolds number anymore.

At face C there is no clear oil strips, but oil bands appear. In the subcritical range the figure 2.4 (c) shows the position of the downstream limit of the oil band. The oil flow directions examined by Huang [24] led him to state that there exists again a double recirculation bubble which is contained within this oil band. In supercritical mode there is a recirculation bubble at the downstream corner whose extent position (three-way saddle) is plotted in figure 2.4 (c) at angles above α_{cr} .

On face D there is a single oil strip at all angles $\alpha < 45^\circ$, marking the position of a stagnation point induced by the reverse flow from the wake bubble (three-way saddle). At $\alpha = 0^\circ$ this strip is located in the middle of face D. It moves towards the upper corner while in the subcritical mode ($\alpha < \alpha_{cr}$). Immediately after passing the critical angle α_{cr} the stagnation point jumps very close to the lower corner and continues travelling upwards towards the middle of the rear face. However once the rod is placed exactly at 45° the oil strip on side D disappears.

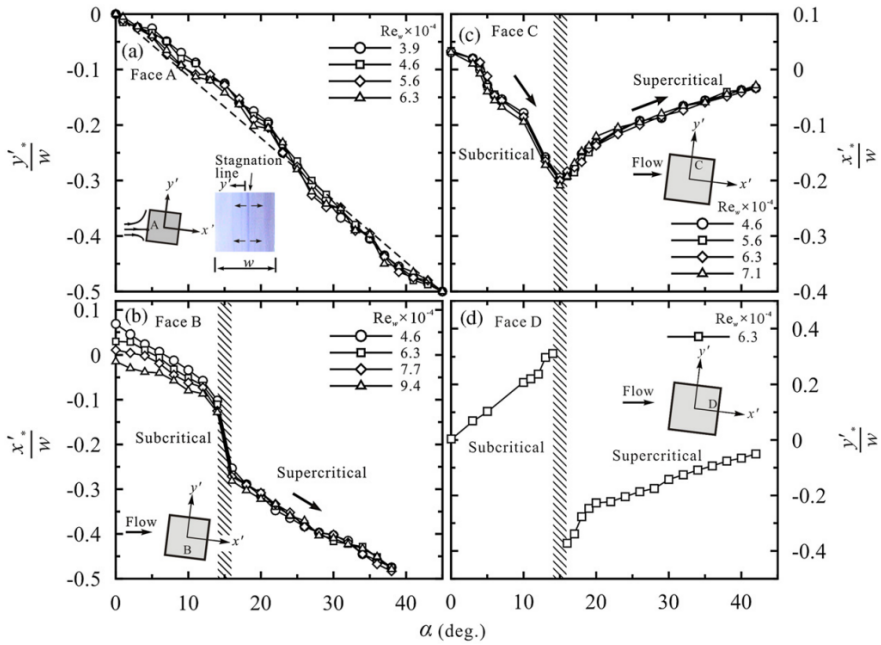


Figure 2.4: Normalised critical points positions on cylinder faces - surface-oil measurements from Huang [24]. $(x', y', z') = (x'_1, x'_2, x'_3)$, $w = D$ - rod width.

2.2.1 Value of critical angle of attack α_{cr}

In the paper of Tamura [60] the influence of turbulence level and the shape of the rod edges on the value of the critical angle α_{cr} is discussed. Increasing the incoming flow turbulence decreases the angle at which reattachment occurs (from 12° to below 10° [60]). Also having the rod corners chamfered or rounded can decrease α_{cr} from about 12° down to 7° and 5° respectively.

Chen [13] studied the dependence of α_{cr} on the Reynolds number. At low Reynolds numbers from 2000 to 3300 he found $\alpha_{cr} = 17^\circ$. For higher Reynolds numbers the critical angle decreases gradually to reach 13° above $Re_D = 8000$.

2.3 Flow in the wake

2.3.1 Instantaneous flow visualisations

In the wake of the square rod at incidence usually periodic vortex shedding is observed [13, 24, 26, 33, 39]. If a circular rod is positioned upstream of the square one a second non-shedding mode is possible [54] depending on the distance between the rods. Smoke visualisation of the shedding and not-shedding modes is shown in figures 2.5a and 2.5b.

2.3.2 Average flow pattern

In figure 2.6 we can see the average flow pattern obtained from PIV measurements by Roosenboom [52]. It agrees with the general classification of flows introduced above [24]. In chapter 4 we will compare in detail the PIV data of Roosenboom [52] with our numerical simulations.

2.4 Pressure on the rod surface at different angles of attack

The average pressure on surface of the rod is also affected by the angle of attack. An example of a C_p distribution around the rod from Igarashi [26] can be seen in figure 2.7. Note the difference between the two angles around α_{cr} $\alpha = 10^\circ$ (black triangles pointing upwards) and $\alpha = 15^\circ$ (white triangles pointing downwards). X_s and X_r indicate the position of separation and reattachment respectively.

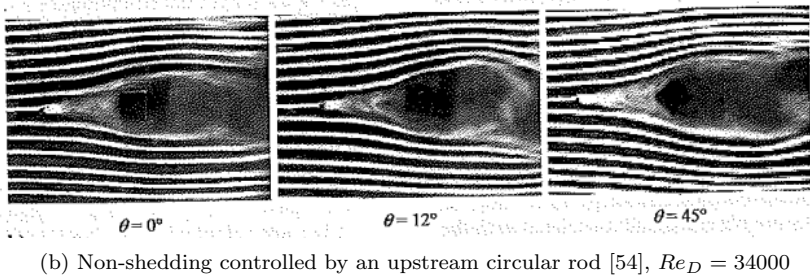
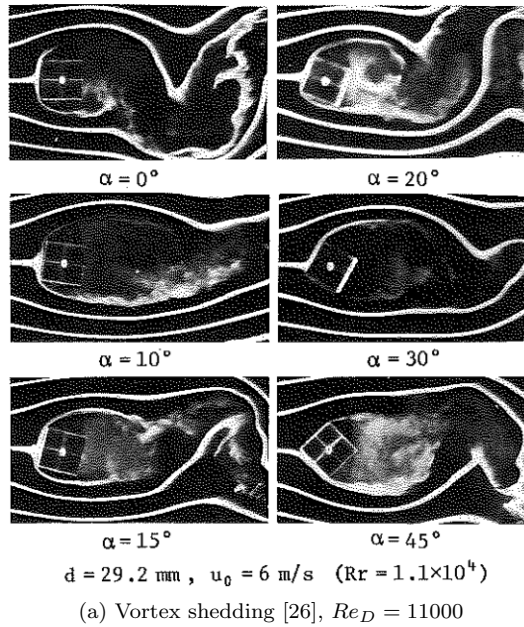


Figure 2.5: Smoke visualisation of the wake of a square rod from Igarashi [26] and Sarioglu [54].

An example spanwise distribution (along the rod length) of base pressure from an experiment performed by Bearman [9] is given in figure 2.8. We can see that due to the effect of the end-plates C_p is not uniform along the span.

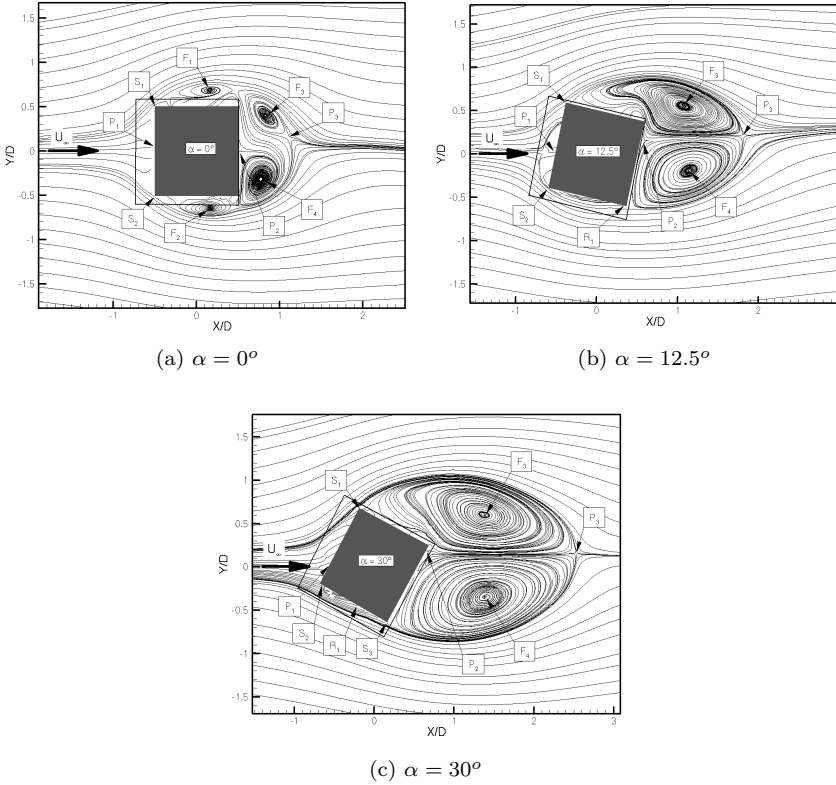


Figure 2.6: Average flow pattern from PIV measurements from Roosenboom [52]. The grey area is the rod cross-section, the square line marks the extent of perspective view of the CCD camera. $Re_D = 20000$

2.5 Lift and drag coefficients

2.5.1 Average lift and drag coefficients at different angles of attack

In figure 2.9 we see the mean lift and drag coefficients (C_l and C_d) determined by integrating the mean pressure measurements from Igarashi [26]. The data of Otsuki et al. [48] shown on that plot comes from direct force measurements. We can see that around $\alpha_{cr} \approx 14^\circ$ the drag coefficient reaches

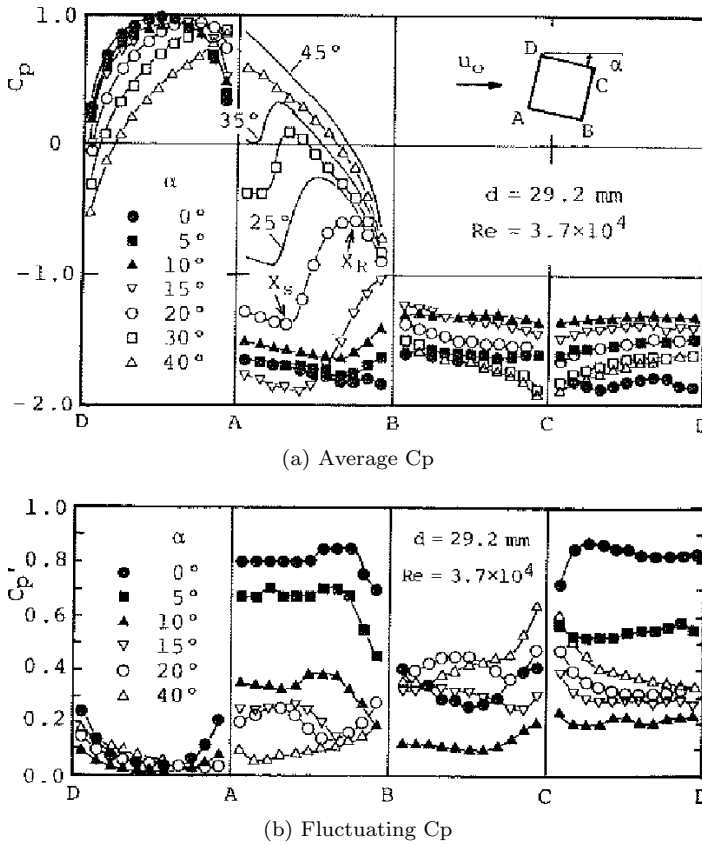


Figure 2.7: Pressure coefficient C_p at the rod walls for different angles of attack from Igarashi [26] (not corrected for blockage). $Re_D = 37000$

its minimum value and the slope of lift turns from positive to negative. The differences of C_d at higher angles of attack between the authors is due to the effect of blockage, i.e. finite wind tunnel cross-section.

In the work of Tamura [60] the effect of turbulence level on lift and drag is studied (figure 2.10). As the turbulence intensity increases, the C_d values decrease. This is especially visible at angles below α_{cr} . At $\alpha = 0^\circ$ the mean C_d with turbulence intensity $I = 14\%$ is 25% lower than C_d with low turbulence flow ($I = 0.4\%$). For the lift coefficient C_l he finds that the flow starts reattaching for lower angles with increasing level of turbulence.

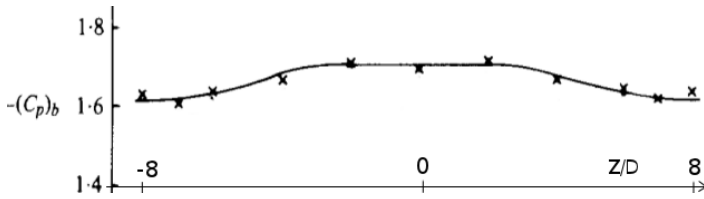


Figure 2.8: Average base pressure coefficient C_{pb} at rear side of the rod vs. spanwise coordinate at $\alpha = 0^\circ$ from Beraman [9] (not corrected for blockage).

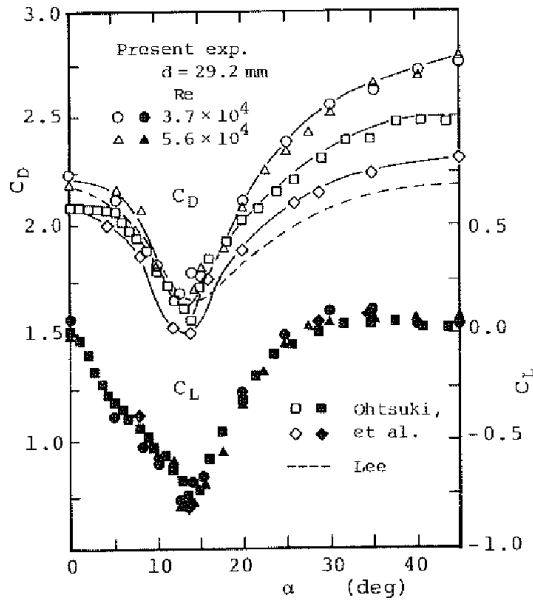


Figure 2.9: Mean lift and drag coefficients C_l and C_d from Igarashi. [26] Re_D from 37000 to 56000

The minimum of C_l occurs at a lower angle of attack α_{cr} with increasing turbulence level.

In the paper of Tamura [60] the influence of sharpness of the rod corners on the mean and fluctuating forces acting on the rod placed in uniform flow (see figure 2.11) is considered. He studied the sharp edged-rod, a chamfered one, and one with rounded corners. The sharp-edged square rod has larger value

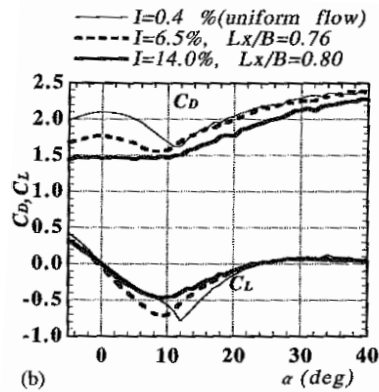


Figure 2.10: Influence of turbulence intensity on coefficients of lift and drag for different angles of attack from Tamura [60]. $Re_D = 30000$

of mean drag than the two other rods (more than 50% for $\alpha < 5^\circ$ - see figure 2.11a). The shape of the edges affects also the value of the critical angle α_{cr} which is as low as 5° for rounded rod, around 7° for the chamfered one, and around 12° for the sharp-edged square rod. However it is the fluctuation of lift that is the most spectacularly affected by the sharpness of the edges (see figure 2.11b). At angle of attack $\alpha = 0^\circ$ it is more than a factor two higher for the sharp-cornered rod than in the case of rounded and chamfered ones.

2.5.2 Oscillating lift and drag coefficients at different angles of attack

Vickery [64] measured for a rod of aspect (length L to width D) ratio $L/D = 30$ at angle of attack $\alpha = 0^\circ$ the rms of the fluctuating lift coefficient (Cl_{rms}) of 1.32 in a smooth flow and 0.68 in a presence of large scale turbulence. The corresponding spanwise correlation lengths were $5.6D$ and $3.3D$ respectively.

Describing fluctuating lift and drag one has to present amplitude (or rms) and frequency of the time signal (Strouhal number).

Data concerning the oscillating drag coefficient as a function of angle of attack was not found in the literature. It is very difficult to measure accurately. In Vickery [64] we find the $Cd_{rms} = 0.17$ for zero angle of attack. Other data available refer to numerical simulations at zero angle of attack

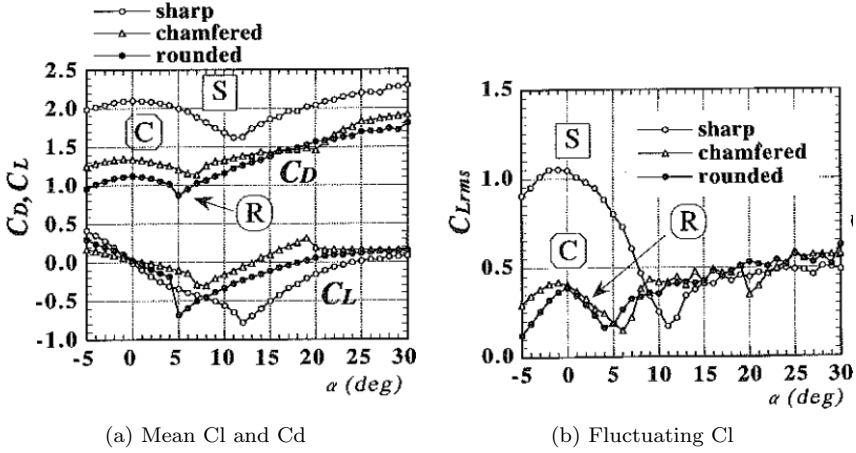


Figure 2.11: Influence of rod edges shape on coefficients of lift and drag for different angles of attack from Tamura [60]. $Re_D = 30000$

and are in the range of 0.1 – 0.37 [51, 58]. For RANS calculations one finds typically $Cd_{rms} < 0.1$ [58]. The data collected by Rodi [51] is obtained for a three-dimensional domain limited to four times the rod width in the spanwise direction. This configuration was also used by Sohankar [58].

In figure 2.12 we see the rms of lift from Knisely [33] measured with three-component load cells and Vickery [64] (with coarse angle resolution). If we compare the C_{Lrms} with Tamura [60] (figure 2.11b for the sharp-edged rod) there is a good agreement for low angles of attack. At $\alpha > 15^\circ$ the C_{Lrms} of Tamura [60] grows to reach 0.5 at $\alpha > 30^\circ$, while the data of Knisely [33] is 20% lower at this angle.

The frequency of the oscillation in the lift force is the same as the vortex shedding frequency [26, 33, 45, 60]. Igarashi [26] gives three different definitions of Strouhal number:

$$St = f D_{proj} / U_o$$

$$St_b = f D_{proj} / U_s$$

$$St_D = f D / U_o$$

where f is the dominating frequency, U_o is the inlet velocity, U_s - velocity along free streamline at separation point (where $U_s = U_o \sqrt{1 - C_{pb}}$). Lengths: D - rod width or D_{proj} - rod width projected normal to the wind

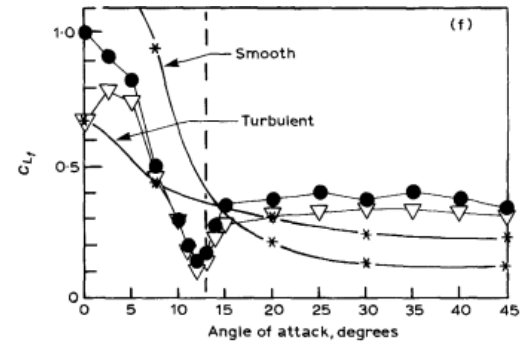


Figure 2.12: Fluctuating lift coefficient Cl_f from experiments of Knisely [33] $Re_D = 22000$ to 62000 , ∇ - spectral peak value, \bullet - rms value, $*$ - Vickery [64], $Re_D = 40000$ to 160000

direction. The behaviour of three Strouhal numbers as a function of angle of attack is shown in figure 2.13. Rounding or chamfering the edges increases the value of Strouhal number [60].

2.6 Sound produced by a square rod at incidence

Two-dimensional cylinders radiate tonal aerodynamic sound (whistling) referred to as an Aeolian tone generated by fluctuating lift and drag forces.

Uffinger et al. [62] measured flow field and sound around a wall-mounted rectangular cross-section rod with various additional shapes added to it. He ordered them with increasing sound pressure level as can be seen in figure 2.14.

The tonal noise produced by a square rod at incidence depends mainly on the amplitude of fluctuating lift [21, 25] and on its correlation length γ as suggested by Phillips [49]. Fujita [21] estimated, using the gaussian distribution fit, the correlation length coefficient γ of a surface pressure on a square rod at incidence (see figure 2.15) to be varying between $\gamma = 9$ and 12 for most angles of incidence. It has peaks up to $\gamma = 30$ around $\alpha = 45^\circ$ and $\alpha = 135^\circ$ where the flow is considered to be symmetric and most stable. He finds also considerable increase in spanwise correlation at 10° , 80° , 100° and 170° . This effect is not understood.

Fujita [21] measured a dramatic loss of sound pressure level (SPL) by 10 dB at the critical angle of attack α_{cr} (see figure 2.16). The results of

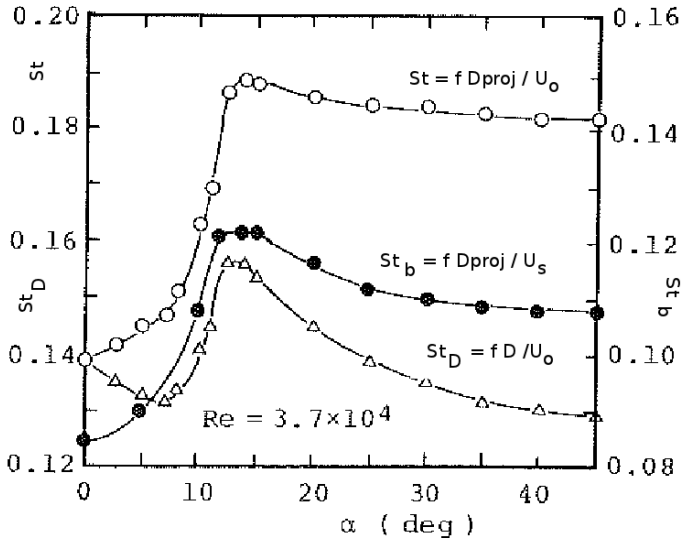


Figure 2.13: Strouhal numbers St , St_b and St_D based on rod width D , projected rod width D_{proj} and inlet velocity U_o or U_s from Igarashi [26], $Re_D = 37000$

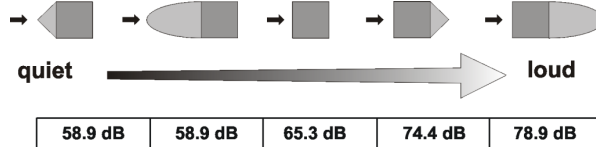


Figure 2.14: Ranking of geometries referring to the acoustic sound pressure level at $U_o = 30m/s$ from Uffinger [62], $Re_D = 37000$

measurements by Hutcheson and Brooks [25] at angles 0° 30° and 45° agree with sound pressure level predicted by Fujita [21]. Hutcheson and Brooks [25] state that sound generated by the rod is not affected by placing a grit (roughness) on its surface.

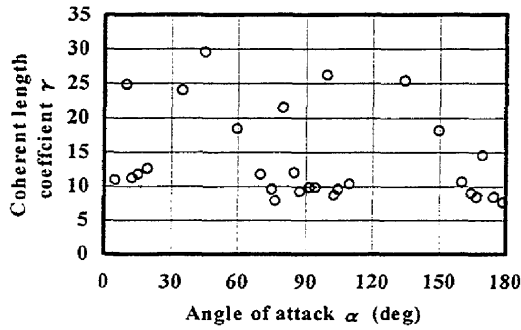


Figure 2.15: Coherent length coefficient γ of a pressure on a square rod at incidence from Fujita [21]

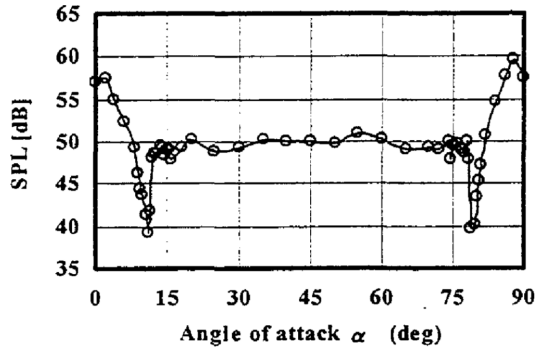


Figure 2.16: Measured sound pressure level (SPL) from Fujita [21]

2.7 Conclusion

Based on our review of the literature we conclude that:

There is a significant impact of angle of attack on velocity and pressure field. Flow around square rods can be classified as subcritical, supercritical and wedge flow regime depending on angle of attack changing the topological features of the flow.

At the critical angle of attack α_{cr} the strongest reattachment on the lower side wall occurs. At this angle there is a maximum of vortex shedding frequency. The mean and fluctuating forces have their minimum. The tonal

sound radiation displays a sharp minimum at α_{cr} . This critical angle of attack depends on Reynolds number (for $Re_D < 5000$), turbulence intensity of the incoming flow and sharpness of the rod edges.

Chapter 3

Flow modeling based on LES

The goal of this chapter is to determine the effect of numerical parameters of Large Eddy Simulation (LES) on the predicted hydrodynamic pressure and velocity field. We perform this study on square rod at zero angle of attack.

In section 3.1 we give a short description of equations used. In section 3.2 we describe the geometry and discretisation of the computational domain used in this chapter. Section 3.3 explores the influence of the grid resolution at the walls of the rod and the eventual use of wall functions. We move on to study the effect of the spanwise dimension of the domain in section 3.4. In section 3.5 we report the differences between using periodic spanwise boundary condition and non-slip end-plates.

3.1 Governing equations

We consider the incompressible time-dependent Navier Stokes (N-S) equations describing the continuity and momentum laws for the spatial domain $\vec{x} \in \Omega$ as function of time t :

$$\frac{\partial u_i}{\partial x_i} = 0 \quad (3.1)$$

$$\frac{\partial u_i}{\partial t} + \frac{\partial u_i u_j}{\partial x_j} = -\frac{1}{\rho} \frac{\partial p}{\partial x_i} + \nu \frac{\partial^2 u_i}{\partial x_j \partial x_j} \quad (3.2)$$

where $u_i(\vec{x}, t)$, $i = 1, 2, 3$ is the velocity vector component, $p(\vec{x}, t)$ is the pressure, ρ is the fluid density and ν is the kinematic viscosity. We consider ρ and ν as constants. The Einstein summation convention is used for the index notation.

3.1.1 DNS

The most straightforward way of solving the N-S equations is to solve them directly without modeling. In case of a turbulent flow as we expect in our

experiments, it means that the mesh and time stepping must be fine enough to resolve the smallest scales down to the Kolmogorov [34] one. These techniques have made available data that had never been measured before: multipoint and not disturbing the flow. The knowledge gained through simulations allowed for turbulence modeling validation and development, and have given the new insight into the physics of turbulence [41].

Such a calculation is however very costly and nowadays still prohibitive for engineering applications. We will therefore consider modeling of the turbulence.

3.1.2 u-RANS

Unsteady Reynolds Averaged Navier Stokes (u-RANS) equations [67] for a turbulent flow are based on the principle of the Reynolds decomposition of the velocity u_i (and other fluctuating fields like pressure) into a mean \bar{u}_i and fluctuating part u'_i .

$$u_i = \bar{u}_i + u'_i \quad (3.3)$$

$$\bar{u}_i = \lim_{T \rightarrow \infty} \frac{1}{T} \int_{t_0}^{t_0+T} u_i dt \quad (3.4)$$

Where \bar{u}_i is a time average. For turbulence that is both stationary and homogeneous (i.e. ergodic) the time average is equivalent to ensemble-average.

After applying the decomposition and time-averaging on the standard N-S equations 3.2 one obtains the RANS set:

$$\frac{\partial \bar{u}_i}{\partial x_i} = 0 \quad (3.5)$$

$$\frac{\partial \bar{u}_i}{\partial t} + \frac{\partial \bar{u}_i \bar{u}_j}{\partial x_j} = -\frac{1}{\rho} \frac{\partial \bar{p}}{\partial x_i} + \nu \frac{\partial^2 \bar{u}_i}{\partial x_j \partial x_j} - \frac{\partial \overline{u'_i u'_j}}{\partial x_j} \quad (3.6)$$

which has new unknowns forming so called specific Reynolds stress tensor $\tau_{ij} = -\overline{u'_i u'_j}$.

The system has to be closed by additional model equations. There are many possibilities of solving this closure problem. One may relate the Reynolds stresses to the mean flow strain rate \bar{S}_{ij} using the concept of eddy viscosity. Unfortunately a universal model coping with all the flows is not known yet.

In this work we used simulations performed with a four-equation v2f turbulence model at UTwente by van der Weide [63]. V2f model was first introduced by Durbin [18] and has become increasingly popular, due to its ability

to correctly account for near-wall damping without the use of ad-hoc damping functions [31]. This model consists of solving two transport equations in addition to the standard $k - \epsilon$ model equations. It adds a convection-diffusion transport equation for the wall-normal stress, \bar{v}^2 , and an elliptic equation for a relaxation function, f .

3.1.3 Large Eddy Simulation formulation

Large Eddy Simulation (LES) is an attractive technique for simulating turbulent flows. It follows the Kolmogorov's [34] theory that the large eddies of the flow are depending on the geometry while the smaller scales are more universal. This allows one to explicitly solve for the large eddies in a calculation and implicitly account for the small eddies by using a subgrid-scale model (SGS model).

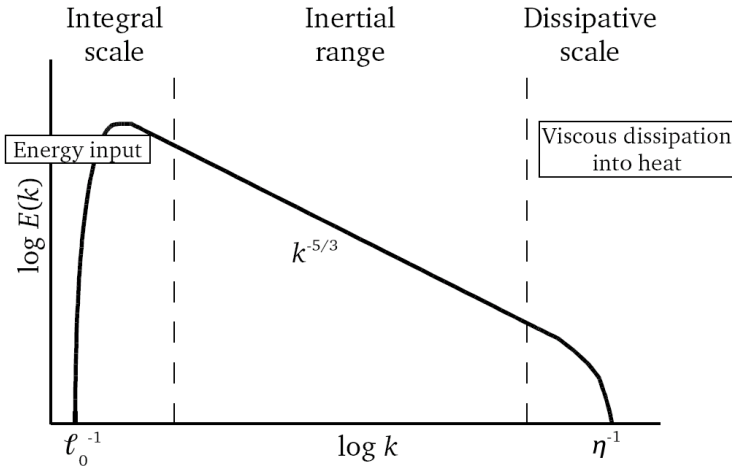


Figure 3.1: Turbulent energy spectrum, from the macroscopic scale l_0 to the Kolmogorov scale η , as a function of the wave number k

Energy (figure 3.1) is extracted from the main flow by stretching of large vortical structures by velocity gradients. The energy cascades down to smaller spatial scales until the Kolmogorov scale η is reached at which molecular viscosity becomes dominant and the energy is dissipated into heat.

We separate the velocity field into a resolved and sub-grid part [53]. The resolved part of the field represents the "large" eddies, while the subgrid part

of the velocity represent the "small scales" whose effect on the resolved field is included through the subgrid-scale model. The filtering is the convolution of a function with a filtering kernel G :

$$\bar{u}_i(\vec{x}) = \int G(\vec{x} - \vec{\xi})u(\vec{x})d\vec{\xi}, \quad (3.7)$$

resulting in

$$u_i = \bar{u}_i + u'_i, \quad (3.8)$$

where \bar{u}_i is the resolvable scale part and u'_i is the subgrid-scale part. Most implementations of LES use the grid itself as the filter and perform no explicit filtering. This is the approach used in Fluent [4], which is the LES solver used for the calculations in this thesis.

The filtered equations are developed from the incompressible Navier-Stokes equations (3.2). Substituting in the decomposition $u_i = \bar{u}_i + u'_i$ and $p = \bar{p} + p'$ and then filtering the resulting equation gives the equations of motion for the resolved field:

$$\frac{\partial \bar{u}_i}{\partial t} + \bar{u}_j \frac{\partial \bar{u}_i}{\partial x_j} = -\frac{1}{\rho} \frac{\partial \bar{p}}{\partial x_i} + \frac{\partial}{\partial x_j} \left(\nu \frac{\partial \bar{u}_i}{\partial x_j} \right) + \frac{1}{\rho} \frac{\partial \tau_{ij}}{\partial x_j}. \quad (3.9)$$

The extra term $\frac{\partial \tau_{ij}}{\partial x_j}$ in (3.9) arises due to the fact that

$$\overline{u_j \frac{\partial u_i}{\partial x_j}} \neq \bar{u}_j \frac{\partial \bar{u}_i}{\partial x_j} \quad (3.10)$$

$$\tau_{ij} = \bar{u}_i \bar{u}_j - \overline{u_i u_j} \quad (3.11)$$

Subgrid-scale turbulence models usually employ the Boussinesq hypothesis [23], and calculate (the deviatoric part of) the subgrid-scale (SGS) stress τ_{ij} using:

$$\tau_{ij} - \frac{1}{3} \tau_{kk} \delta_{ij} = -2\mu_t \bar{S}_{ij} \quad (3.12)$$

where \bar{S}_{ij} is the rate of strain tensor for the resolved scale defined by

$$\bar{S}_{ij} = \frac{1}{2} \left(\frac{\partial \bar{u}_i}{\partial x_j} + \frac{\partial \bar{u}_j}{\partial x_i} \right) \quad (3.13)$$

and μ_t is the subgrid-scale turbulent viscosity also written as $\nu_t = \mu_t/\rho$. Substituting into the filtered Navier-Stokes equations, we then have

$$\frac{\partial \bar{u}_i}{\partial t} + \bar{u}_j \frac{\partial \bar{u}_i}{\partial x_j} = -\frac{1}{\rho} \frac{\partial \bar{p}}{\partial x_i} + \frac{\partial}{\partial x_j} \left([\nu + \nu_t] \frac{\partial \bar{u}_i}{\partial x_j} \right), \quad (3.14)$$

where the incompressibility constraint has been used to simplify the equation and the pressure \tilde{p} is now modified to include the trace term $\tau_{kk}\delta_{ij}/3$.

3.1.3.1 Subgrid-scale turbulence model

In this thesis we chose to use the off-the-shelf commercial CFD solver, Fluent [1]. This solver has available the following subgrid scale models:

- Smagorinsky-Lilly [57],
- Dynamic Smagorinsky [22],
- Wall-Adapting Local Eddy-viscosity (WALE), [44]
- Dynamic Kinetic Energy Subgrid-Scale Model [32]

We decided not to use dynamic models as they are more computationally intensive and may introduce instabilities [43, 44]. Smagorinsky-Lilly was ruled out due to poor performance in wall bounded flows. The WALE model is designed to return the correct wall asymptotic ($\propto y^3$) behaviour of turbulent viscosity for wall bounded flows and can reproduce the transition from laminar to turbulent flow.

In the WALE [44] approach used in current calculations the eddy viscosity is based on a square of the velocity gradient tensor $\bar{g}_{ij}^2 = \bar{g}_{ik}\bar{g}_{kj}$:

$$\nu_t = \Delta_s^2 \frac{(S_{ij}^d S_{ij}^d)^{3/2}}{(\bar{S}_{ij} \bar{S}_{ij})^{5/2} + (S_{ij}^d S_{ij}^d)^{5/4}} \quad (3.15)$$

$$\Delta_s = C_w V^{1/3} \quad (3.16)$$

$$S_{ij}^d = \frac{1}{2} (\bar{g}_{ij}^2 + \bar{g}_{ji}^2) - \frac{1}{3} \delta_{ij} \bar{g}_{kk}^2 \quad (3.17)$$

$$\bar{g}_{ij} = \frac{\partial \bar{u}_i}{\partial x_j} \quad (3.18)$$

$$(3.19)$$

where \bar{S}_{ij} is the rate-of-strain tensor for the resolved scale defined (3.13), V is the volume of the cell.

We use the value of the constant $C_w = 0.325$, which is the common practice for this model.

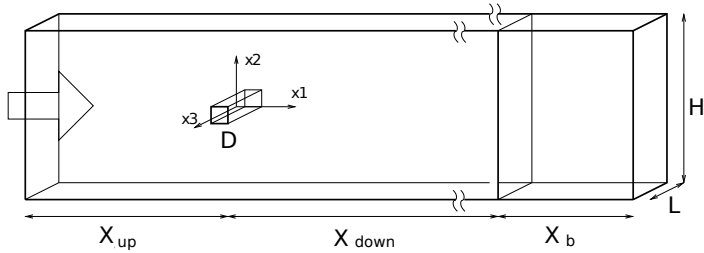


Figure 3.2: LES computational domain

3.2 Model Problem

To investigate sound generation on flows around bluff bodies or obstructions, we studied the model problem of a flow around a square rod at angle of attack $\alpha = 0^\circ$ (figure 3.2). The coordinate system (x_1, x_2, x_3) has its origin in the center of the rod. The rod is placed in the fluid domain which is restricted to a box of size $(X_{up} + X_{down} + X_b) \times H \times L$ in directions x_1, x_2 and x_3 respectively. X_{up} is the domain extent upstream of the rod, X_{down} is the length of the domain downstream of the rod. X_b is the length of a buffer zone.

A preliminary study for the CFD outlet conditions was carried out on a similar geometry with an incompressible laminar flow[42]. It showed that it is necessary to place a pressure reference cell in a region without fluctuations. A buffer zone was added to damp out spurious waves due to the crossing of vortical disturbances at the downstream boundary. It consists of a mesh stretched in the streamwise direction starting from X_b before the outlet face. It ensures that vortices are dissipated before reaching the downstream boundary of the computational box. The stretching ratio is 1.2. The pressure reference cell is positioned at the downstream end of the buffer zone.

3.2.1 Blockage effects

Most experiments reported in the literature are carried out in a wind tunnel with a closed test section. Due to the limited size of the wind tunnel cross-section in x_2 direction there is a blockage effect. The aerodynamic coefficients of lift and drag (C_l and C_d respectively) are corrected for blockage using the formula [14]:

$$C_{d_{corr}} = C_d(1 - A_m/A_s)^N \quad (3.20)$$

where A_m is the model frontal area and A_s is the tunnel crosssectional area. Knowing both, we can also compute the blockage ratio. N is an empirical correction parameter and it depends on the length of the afterbody. For a square rod at $\alpha = 0^\circ$ N is usually taken as 1.3 [14].

3.2.2 Grid topology

LES

The LES grid was created using Gambit 3-d meshing tool [8], where initially a 2-d mesh was created in the plane $x_3 = L/2$. The mesh features a refinement close to the non-slip walls of the rod, and is solely composed of quadrilaterals. In order to control the desired resolution and gradual coarsening of the mesh it was built out of subdomains (see figure 3.3). The 2-d mesh was finally extruded along x_3 direction to obtain a hexahedral three-dimensional grid.

The mesh is cartesian around the rod and in its wake, with stretching allowing to have more points in the boundary layers next to the walls of the rod and coarser mesh outside the boundary layers. At distance of $0.8D$ from the walls of the rod we start a quadrilateral (non-cartesian) grid providing a transition from the rod to the channel walls (figure 5.7).

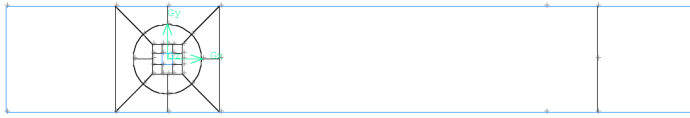


Figure 3.3: Mesh topology

uRANS

The uRANS was solved on a 2-d mesh, consisting of quadrilateral curvilinear elements as shown in figure 3.4. The square rod is placed in the center of a circular domain, where the outer circle has a radius of 50 rod diameters [63].

3.2.3 Boundary conditions

LES

We group boundaries as follows:

- 1 - the flow inlet is at the plane $x_1 = -X_{up}$.

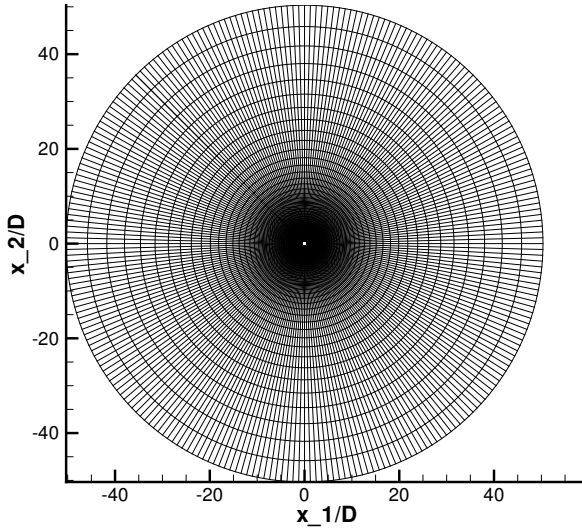


Figure 3.4: Mesh uRANS

2 - at planes $x_2 = \pm H/2$

3 - at planes $x_3 = \pm L/2$

4 - the flow outlet at plane $x_1 = X_{down} + X_b$

The inlet and outlet boundaries 1 and 4 remain the same in all cases solved. At boundary 1 we apply uniform inlet velocity [3]. Outlet (boundary 4) has zero gauge pressure condition [5]. Boundary 2 is either a slip- or non-slip wall [7]. Boundary 3 is either a non-slip wall representing end-plates or a periodic boundary condition in the direction x_3 .

The calculations were initialised with uniform velocity (equal to the inlet velocity) and atmospheric pressure in the whole computational domain.

uRANS

For the uRANS calculations, non-slip boundary conditions were used on the rod-edges and a far-field boundary condition based on the inlet velocity was applied on the domain outer boundary.

3.2.4 Discretisation

LES

The LES solver of Fluent software [1] consists of a cell-centered finite volume discretisation of the flow equations, formulated on a velocity-pressure coupling algorithm (PISO). This means that the momentum equations (with velocity as unknowns) are solved sequentially - segregated from the mass conservation equation (where pressure is the unknown). Each equation is discretized implicitly into a linear system which is solved with algebraic multi-grid (AMG) which uses a standard V-cycle for the pressure and a flexible cycle for momentum which may or not include coarsest level solutions.

The spatial discretization of the convective fluxes follows a bounded central-differencing scheme. Central differencing (CD) serves as a good base to construct a scheme for LES, thanks to its low dissipation (2nd order). However it can introduce unphysical oscillations (sometimes called wiggles), therefore Fluent features the Bounded Central Differencing (BCD) scheme which is considered suitable for LES. The BCD consists of a blending between a 2nd order upwind and the 2nd order central scheme, therefore retains its formal 2nd order accuracy. Whenever the convection boundedness criterion (CBC) is violated, the scheme is switched to a first order upwind to avoid unphysical oscillations [2].

Time is discretized implicitly with an unconditionally stable backward difference of second order. To speed-up time-stepping, it uses a non-iterative time advancement (NITA) of the PISO algorithm [1] [28], where each segregated linear system is solved to enough accuracy, but no outer iterations are performed, thus saving iterations on the non-linear loop. We used a constant timestep assuring the CFL number to be below 1 for accuracy reasons.

uRANS

The solution of the compressible Reynolds-averaged Navier-Stokes equations is obtained by solving the flow equations decoupled from the turbulence transport equations. The flow equations are discretised using a cell centered finite volume approach using upwind scheme with Roe's approximate Riemann solver for the inviscid fluxes. To achieve 2nd order accuracy, a MUSCL approach with linear reconstruction is used to compute the gradient of the solution at the cell interfaces. The viscous fluxes are discretised with a standard 2nd order central scheme.

Time-stepping is achieved with an unconditionally stable 2nd order Backward Euler Method, where the non-linear system in time is solved using a pseudo-time stepping method.

The turbulence transport equations consist of a 4 equation V2F model cast in quasi-linear form and discretised with cell-centered finite differences using an upwind scheme for convective terms with a MUSCL discretisation and a MinMod limiter to clip unphysical over-shots. The viscous terms are centrally discretised following an orthogonal curvi-linear arrangement of the grid. This segregated finite difference discretisation ensures strict positivity, therefore avoiding unphysical oscillations on the turbulence quantities thus improving overall stability.

The whole iterative solution process is accelerated with a geometrical multi-grid (3W cycle) for the flow equations, combined with explicit Runge-Kutta smoothers, with turbulence frozen at the coarser levels. The turbulence transport equations are solved using a diagonal dominant alternative directions implicit method (DD-ADI) with inclusion of only the sink terms on the linearised Jacobian.

The above procedures were used at UTwente by E. van der Weide [63] to provide uRANS solutions used for comparison in this thesis.

3.2.5 Experiment at UTwente

Experiments of the model problem described in section 3.2, were performed at UTwente by Dorneanu [16]. Both static pressure on the surface of the rod and the radiation of the sound were measured. These values are compared to the numerical results in the following sections, where the experiment is identified as *current experiment*.

More detailed description of this experimental campaign can be found in chapter 5.

3.3 The influence of wall resolution and use of wall functions

In this section we compare simulations performed with different mesh refinements in the vicinity of the non-slip wall of the rod.

Friction at the wall causes the fluid to come to rest creating a boundary layer, as first described by Prandtl in 1904 [50, 56]. In order to characterise grid resolution at the wall we use a non-dimensional wall distance y_{min}^+ . This dimensionless distance is defined as:

$$y^+ = \frac{u_\tau y}{\nu} \tag{3.21}$$

where u_τ is the friction velocity defined as

$$u_\tau = \sqrt{\frac{\tau_w}{\rho}}. \quad (3.22)$$

where τ_w is the wall shear stress, y is the distance to the wall, ν is the molecular kinematic viscosity of the fluid of density ρ . One can also define the non-dimensional wall velocity $u^+ = u/u_\tau$.

In figure 3.5 we can see a typical self-similar plot of u^+ as a function of y^+ in a boundary layer of a channel flow without pressure gradient. It can be divided in several sublayers. Closest to the wall there is a viscous sublayer (up to $y^+ = 5$) where we have a linear velocity profile $u^+ \approx y^+$ due to the predominance of laminar viscosity. In the region above $y^+ = 30$ (called log-law, or fully turbulent region), where turbulent viscosity outweighs laminar viscosity, the velocity can be approximated by a logarithmic law of the form:

$$u^+ = \frac{1}{\kappa} \ln(y^+) + B \quad (3.23)$$

where κ is the von Kármán constant and B is a constant. The upper limit of applicability of this law depends on the Reynolds number of the flow. This logarithmic law can be derived [67] by postulating that the mean velocity gradient $\partial U/\partial y$ correlates to a function of u_τ , ν/u_τ and y . This function is experimentally observed in a wide range of cases to be:

$$\frac{\partial U}{\partial y} = \frac{u_\tau}{y} F(u_\tau y/\nu) \quad (3.24)$$

with

$$F(u_\tau y/\nu) \longrightarrow \frac{1}{\kappa} \quad \text{as} \quad u_\tau y/\nu \longrightarrow \infty \quad (3.25)$$

which by integration over y , we arrive to equation (3.23).

The transition region in between the viscous and the log-law sublayers at $5 \leq y^+ \leq 30$ is called the buffer sublayer, where neither laminar or turbulent viscosities are predominant, and therefore none of the above approximations is valid.

When we perform the numerical simulation it is crucial to properly capture the boundary layer near the wall, *i.e.* to accurately represent the boundary layer across its sublayers. Two alternative approaches are possible: solving the problem using enough mesh points in the boundary layer to resolve the velocity profile directly (DNS, resolved LES), or using special boundary

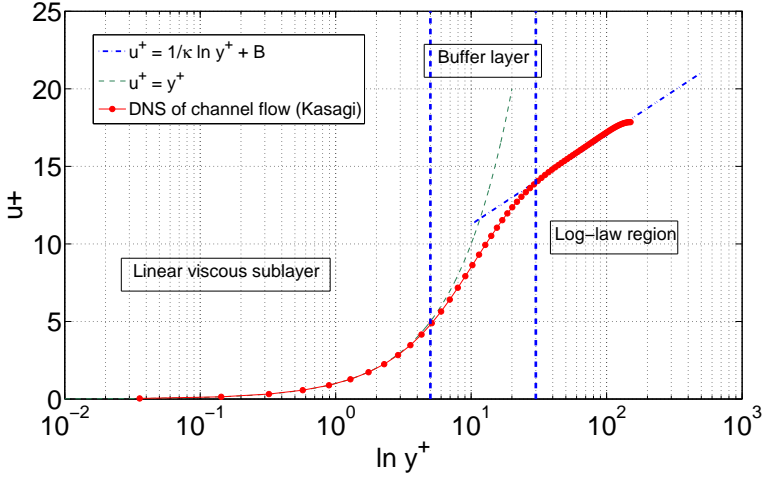


Figure 3.5: Boundary layer regions. Kasagi [30].

conditions that incorporate so called wall functions, that inherently model the viscous and buffer layers using analytical approximations.

Wall functions are implemented in Fluent software (see [6]) in such a way that, when the mesh is 'fine enough' to resolve the laminar sublayer, the wall shear stress is obtained from the laminar stress-strain relationship:

$$\bar{u}^+ = y^+ \quad (3.26)$$

If the mesh is too coarse to resolve the laminar sublayer, it is assumed that the centroid of the wall-adjacent cell falls within the logarithmic region of the boundary layer, and the law-of-the-wall is employed:

$$\bar{u}^+ = \frac{1}{\kappa} \ln E(y^+) \quad (3.27)$$

where κ is the von Kármán constant and $E = 9.793$. If the mesh is such that the first near wall point is within the buffer region, then the two above laws are blended in accordance with Kader [29]:

$$u^+ = e^\Gamma u_{\text{lam}}^+ + e^{\frac{1}{\Gamma}} u_{\text{turb}}^+ \quad (3.28)$$

where the blending function is given by:

$$\Gamma = -\frac{a(y^+)^4}{1 + by^+} \quad (3.29)$$

where $a = 0.01$ and $b = 5$.

This formula should guarantee the correct asymptotic behaviour for large and small values of y^+ and reasonable representation of velocity profiles in the cases where y^+ falls inside the wall buffer region. In Fluent solver [6], the wall function is automatically applied when the $y^+ = y_{min}^+$ of the first cell is above 11.

3.3.1 Parameters for the study of wall mesh refinement

The computational domain (fig. 3.2) in this study has the following dimensions (relative to rod width D): $X_{up} = 15D$, $X_{down} = 40D$, $X_b = 10D$ and $L = 3D$. Blockage, defined as $b = D/H$, along with other parameters can be found in table 3.1. The Boundary 2 is a slip-wall and boundary 3 in spanwise direction is periodic (see paragraph 3.2.3). Case A is wall-resolved LES with $y_{min}^+ < 1.5$ and without using the wall function. Case B features a grid with $y_{min}^+ < 7$, and represents a non-resolved LES without using the wall functions. Case C, where $y_{min}^+ < 60$, uses the wall functions with the logarithmic law as described in (3.27). The x_{min}^+ is the mesh size in streamwise direction on the wall of the rod (top/bottom). It stays within the guidelines for resolved LES for all the cases [65]. However the z_{min}^+ resolution in spanwise direction is about five times larger than the one recommended for the channel flow [65].

Case	x_{min}^+	y_{min}^+	z_{min}^+	b	$N \times N_{x_3}$	Re_D	No. of cells
LES - A	< 20	< 1.5	< 100	10%	30×18	5000	1.5 mln
LES - B	< 20	< 7	< 100	6%	30×18	5000	1 mln
LES - C	< 60	< 60	< 120	10%	10×18	12000	0.7 mln

Table 3.1: Summary of simulations in the mesh refinement study, where x_{min}^+ , y_{min}^+ and z_{min}^+ are the mesh resolutions in streamwise (x_1), wall-normal (x_2) and spanwise (x_3) directions on the rod walls, b is blockage and $N \times N_{x_3}$ is the number of cells on the side of the rod in x_1 and x_3 direction.

3.3.2 Discussion of Numerical Results

3.3.2.1 Impact of wall resolution on pressure

Average pressure coefficient distribution around the rod is shown on figure 3.6 using a surface coordinate S defined also in that figure. We present here both original data calculated in LES, and the ones corrected for blockage effects using the theory described in Courchesne [14]. It can be seen that the case with $y_{min}^+ = 60$ gives good prediction in the front and base pressure (sides A and D in figure 2.1) when not correcting for blockage (figure 3.6 (a)). Applying the correction (figure 3.6 (b)) reveals that average C_p of case C does not agree well with the experiments away from the front wall A. The pressure of the lateral sides (sides B, C in figure 2.1) is not well predicted by wall modelled LES case C. As expected - fine resolved case ($y_{min}^+ = 1.5$) gives result closer to experimental data (however there is asymmetry between sides B and C). The $y_{min}^+ = 7$ case (B) has average pressure similar as the resolved case A.

Looking at the dependence of mean lift and drag coefficients (Cl_{mean} and Cd_{mean}) on wall resolution (figure 3.7) one can see that Cl_{mean} predicted using wall functions is closest to zero. Coarser mesh induces higher turbulent viscosity. The predicted mean drag coefficient Cd_{mean} is in very good agreement with literature data [45], [33] using both resolved ($y_{min}^+ = 1.5$) and unresolved ($y_{min}^+ = 7$) LES. Simulation with wall function and $y_{min}^+ = 60$ underestimates the mean drag by roughly 20%. The Cl_{mean} and Cd_{mean} data from the current experiment of Dorneanu [16] were obtained by integrating the C_p results on walls C and B (top/bottom), and A, D (front/rear) (following the nomenclature of figure 2.1).

In figure 3.8, we present a comparison of RMS fluctuations of lift and drag coefficients (Cl_{rms} and Cd_{rms}) and we observe the decrease of these parameters when using wall function. Using the mesh with $y_{min}^+ = 60$ we have an error of nearly 30% on the Cl_{rms} compared with the direct measurements of Knisely [33]. The fact that Cl_{rms} in case A and B is overpredicted with respect to experimental data [33], [21] is explained in section 3.4. It is interesting to explore domain models with $y_{min}^+ \approx 30$ to see how the solution is affected when the first cell falls within the buffer region.

Still in figure 3.8, the experimental data of Knisely [33] was measured directly by pressure transducers on the rod surface. The Cl_{rms} of Fujita [21] and the experiment in UTwente by Dorneanu [16] are computed using the microphone measurements in the far field and processed by the following formula (rearranged from Fujita [21]):

$$Cl_{rms} = \frac{p_{ref} \times 4ar^2 \times 10^{SPL/20}}{\rho U_o^3 St_D x_2 L \sqrt{1 + \frac{1}{(2\pi St_D M r/D)^2}}} \quad (3.30)$$

where $p_{ref} = 2 \cdot 10^{-5} Pa$, a is the speed of sound, r is the distance from the rod axis to the microphone, SPL is the measured sound pressure level, x_2 is the second coordinate of the microphone, M is the Mach number, L is the rod length and D is the rod diameter.

All the Cl and Cd coefficients obtained by LES computation and discussed in this section were corrected for blockage effects using formula (3.20). The current experiment by Dorneanu [16] was performed on a semi-confined jet and was not corrected for blockage.

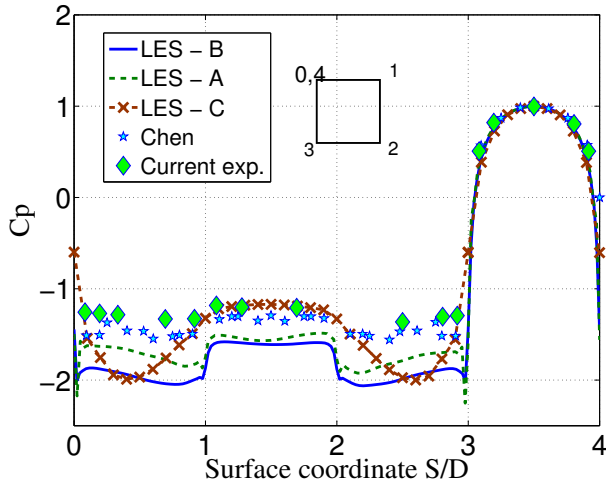
3.3.2.2 Impact of wall resolution on velocity field

The LES computations without wall models provide good prediction of streamwise velocity U_{mean} , U_{rms} and the normal direction x_2 (lift direction) V_{rms} . There is no significant difference between the resolved ($y_{min}^+ = 1.5$) and the under-resolved ($y_{min}^+ = 7$) mesh cases, as shown in figure 3.9. On the other hand we can see clearly that in the case of $y_{min}^+ = 60$ the solution neither agree with experiment [39] nor with numerical LES results from the literature [58]. It is especially important for V_{rms} which peak is 30% lower than expected. In case of spanwise velocity fluctuations W_{rms} (figure 3.9d) the under-prediction of velocity is mostly due to the domain size which is discussed in the section 3.4.

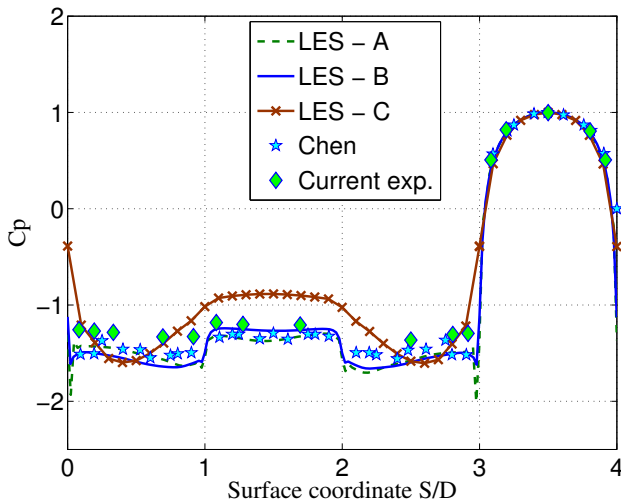
In figure 3.10 we show the velocity statistics in the wake, at $x_1 = 2.5D$. This profile can be compared with data from literature. The velocity is well predicted using finer meshes. W_{rms} is predicted in agreement with LES data available from literature when using wall function (LES - C, $y_{min}^+ = 60$) and the finest mesh resolution case gives the poorest fit with the reference data [58].

3.3.3 Conclusion

We assessed the impact of wall resolution at the rod surface on velocity and pressure fields. A domain of limited span dimension ($L = 3D$) was used to allow a full resolution of the boundary layer with the available computer power. We observe significant errors in mean and fluctuating force prediction when using a coarse mesh (LES - C, $y_{min}^+ = 60$) and log-law type of wall function (3.27).



(a) Not corrected for blockage effects



(b) Corrected for blockage effects

Figure 3.6: Time- and spanwise average C_p distribution on the rod surface at $\alpha = 0^\circ$ depending on wall resolution y_{min}^+ for $L = 3D$ and periodic boundary conditions in the x_3 direction. Side A (front) is between edges 3 and 4. Side B is between edges 2 and 3. Side C is between edges 0 and 1. Side D (rear) is between edges 1 and 2. Not corrected (a) and corrected (b) for blockage. Chen [13], $Re_D = 5300$, Current experiment [16], $Re_D = 46000$

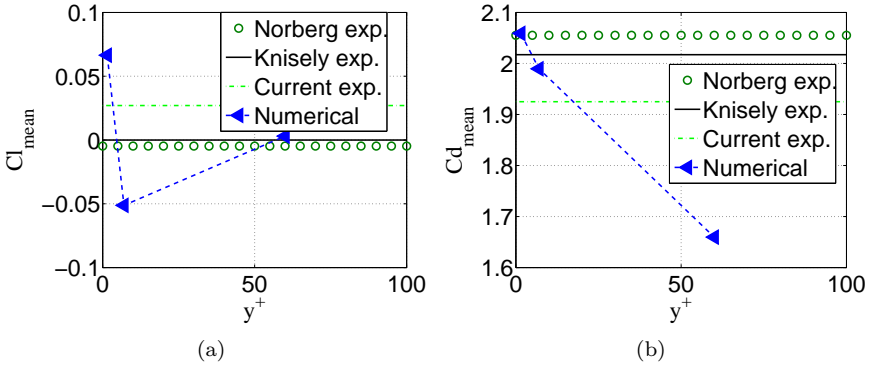


Figure 3.7: Cl_{mean} and Cd_{mean} vs. y_{min}^+ at the wall of the rod. Numerical results compared with experiments. Norberg [45], $Re_D = 5000$, Knisely [33], $Re_D = 22000$ to 62000, Current experiment [16], $Re_D = 46000$. LES corrected for blockage.

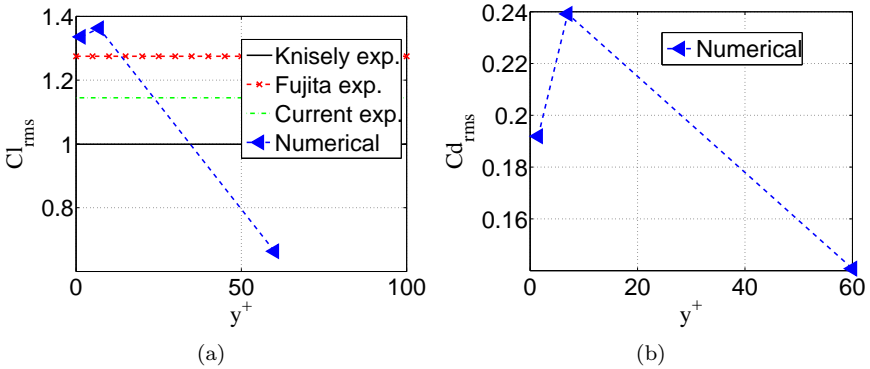


Figure 3.8: Cl_{rms} and Cd_{rms} vs. y_{min}^+ . Numerical results compared with experiments. Knisely [33] $Re_D = 22000$ to 62000, Fujita [21] $Re_D = 10000$, Current experiment [16], $Re_D = 46000$.

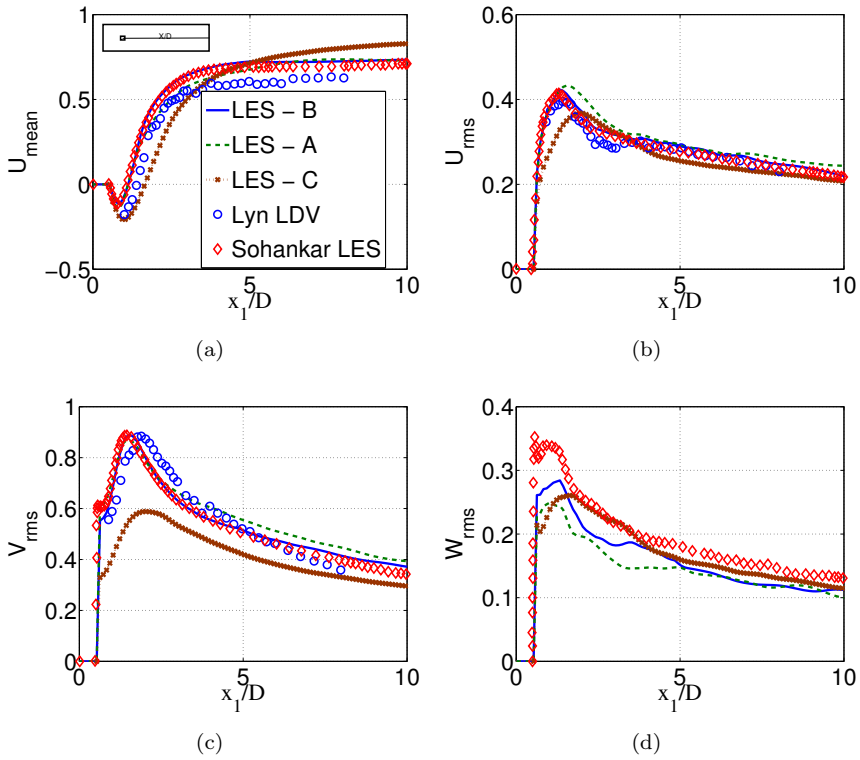


Figure 3.9: Time averaged streamwise velocity U_{mean} and RMS velocity $U_{rms}, V_{rms}, W_{rms}$ at centerline ($x_2 = 0, x_3 = 0$) at different wall resolution y_{min}^+ , for $L/D = 3$ and periodic boundary conditions in x_3 direction. Scaled with inlet velocity U_o . Lyn et al. [39], $Re_D = 22000$, Sohankar et al. [58], $Re_D = 22000$.

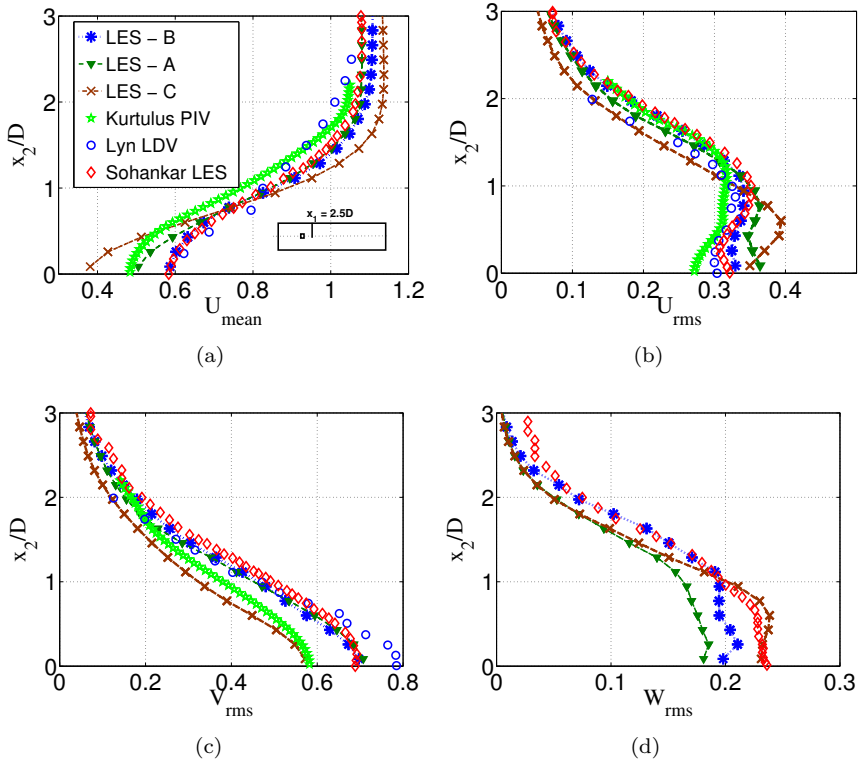


Figure 3.10: Time averaged streamwise velocity U_{mean} and RMS velocity $U_{rms}, V_{rms}, W_{rms}$ at $x_1 = 2.5D$ at different wall resolution y_{min}^+ ($L/D = 3$). Scaled with inlet velocity U_o . Kurtulus [35] $Re_D = 5000$, Lyn et al. [39], $Re_D = 22000$, Sohankar et al. [58], $Re_D = 22000$.

3.4 The influence of domain size in spanwise direction

A bluff-body wake often displays periodic vortex shedding like the von Kármán vortex street for cylinders. These are essentially 2-d instabilities.

Turbulent bluff-body wakes are more complex. They are not only determined by 2-d instabilities but 3-d vortical instabilities also play an important role. Already in the work of Phillips [49] we can find the formula predicting acoustic pressure taking into account the spanwise correlation length. It accounts for three-dimensional character of the flow at high Reynolds numbers. In this section we show the influence of the computational box width L on flow velocity, pressure and integral aerodynamic parameters.

3.4.1 Study parameters

The parameter of this study is the L dimension, as described in the figure 3.2 of the computational domain. It varies from zero (2-d case) till $17D$. The summary of simulations can be found in table 3.2.

Case	L/D	b	y_{min}^+	N_{x_3}	Re_D	Boundary 2	Boundary 3
uRANS 2-d	0	2%	< 0.02	0	144000	far field bc	-
LES - D	1	6%	< 1.5	10	5000	non-slip wall	periodic
LES - A	3	10%	< 1.5	18	5000	slip wall	periodic
LES - E	8.5	6%	< 1.5	50	5000	non-slip wall	periodic
LES - F1	17	6%	< 1.5	120	5000	non-slip wall	periodic

Table 3.2: Summary of simulations with different L/D spanwise size of the computational domain, b is blockage, y_{min}^+ - the wall normal cell resolution around rod walls, N_{x_3} - number of cells in x_3 direction.

3.4.2 Discussion of Numerical Results

All simulations discussed in this section were performed at angle of attack $\alpha = 0^\circ$. The uRANS results are provided by van der Weide (University of Twente). All the LES results were processed from time signals recorded during 10 periods of the dominant von Kármán vortex shedding. In all cases $y_{min}^+ < 1.5$ and Reynolds number $Re_D = 5000$ (with exception of uRANS) as described in table 3.2. Taking into consideration this value of y_{min}^+ , we can consider the LES simulations to be wall-resolved.

3.4.2.1 Impact of domain width on pressure field

Mean pressure

The average wall pressure coefficient (figure 3.11) is reproduced well at the pressure side and under-predicted after the separation of the flow. There is no significant difference between the LES cases solved. URANS does not compare well with the experiment at the lateral walls B and C.

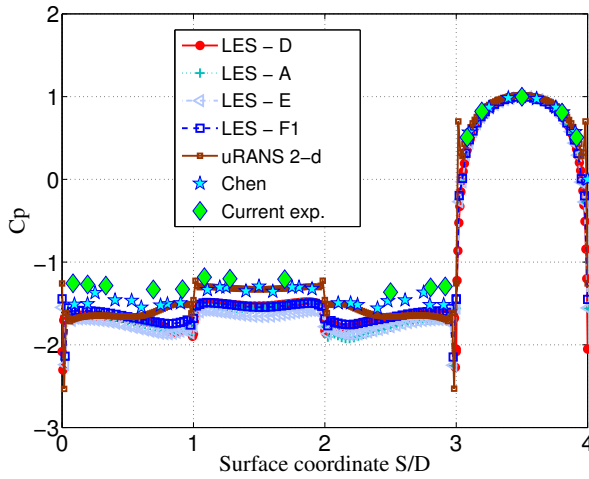
As this study was performed for angle of attack $\alpha = 0^\circ$, it is noteworthy that this particular configuration is widely reported in the literature (especially for numerical studies), yet it presents significant difficulties due to high sensitivity to symmetry of the inflow and the positioning of the rod. In a perfectly symmetric set-up (be it experiment or numerical grid) the expected mean lift force should be equal to zero. Both experiments and numerical results deviate from $Cl_{mean} = 0$. LES - D and LES - A (with $L/D = 1$ $L/D = 3$ respectively) present roughly 3 to 5 times larger difference than the other predictions and experiments (see table 3.3). The mean drag coefficient (Cd_{mean}) is generally over-predicted in numerical simulations when compared with experiments (see table 3.3).

Case	Cl_{mean}	Cd_{mean}
uRANS 2-d	-0.019	2.125
LES - D	-0.057	2.065
LES - A	0.067	2.059
LES - E	0.012	2.147
LES - F1	-0.010	2.130
Current exp. [16]	0.027	1.925
Knisely [33]	0	2.017
Norberg [45]	-0.005	2.055

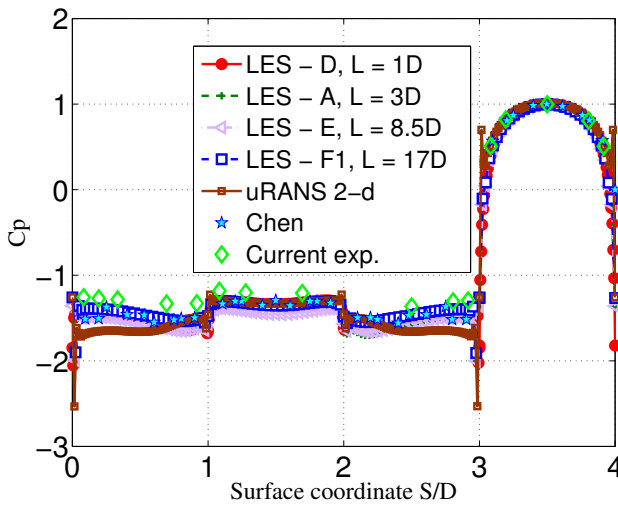
Table 3.3: Mean lift (Cl_{mean}) and drag (Cd_{mean}) coefficients, comparison of numerical predictions with the experimental data

Unsteady pressure

In figure 3.12, we can see that by using an LES with span lower than $L = 8D$ we over-predict the *rms* of lift by more than 10% reaching more than 50% for case with $L/D = 1$ compared with the direct pressure measurements of Knisely [33]. What is worth noting is that the 2-d URANS calculation over-predicts fluctuations of unsteady lift by only 20% which is better than resolved LES - A with $L = 3D$

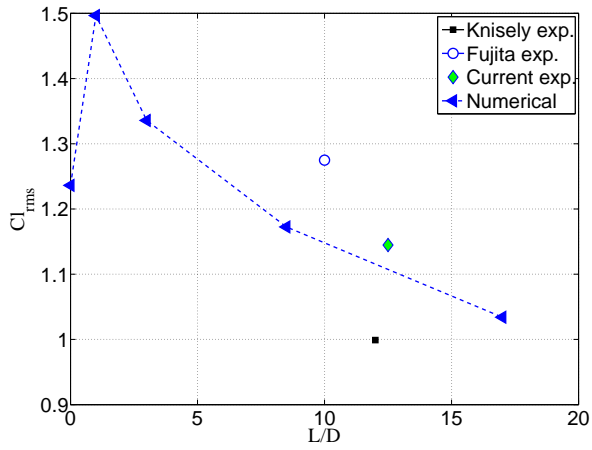


(a) Not corrected for blockage effects

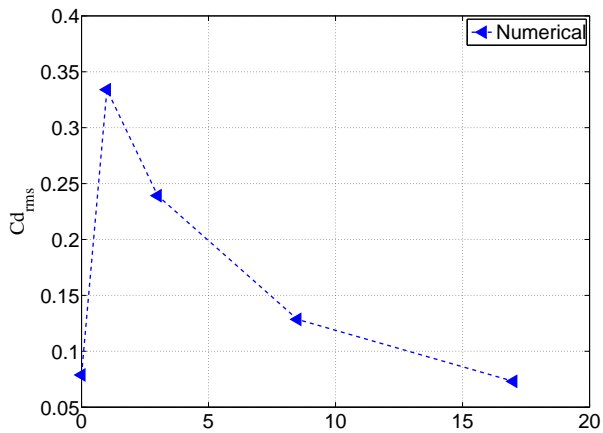


(b) Corrected for blockage effects

Figure 3.11: Time- and spanwise average C_p distribution on the rod surface at $\alpha = 0^\circ$ as a function of the length L of the calculation domain in the x_3 direction. LES $Re_D = 5000$, uRANS by van der Weide [63] $Re_D = 144000$, Chen [13], $Re_D = 5300$, Current experiment [16], $Re_D = 46000$.



(a)



(b)

Figure 3.12: Cl_{rms} and Cd_{rms} vs. L/D . Numerical results compared with experiments. LES $Re_D = 5000$, $L/D = 0$ refers to 2-d URANS, $Re_D = 144000$. Knisely [33], $Re_D = 22000$ to 62000 , Fujita [21], $Re_D = 10000$, Current experiment [16], $Re_D = 46000$.

Unsteady lift frequency (Strouhal number)

In the available literature the non-dimensional Strouhal number for the lift force, St_D , varies between 0.115 and 0.13. Figure 3.13 shows that for $L/D < 3$, we are clearly over-predicting as we find $St_D = 0.137$.

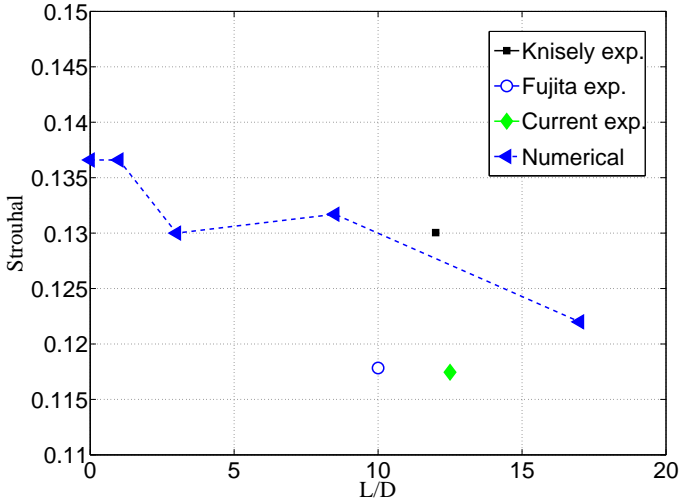


Figure 3.13: Strouhal number for Lift force at $\alpha = 0^\circ$ for $Re_D = 5000$. $L/D = 0$ refers to 2-d URANS [63]. Knisely [33], Fujita [21], Current experiment [16]

3.4.2.2 Impact of domain width on velocity field

When comparing the predicted average and RMS velocities with the experiments [35], [39] and other simulations [58] we note the importance of the spanwise size of the computational domain. Figures 3.14b and 3.15b show that both in x_1 and x_2 directions the U_{rms} is overpredicted when using a model with a length in the x_3 direction of $L = 1D$. The mean streamwise velocity U_{mean} and V_{rms} are not affected by the spanwise computational box size. The spanwise velocity W could be compared only with other LES results [58]. We can see in figures 3.14d and 3.15d that computations with $x_3 \leq 3D$ underpredict the velocity in the spanwise direction. The kinetic energy from spanwise direction x_3 (which is too narrow) is transferred to

the streamwise x_1 direction not affecting the transversal x_2 direction.

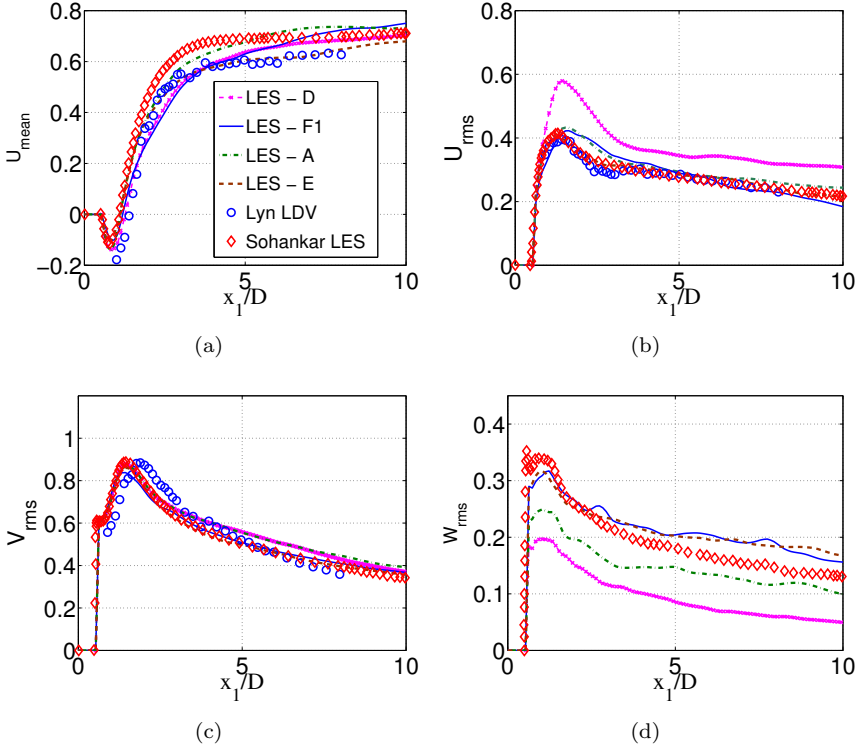


Figure 3.14: Time averaged streamwise velocity U_{mean} and RMS velocity $U_{rms}, V_{rms}, W_{rms}$ at centerline ($x_2 = 0, x_3 = 0$) for different width L of the calculation domain in x_3 direction. Scaled with U_o . LES, $Re_D = 5000$, Lyn et al. [39], $Re_D = 22000$, Sohankar et al. [58], $Re_D = 22000$.

3.4.3 Conclusion

We studied the influence of the size L of the calculation domain for the case of angle of attack $\alpha = 0^\circ$ and periodic boundary condition in the x_3 -direction. Increasing the calculation domain width L , we observe an asymptotic behaviour of force coefficients and Strouhal number at $\alpha = 0^\circ$ ap-

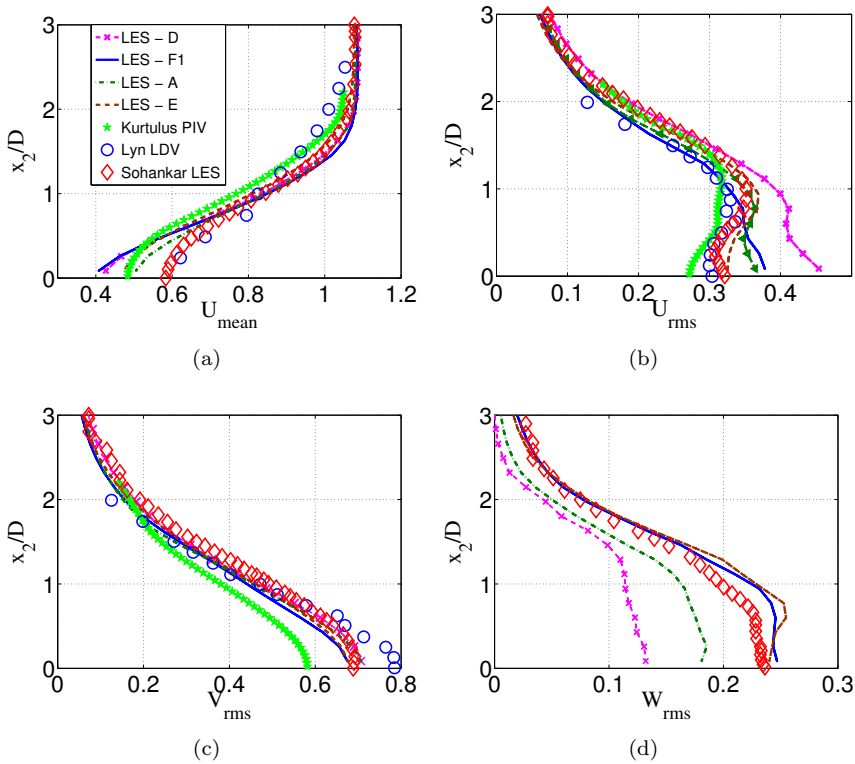


Figure 3.15: Time averaged streamwise velocity U_{mean} and RMS velocity $U_{rms}, V_{rms}, W_{rms}$ at $x_1 = 2.5D$ (downstream of the rod) for $Re_D = 5000$. Scaled with U_o . Kurtulus [35] $Re_D = 5000$, Lyn et al. [39], $Re_D = 22000$, Sohankar et al. [58], $Re_D = 22000$.

proaching the experimental results. The narrower the size of the computational box the higher are the coefficients of mean and fluctuating forces acting on the rod. Calculation with $L = 1D$ resulted in 50% overestimation on lift fluctuation, which was reduced to a value comparable with literature for the computational domain of $8.5D$ with the further decrease for $L = 17D$. The same behaviour was observed for drag fluctuation.

A satisfactory prediction of the velocity field is reached with $L = 8.5D$, while doubling the size of the computational box did not significantly affect the velocity field. This prediction was achieved with LES using the WALE

subgrid model. The velocity V in transversal x_2 direction is not affected by a narrow computational box in x_3 -direction. The RMS of the velocity in streamwise direction U_{rms} increases when L decreases, at the expense of the RMS of the spanwise velocity W_{rms} .

3.5 The influence of end-plates and their wall resolution

So far we were considering the numerical simulations of a model with periodic spanwise boundary conditions, therefore simulating an infinite rod and domain in the x_3 direction. In the experiments and in industrial installations comprising rods, they are usually attached to side walls or end-plates. In this section we will examine the effect of including the end-plates and thus assessing the influence of a finite domain in the flow field simulations.

3.5.1 Study parameters

For this analysis we used the widest case solved in section 3.4 with spanwise dimension $L = x_3 = 17D$. The computational domain can be seen in figure 3.2 and has the following dimensions (relative to rod width D): $X_{up} = 15D$, $X_{down} = 40D$, $X_b = 10D$, $L = 17D$ and $H = 17D$. The mesh has 5 mln elements and resolution of $y_{min}^+ < 1.5$ near the rod surface. This means that we are considering wall-resolved LES for the rod surface. The streamwise resolution at the surface of the rod is $x_{min}^+ < 20$. The mesh in spanwise direction is stretched to allow for better refinement close to the end-plates. The z_{min}^+ varies between 30 and 100.

Boundary 2 is a slip-wall. The parameter of this study is the boundary 3 in spanwise direction. The simulation is run first applying the periodic boundary condition (LES - F1 discussed already in section 3.4) and then run again using the same mesh, but applying non-slip wall boundary at planes $x_2 = \pm L/2$ (LES - F). The mesh resolution at those end-plates is compromised to $z_{min}^+ < 30$ so a blended wall function (3.28) is used there.

3.5.2 Discussion of Numerical Results

3.5.2.1 Impact of end-plates on pressure field

Mean pressure

In figure 3.16 we show the impact of using end-plates on the mean pressure field. On the left (figure 3.16a), one can see the distribution of mean C_p on the surface of the rod at periodic case (LES - F1). On the right (figure 3.16b) we see the map of mean pressure for case LES - F with end-plates. Two symmetric regions of low mean pressure at the rear of the rod are visible in the case LES - F. In the next figure 3.17, we plot detailed profiles of the mean pressure coefficient at the centerlines of the leading wall (stagnation line $x_1 = -0.5D$ $x_2 = 0$) and trailing wall (rear center line $x_1 = 0.5D$ $x_2 = 0$). It shows that in the case without end-plates the profiles are rather uniform, and introducing the end-plates causes two minima at the rear wall of the rod. According to the measurements of Fujita [21] the correlation length on a square rod at zero angle of attack is of the order $\gamma = 7 - 9$. In this case the computational domain has $L = 17D$ spanwise, which means that it is enough to contain twice the correlation length.

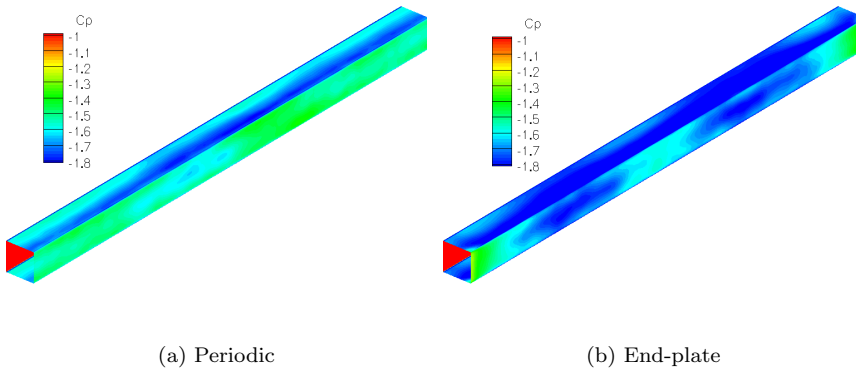


Figure 3.16: Map of averaged C_p for LES case F1 and F ($L = 17D$) - effect of end-plates. Coordinate system $(x, y, z) = (x_1, x_2, x_3)$

The two symmetric pressure minima at the rear wall explain the difference between LES with end-plates and periodic LES visible in figure 3.18 which shows the profiles of C_p averaged not only in time but also in spanwise direction.

When calculating $C_{l_{mean}}$ and $C_{d_{mean}}$ we integrate the pressure and viscous forces acting on the whole surface of the rod. In this way we obtain the plots in figure 3.19. In terms of average Lift and Drag both cases are in

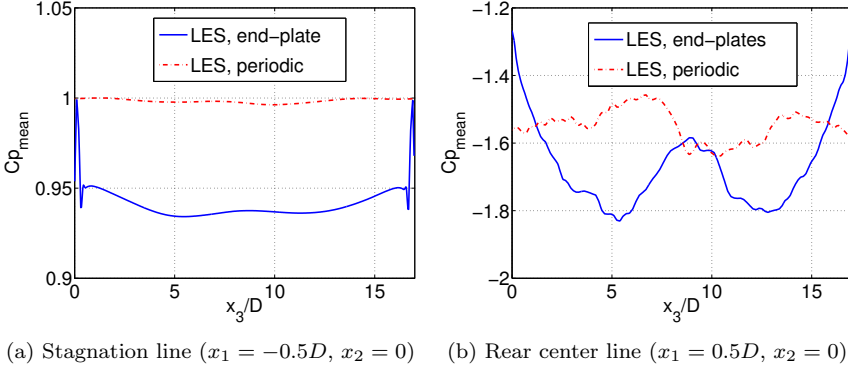


Figure 3.17: Spanwise evolution of averaged C_p for LES cases with and without end-plates

reasonable agreement with the literature, however the case with end-plates is closer to the experimental data.

Unsteady pressure

By defining the root-mean-square of pressure fluctuations Cp_{rms} as:

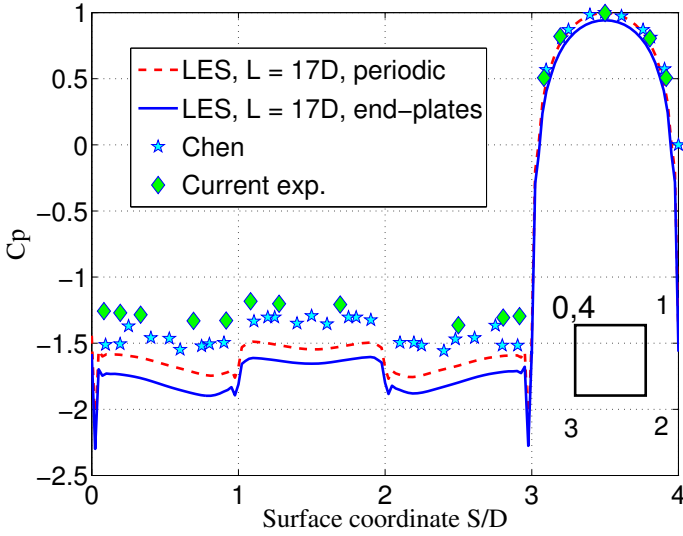
$$Cp_{rms} = p_{rms}/(0.5\rho U_o^2) \quad (3.31)$$

in figure 3.20, we observe that higher intensity fluctuations are happening on walls parallel to the flow ($x_2 = \text{const}$). Two maxima of the pressure fluctuation are positioned at the same spanwise location as the minima of average pressure in figure 3.16 for the case with end-plates.

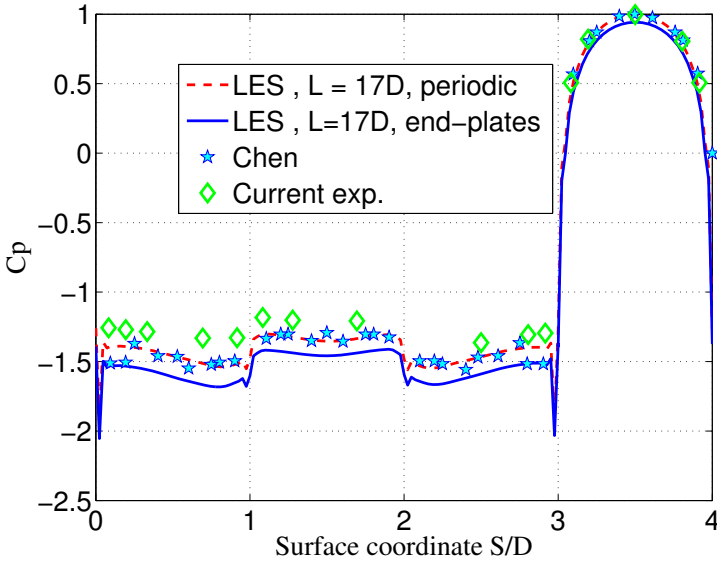
In figure 3.21 we examine the influence of introducing the end-plates on integral Cl_{rms} and Cd_{rms} . We can see that there is around 10% difference for both integral fluctuation of lift and drag. We have some data of Cl_{rms} measured directly on the surface from Knisely [33] and the ones retrieved from acoustic measurements using the equation (3.30) (current experiment [16] and Fujita [21]).

3.5.2.2 Impact of end-plates on velocity field

When analysing the impact of the end-plates on the velocity profiles in the wake (figures 3.22 and 3.23), we see that there is no significant impact due



(a) Not corrected for blockage effects



(b) Corrected for blockage effects

Figure 3.18: Time- and spanwise average C_p distribution on the rod surface at $\alpha = 0^\circ$. LES $Re_D = 5000$, Chen [13], $Re_D = 5300$, Current experiment [16], $Re_D = 46000$.

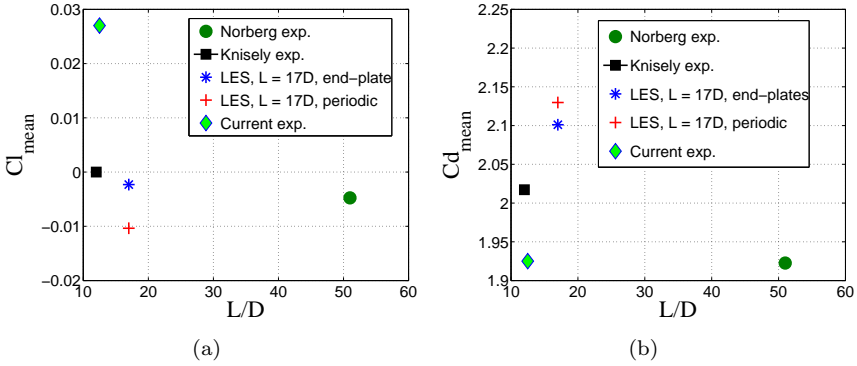


Figure 3.19: Cl_{mean} and Cd_{mean} in case with and without end-plates. Comparison with literature. Norberg [45] $Re_D = 5000$, Knisely [33] $Re_D = 22000$ to 62000 , Current experiment [16] $Re_D = 46000$

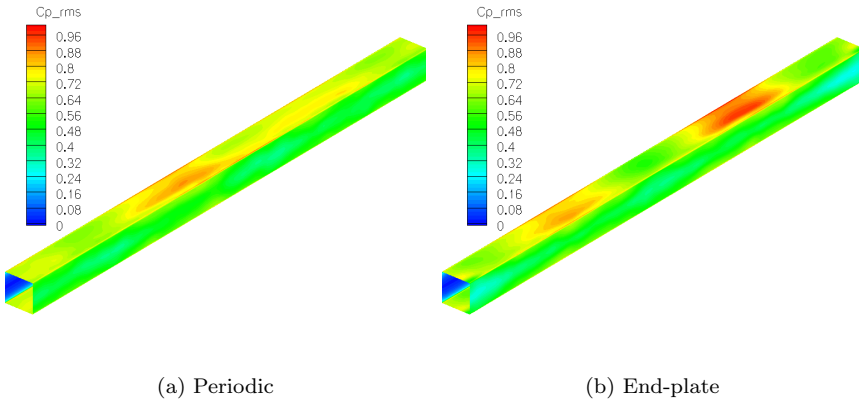


Figure 3.20: Map of Cp_{rms} for LES cases - effect of end-plates ($L = 17D$)

to different spanwise boundary condition. However, behind the rear wall of the rod ($x_1 = D/2 + 0.0033D$, $x_2 = 0$), if we look on spanwise behaviour of velocity fluctuations (figure 3.24), we see a difference between the periodic and non-slip wall boundary condition. All the RMS components of velocity have two maxima in the case with end-plates, which is not clearly visible in

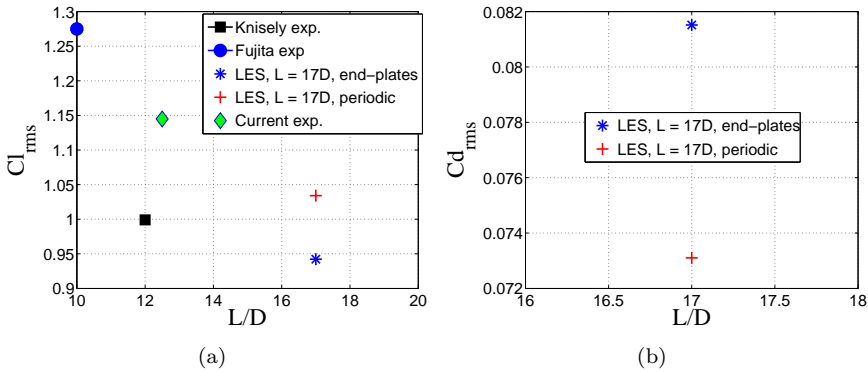


Figure 3.21: Cl_{rms} and Cd_{rms} in case with and without end-plates. Comparison with literature. Knisely [33] $Re_D = 22000$ to 62000 , Fujita [21] $Re_D = 10000$, Current experiment [16], $Re_D = 46000$

periodic case.

3.5.3 Conclusion

In this section a study of the impact of end-plates is presented. Both mean and fluctuating pressure distributions on the walls of the rod are affected by the end-plates. Two symmetric minima of mean pressure on the rear wall are identified in the presence of non-slip end-plates and the spanwise dimension $L = 17D$. Similarly two maxima of fluctuating pressure are present on top and bottom walls. This might be associated with the spanwise correlation length observed in the experiment of Fujita [21]. However the integral coefficients of lift and drag do not show significant differences.

3.6 General conclusion

In this chapter we evaluated the impact of different computational parameters on the velocity and pressure fields at the walls of the rod in order to identify the most crucial parameters for accuracy. In order to predict the tonal sound produced by the rod in a cross-flow we are interested in the accuracy of the forces acting on the walls of the rod.

We examined the influence of mesh resolution close to the rod surface

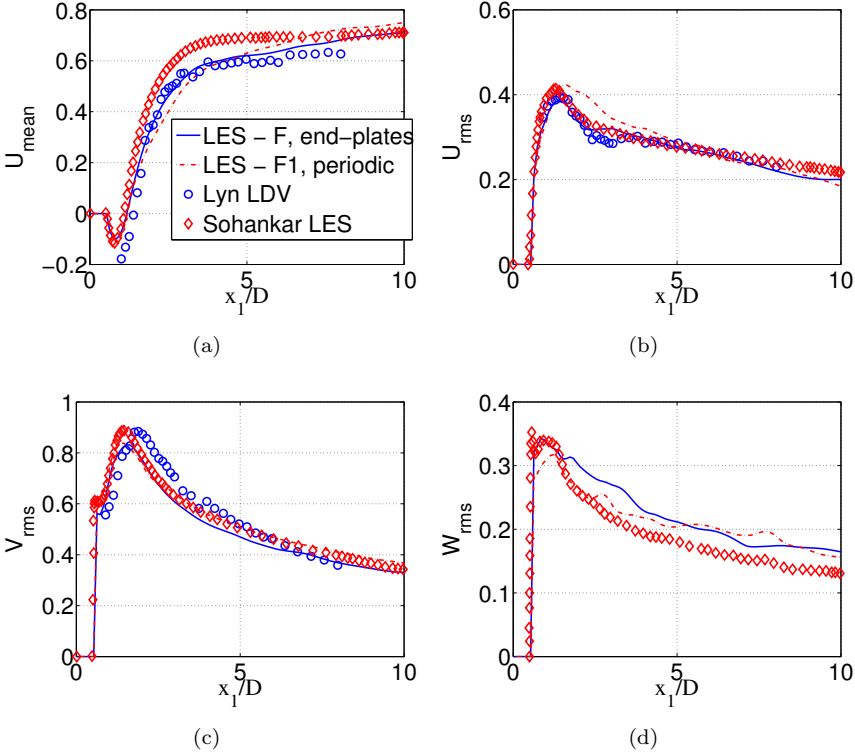


Figure 3.22: Time averaged streamwise velocity U_{mean} and RMS velocity $U_{rms}, V_{rms}, W_{rms}$ at centerline ($x_2 = 0, x_3 = 0$) with and without end-plates. Scaled with U_o . LES, $Re_D = 5000$, Lyn et al. [39], $Re_D = 22000$, Sohankar et al. [58], $Re_D = 22000$.

and using wall functions (section 3.3). It showed that having the first cell within the log-law layer ($y^+ = 60$) gives serious under-prediction of lift and drag fluctuations on the rod. In this study we were limited to thin spanwise domains. This leads to another issue: the domain spanwise width L .

In section 3.4 we explored the influence of the domain span dimension by varying it from $L = 1D$ to $L = 17D$. For this study we used the finest wall resolution from the previous section. It turned out that having $L \leq 8.5D$ the fluctuating forces were overpredicted by up to 50% in the case of $L = 1D$. Nonetheless, 2-d uRANS performed quite well when predicting pressure

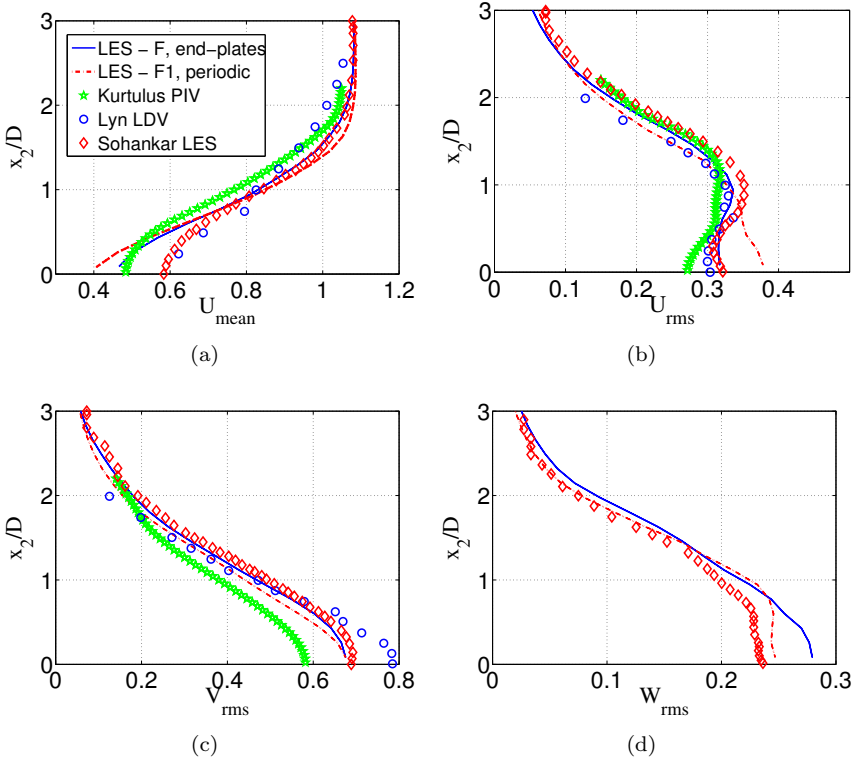


Figure 3.23: Time averaged streamwise velocity U_{mean} and RMS velocity $U_{rms}, V_{rms}, W_{rms}$ at $x_1 = 2.5D$ with and without end-plates. Scaled with U_o . Kurtulus [35], $Re_D = 5000$, Lyn et al. [39], $Re_D = 22000$, Sohankar et al. [58], $Re_D = 22000$.

fluctuations on the rod.

In the last section, 3.5, we analysed the effect of the end-plates. Their presence organises the flow into two spanwise regions visible in both the mean and fluctuating pressure and velocity fields. The average lift and drag coefficients were comparable with the literature data.

Given those results the recommendation for the simulation of the flow around a square rod as a source of tonal sound would be the following:

- Grid resolution at the wall should be enough to model directly the

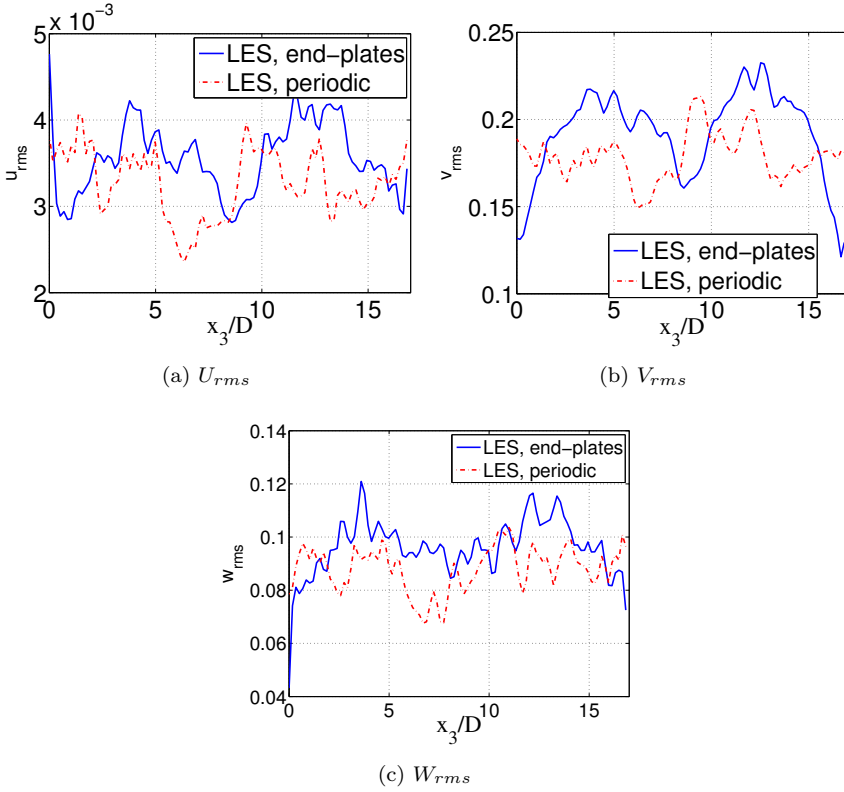


Figure 3.24: Spanwise evolution of velocity fluctuations behind the rear wall of the rod for LES cases with and without end-plates. Scaled with U_o , $Re_D = 5000$

boundary layer and avoid the usage of wall functions. In Fluent [6], this means using $y_{min}^+ < 11$ such that the wall-functions are not activated.

- The spanwise dimension of the domain should be at least of the order of the spanwise correlation ($L \geq 7D$ to $9D$ at $\alpha = 0^\circ$).
- The end-plates introduce a spanwise distribution of flow variables which might be important when the rod is not acoustically compact.

A more in-depth study of the dependence on various angles of attack α is presented in the following chapters.

Chapter 4

Flow around square rod at incidence - LES results and comparison with PIV

In this chapter we describe the results of the LES computations at $Re_D = 5000$ on two mesh resolutions for three angles of attack: $\alpha = 0^\circ$, $\alpha = 13^\circ$ and $\alpha = 45^\circ$. We simulated full span of the square rod using non-slip endplates as spanwise boundary condition. We compare the LES results with uRANS and with data available from the literature for the above selected angles of attack.

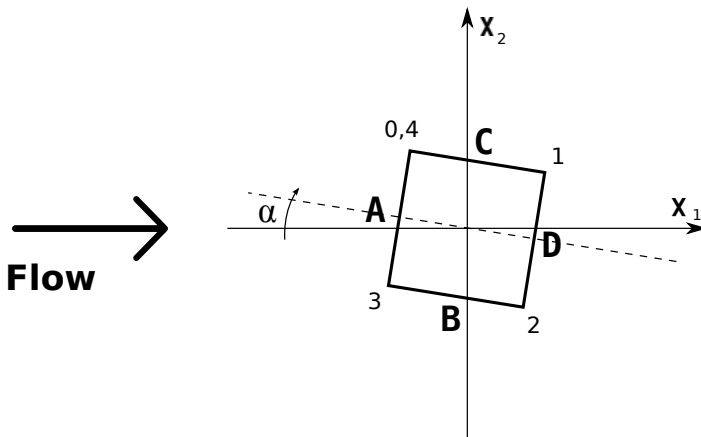


Figure 4.1: Definition of angle of attack α

Definition of angle of attack α used in LES computations can be seen in figure 4.1. It is oriented counter-clockwise.

In this chapter we will consider only the velocity field. In chapter 5 we will compare predicted pressure fields, lift and drag with experimental data.

4.1 Computational model

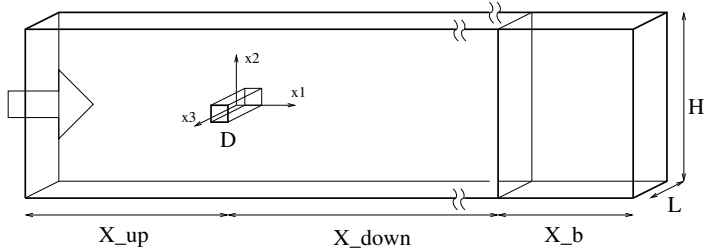


Figure 4.2: LES computational domain

In figure 4.2 we see the geometry of the computational model. The rod is placed in the middle of the domain which is restricted to a box of size $(X_{up} + X_{down} + X_b) \times H \times L$. X_b is the length of a buffer zone consisting of stretched a mesh, as explained in chapter 3, section 3.2. In this chapter the results of two LES models are presented - unresolved LES - G and LES - F resolving the boundary layers around the rod surface.

We provide results for three angles of attack: $\alpha = 0^\circ$, $\alpha = 13^\circ$ and $\alpha = 45^\circ$. The rod is rotated about its axis (x_3). The geometric dimensions of the computational box for LES - G and LES - F for all angles of attack are provided in table 4.1. The span and rod dimensions of case LES - G correspond to the experiment from UTwente [16], and case LES - F to the experiment of Kurtulus et al. [35]. LES - F at zero angle of attack was described already in chapter 3, section 3.5.

	D [m]	L/D	H/D	X_{up}/D	X_{down}/D	X_b/D
LES G	0.036	12	10	18	40	15
LES F	0.03	17	17	10	30	10

Table 4.1: Computational domain dimensions in LES - G and LES - F. For definition of L , D , H , X_{up} , X_{down} and X_b see figure 4.2

Boundary conditions

We apply the following boundary conditions:

- 1 - uniform inlet velocity U_o at the plane $x_1 = -X_{up}$ giving $Re_D = 5000$.
- 2 - a slip wall at planes $x_2 = \pm H/2$

3 - a non-slip wall representing endplates at planes $x_3 = \pm L/2$ and on the surface of the rod

4 - the flow outlet as zero gauge pressure condition at plane $x_1 = X_{down} + X_b$

The calculations were initialised with uniform velocity (equal to the inlet velocity) and atmospheric pressure in the whole computational domain.

4.1.1 Mesh & near wall resolution

The conclusions of chapter 3 provide the following guidelines for the minimum LES requirements:

- The grid resolution close to the rod wall with $y_{min}^+ < 11$, in order not to use wall functions,
- Domain spanwise dimension $L \geq 8.5D$
- Using end-plates with grid resolution also $y_{min}^+ < 11$

The size of the mesh for case LES - G (see table 4.2) follows those requirements. However the spanwise mesh resolution in case G is ranging from $z_{min}^+ < 14$ near the end-plates to $z_{min}^+ < 100$ in the middle of the rod. Its dimensions correspond to the experimental set-up in UTwente [16] which is described in more details in the next chapter 5. LES - G under-resolves the boundary layers, but still avoids using wall functions close to the surface of the rod and the end-plates. Most importantly though, we compute on a model that spans more than 8 times the rod diameter D which should allow for a reasonable prediction of fluctuating forces on the rod surface.

We also solved on a finer mesh case LES - F (discussed in detail in chapter 3 for angle of attack $\alpha = 0^\circ$). In this case we resolve the boundary layer around the rod with $y_{min}^+ < 1.5$, but use blended wall functions on the end-plates where the first cell y_{min}^+ is below 30. The spanwise dimension of case LES - G is $L/D = 17$ which corresponds to the wind tunnel measurements from Kurtulus et al.[35]. The spanwise mesh resolution in case F is ranging from $z_{min}^+ < 30$ at the end-plates and reaching $z_{min}^+ = 100$ in the middle of the rod. This means that case F has poorer spanwise resolution than case G.

Running LES - G it is possible to obtain converged statistics of the flow after 1 week of computing on 8 processors per case. It takes 3-4 weeks on

16 processors per case to obtain comparably converged results for case LES - F.

The mesh characteristics are summarised in table 4.2. It can be seen that in LES - G at angle of attack $\alpha = 0^\circ$ the y_{min}^+ near the rod surface exceeds the limit of 11. In that case the solver automatically activated the use of wall functions [6]. All the other cases solved in this chapter do not employ wall functions near the surface of the rod.

α	LES - G 0°	LES G 13°	LES G 45°	LES F 0°	LES F 13°	LES F 45°
x_{min}^+ at the rod	< 20	< 20	< 20	< 20	< 20	< 20
y_{min}^+ near rod	< 12	< 8	< 9	< 1.5	< 1.2	< 1.1
y_{min}^+ near end-plates	< 9	< 11	< 11	< 30	< 30	< 30
N_{x_3}	80	80	80	128	128	128
z_{min}^+ near end-plates	< 14	< 14	< 14	< 30	< 30	< 30
z_{min}^+ middle of the rod	< 100	< 100	< 100	< 100	< 100	< 100
No. of cells (mln)	0.975	1.485	1.475	4.7	4.7	4.7

Table 4.2: Mesh characteristics LES - G and LES - F. x_{min}^+ , y_{min}^+ and z_{min}^+ are the streamwise, transverse and spanwise mesh resolutions, N_{x_3} is the number of cells in spanwise direction

In order to construct a quadrilateral mesh a block structure seen in figure 4.3 is used. The mesh we see is a surface mesh which then is extruded in spanwise direction (x_3) creating a volume mesh. The detailed mesh view for LES - G can be seen in figure 4.4 for all three angles of attack solved.

4.2 Average flow

The PIV measurements, with which we compare our simulations, were performed in a low speed open wind tunnel (W-tunnel) of the Aerodynamic Department of the Faculty of Aerospace Engineering of Delft University of Technology by Roosenboom [52]. The Reynolds number based on the rod width D is $Re_D = 2 \cdot 10^4$. For each angle of attack (here we show 0° , 12.5° and 45°) 1000 images at rate of 3.3Hz were acquired. Roosenboom [52] processed the images using the PIV software package WIDIM [55].

The results of uRANS from van der Weide [63] ($Re_D = 165000$) were sampled at each timestep with frequency of 40kHz and time-averaged over:

- 2 periods of vortex shedding for 0° angle of attack,

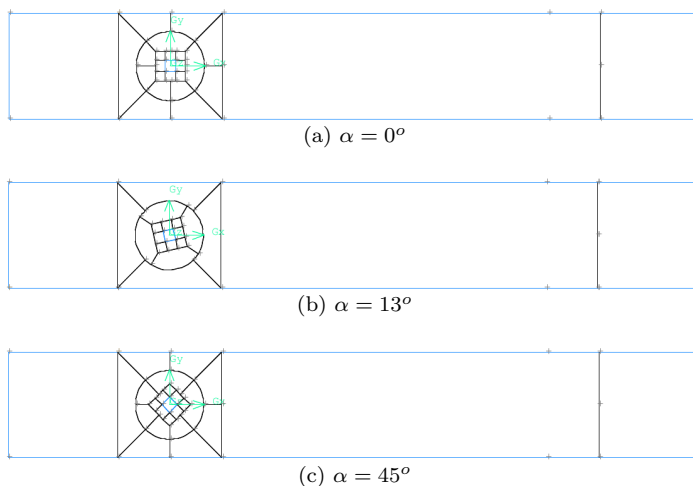


Figure 4.3: Models' block structure for three angles of attack solved (LES - G)

- 9 periods of vortex shedding for 13° angle of attack,
- 4 periods of vortex shedding for 45° angle of attack,

The results of LES - G ($Re_D = 5000$) were sampled at each timestep with frequency of 20kHz and time averaged over:

- 100 periods of vortex shedding for 0° angle of attack,
- 40 periods of vortex shedding for 13° angle of attack,
- 25 periods of vortex shedding for 45° angle of attack,

The results of LES - F ($Re_D = 5000$) were sampled with the same frequency as LES - G and acquired over 40 vortex shedding periods for 0° angle of attack and over 20 periods for angle of attack $\alpha = 13^\circ$ and $\alpha = 45^\circ$.

In figures 4.5, 4.6 and 4.7 we can see the average streamlines and vorticity in the plane $x_3 = 0$ obtained using uRANS and LES compared with PIV [52]. The dark grey square in PIV results is the rod cross-section. The light grey color marks the region where the PIV results were not reliable due to reflections from the surface of the rod.

For the angle of attack $\alpha = 0^\circ$ (figure 4.5) all the numerical simulations predict well the near wake recirculation zone length. The average flow is

symmetric with respect to the horizontal plane ($x_2 = 0$). The surface-oil flow visualisations by Huang [24] suggest the presence of a recirculation bubble on top and bottom walls. The resolved LES - F reproduces this recirculation. However using uRANS and LES not resolving the boundary layer (LES - G) we do not obtain the secondary recirculation bubble on top and bottom walls of the rod. This bubble is not visible in PIV due to reflection from the wall.

At angle of attack $\alpha = 13^\circ$ the uRANS averaged over 9 shedding periods gives a streamline pattern (figure 4.6) that disagrees with the experimental data and the LES results. The average flow is no longer symmetric. Both LES cases show the vortex shed from the left (upstream) corner on the top and right (downstream) corner on the bottom of the rod. In LES - G we see two recirculation bubbles on the top wall which are not present in refined LES - F case.

At angle of attack of 45 degrees (figure 4.7) the average flow is again symmetric. When using uRANS the near wake length has half the length observed in experiment and LES. uRANS and LES show a secondary recirculation at the rear sides, which does not appear in the perfect wedge flow described by Huang [24] and is not visible in PIV results from Roosenboom [52]. The data set length for numerical simulations at this angle is relatively short.

In general LES - F provides the best comparison of after-rod recirculation length, while u-RANS tends to give a short wake which is twice shorter than PIV results for angle of attack 45° .

4.3 Flow statistics

In figures 4.8, 4.9 and 4.10 we present the time averaged velocity magnitude for the three angles of attack considered. The recirculation zone is longer with increasing angle of attack. The uRANS gives a reasonable time averaged velocity only at zero degree angle of attack.

At all angles of attack the speed-up zones and the low velocity zones are best predicted by LES - F. Case LES - G yields a shorter zone of low velocity in the wake than LES - F and PIV.

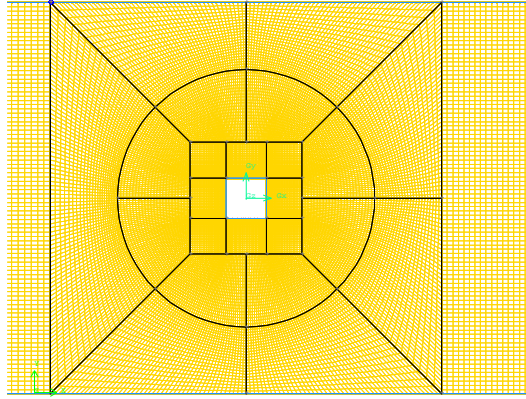
When considering the root mean square of fluctuations in the velocities, we see that LES has maxima of U_{rms} close to the downstream corners of the rod at $\alpha = 0^\circ$ which is not so pronounced in PIV and uRANS (figure 4.11). At angle $\alpha = 13^\circ$ the LES - F predicts a peak of U_{rms} close to the lower down-stream corner of the rod - this is not visible in other cases

(figure 4.12). At $\alpha = 45^\circ$ (see figure 4.13) the uRANS fails to predict U_{rms} giving the maximum values about three times lower than in LES and the experiment.

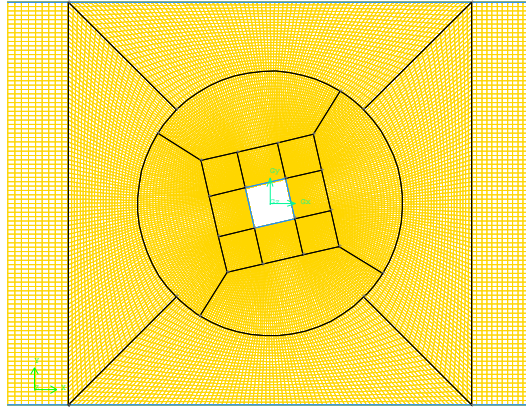
The LES prediction of the fluctuation of stream-wise (U_{rms}) and transverse (V_{rms}) velocities is about 10% lower than the experimental data (see maps in figures 4.11, 4.12, 4.13, 4.14, 4.15, 4.16). W_{rms} data is not available from the two-dimensional uRANS [63] and PIV [52]. At angle 45° the W_{rms} obtained in case LES - G is twice higher than that of LES - F.

4.4 Instantaneous flow pattern

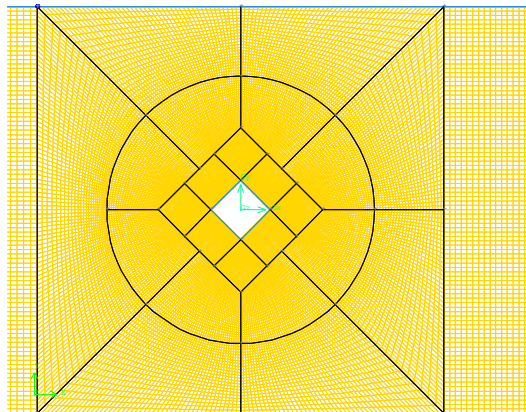
Figures 4.18, 4.20 and 4.22 show the instantaneous flow pattern calculated with LES - F for three angles of attack $\alpha = 0^\circ$, 13° and 45° for one oscillation period. These flow patterns are quite similar to the phase averaged flow snapshots presented by Roosenboom shown in figures .



(a) $\alpha = 0^\circ$



(b) $\alpha = 13^\circ$



(c) $\alpha = 45^\circ$

Figure 4.4: Models' mesh for three angles of attack solved (LES - G)

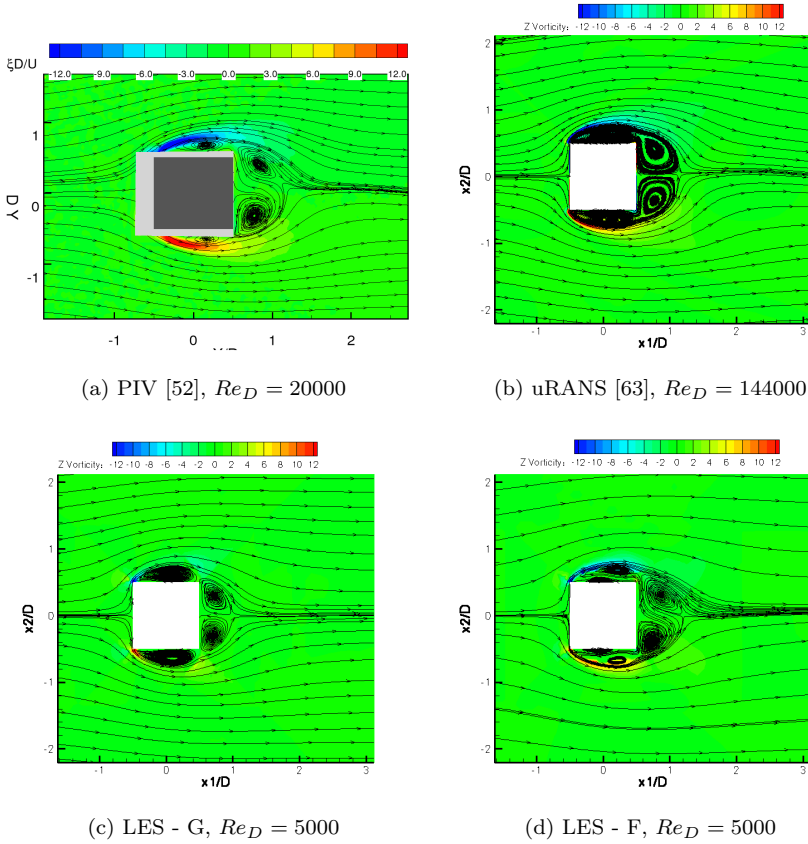


Figure 4.5: Average streamlines on background of vorticity. Angle of attack $\alpha = 0^\circ$

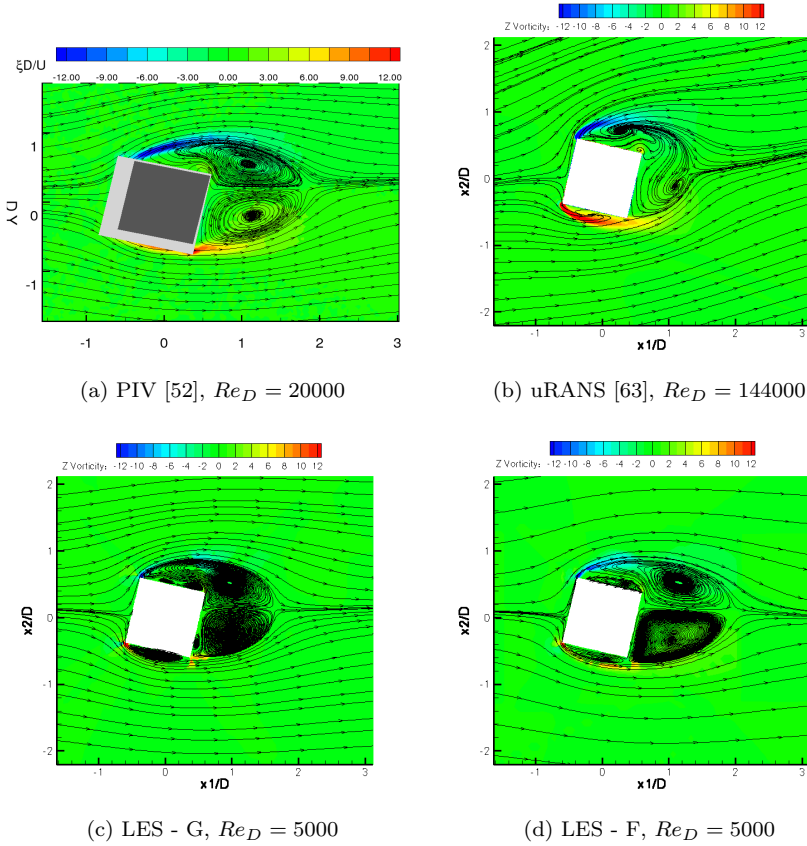


Figure 4.6: Average streamlines on background of vorticity. Angle of attack $\alpha = 13^\circ$

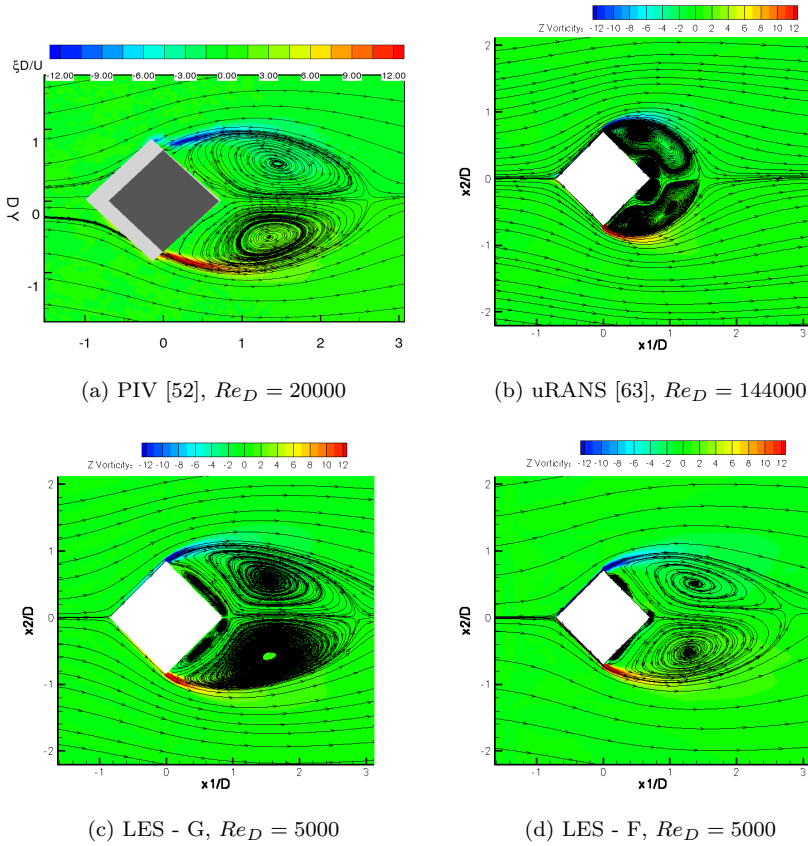


Figure 4.7: Average streamlines on background of vorticity. Angle of attack $\alpha = 45^\circ$

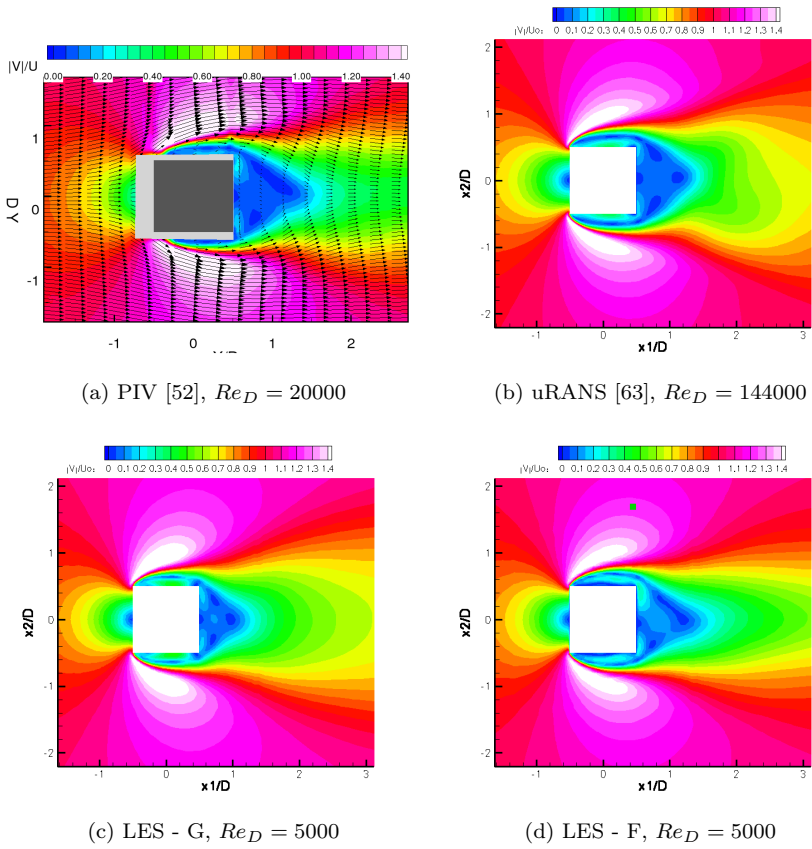


Figure 4.8: Mean velocity magnitude. Angle of attack $\alpha = 0^\circ$

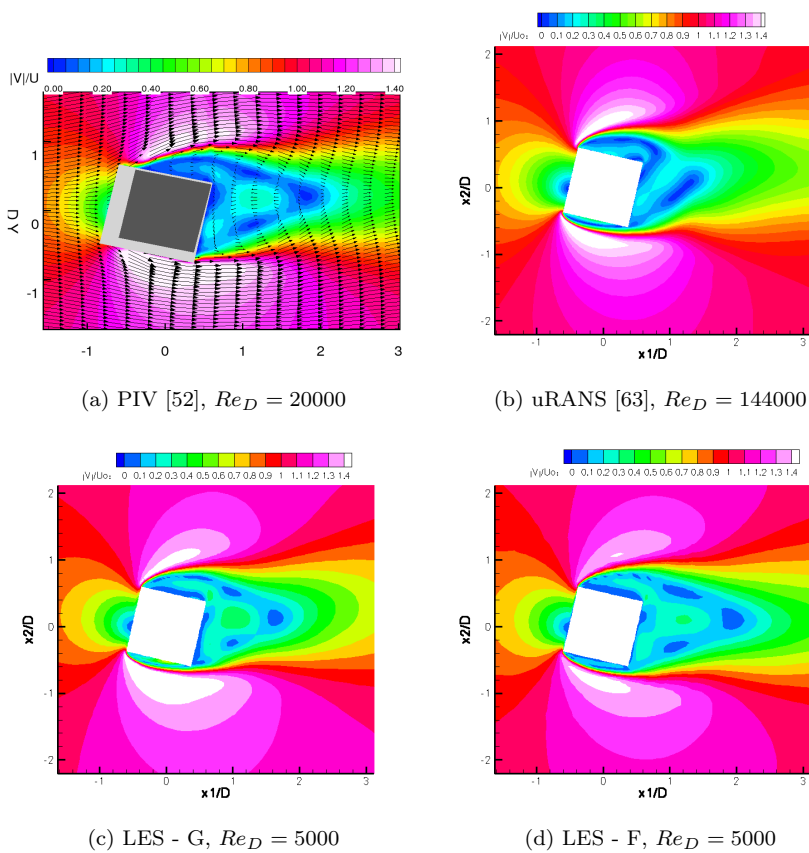


Figure 4.9: Mean velocity magnitude. Angle of attack $\alpha = 13^\circ$

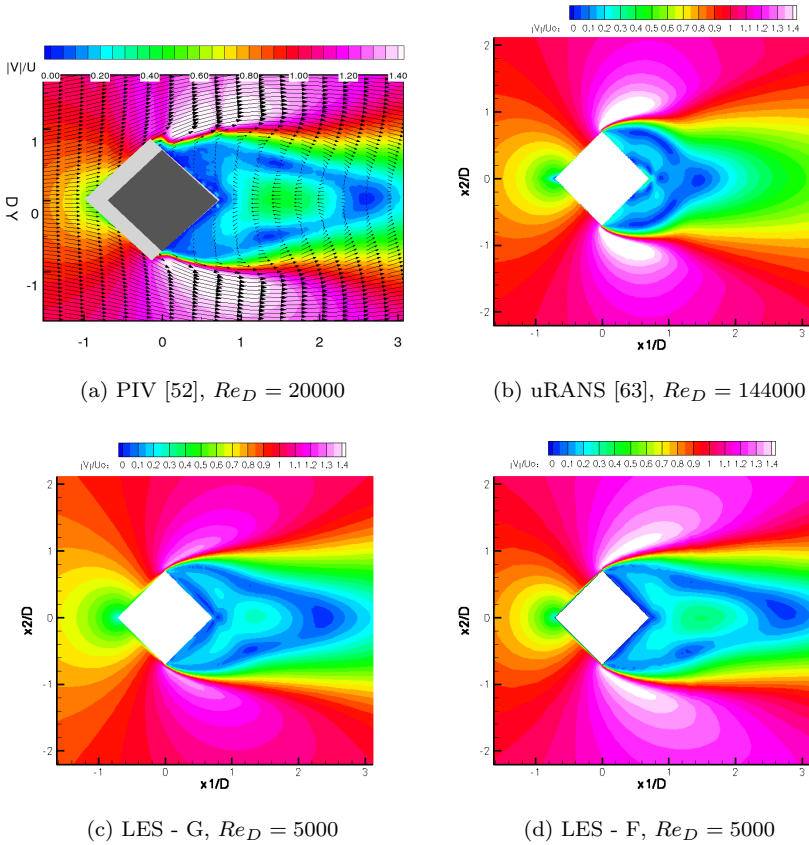


Figure 4.10: Mean velocity magnitude. Angle of attack $\alpha = 45^\circ$

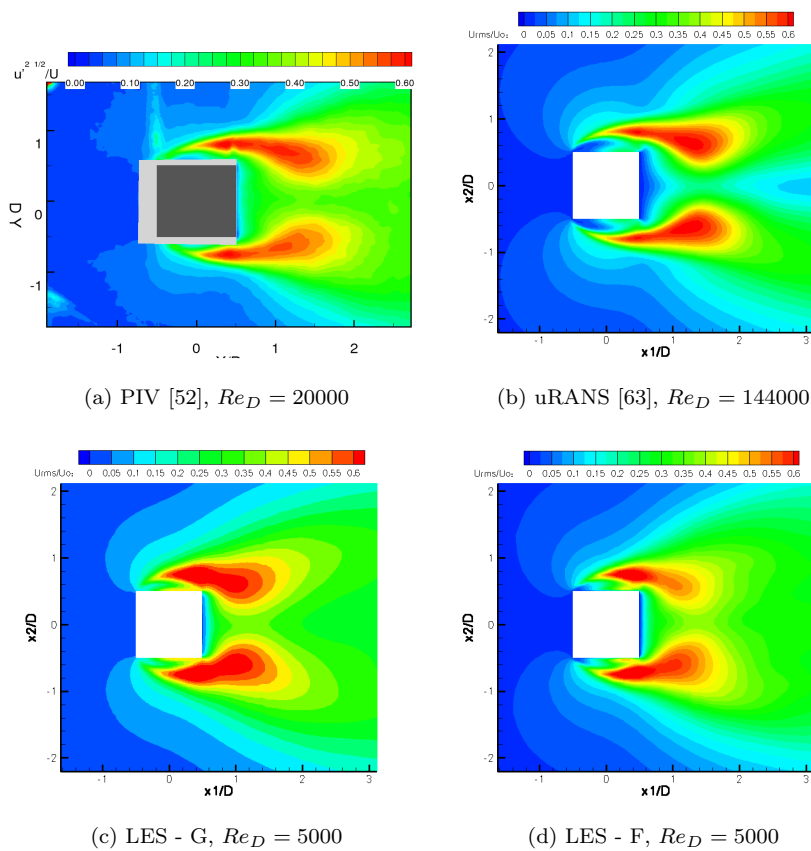


Figure 4.11: U_{rms} . Angle of attack $\alpha = 0^\circ$

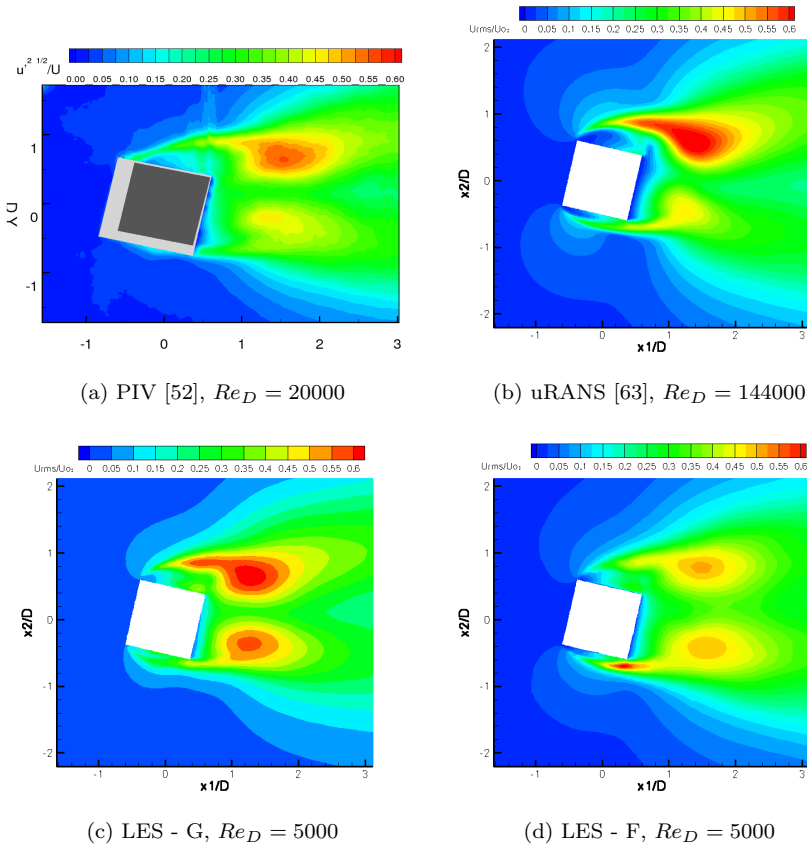


Figure 4.12: U_{rms} . Angle of attack $\alpha = 13^\circ$

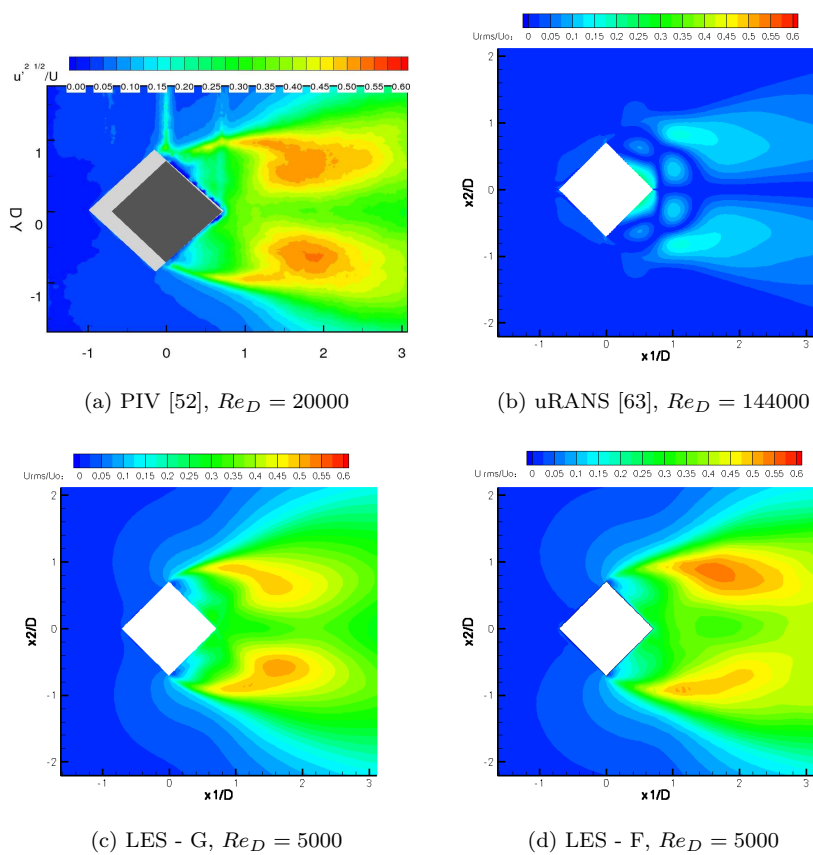


Figure 4.13: U_{rms} . Angle of attack $\alpha = 45^\circ$

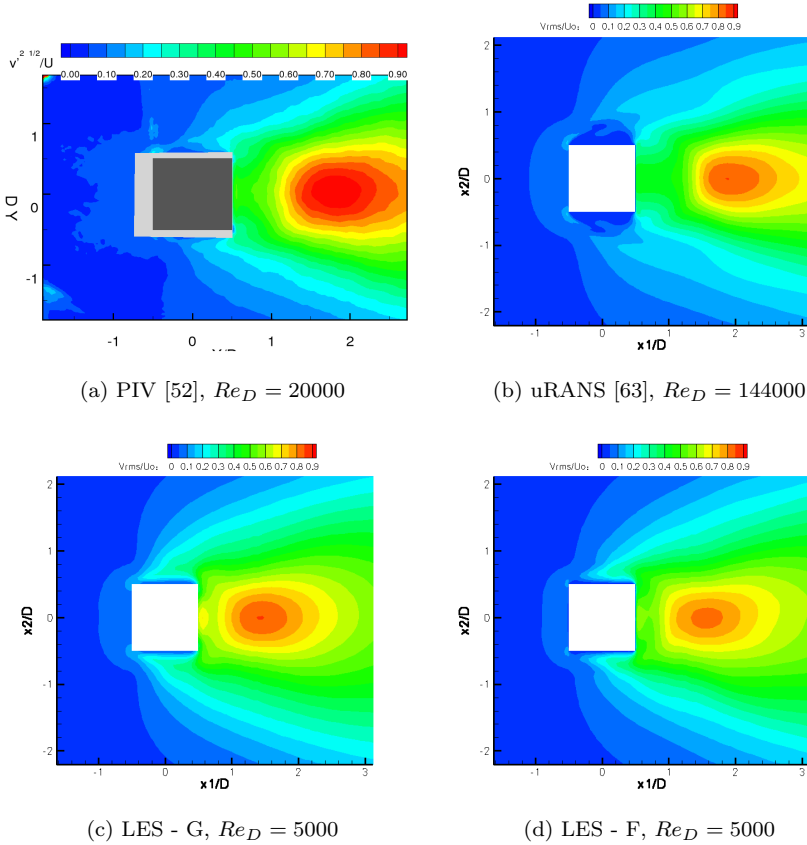


Figure 4.14: V_{rms} . Angle of attack $\alpha = 0^\circ$

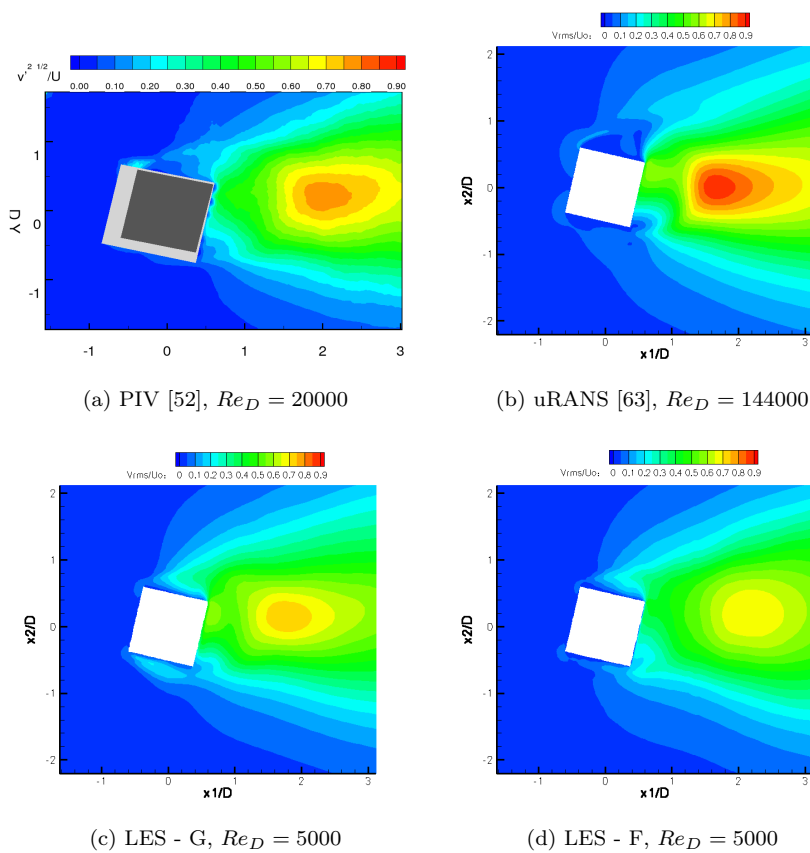


Figure 4.15: V_{rms} . Angle of attack $\alpha = 13^\circ$

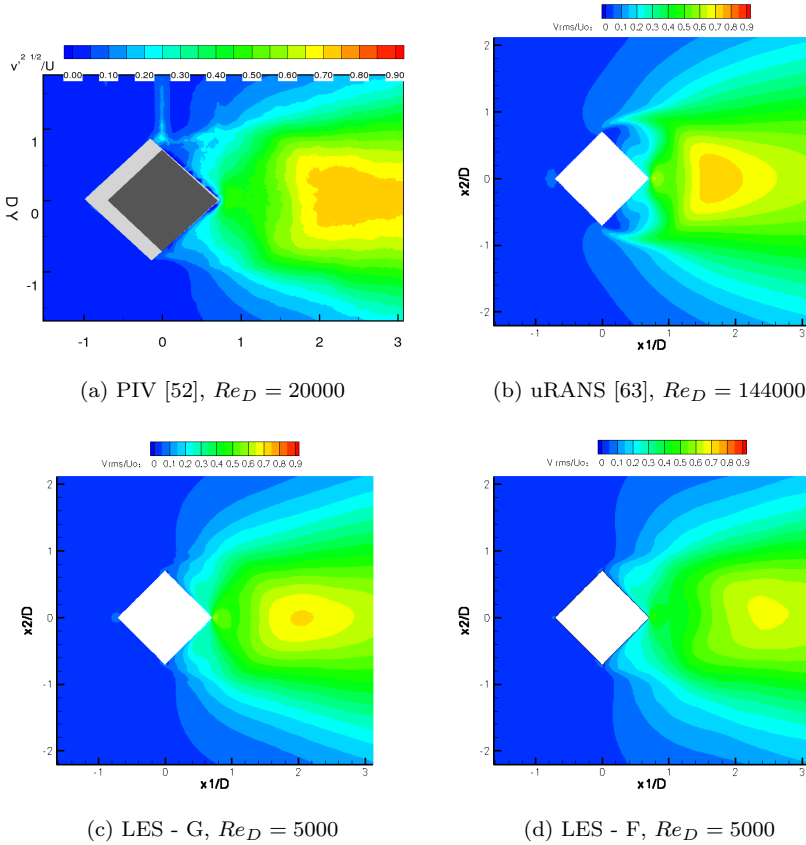
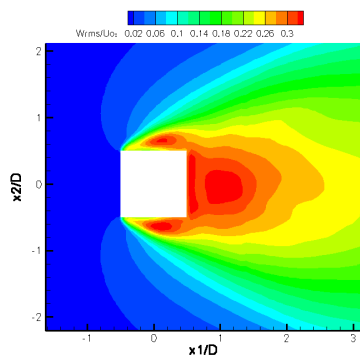
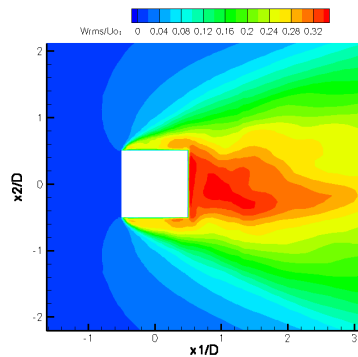


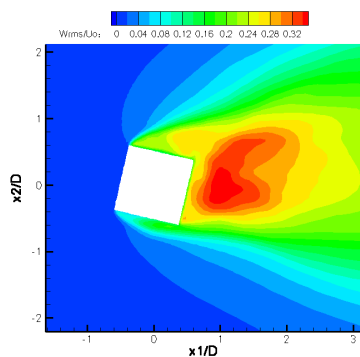
Figure 4.16: V_{rms} . Angle of attack $\alpha = 45^\circ$



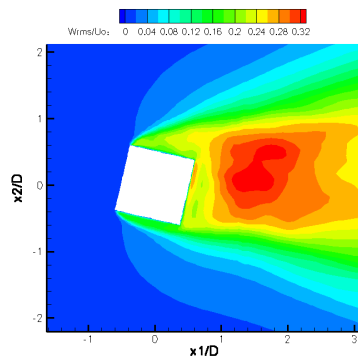
(a) LES - G, $Re_D = 5000$, $\alpha = 0^\circ$



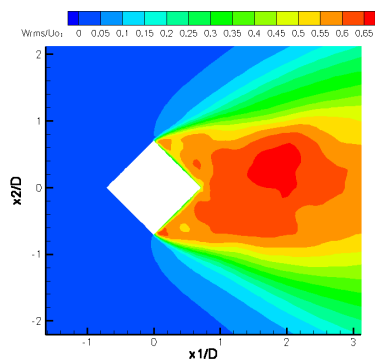
(b) LES - F, $Re_D = 5000$, $\alpha = 0^\circ$



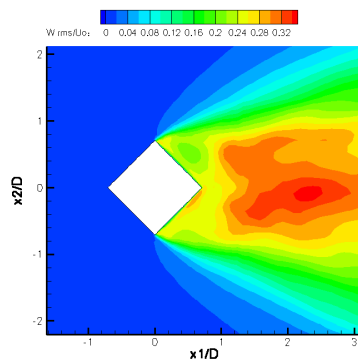
(c) LES - G, $Re_D = 5000$, $\alpha = 13^\circ$



(d) LES - F, $Re_D = 5000$, $\alpha = 13^\circ$



(e) LES - G, $Re_D = 5000$, $\alpha = 45^\circ$



(f) LES - F, $Re_D = 5000$, $\alpha = 45^\circ$

Figure 4.17: W_{rms} computed by LES.

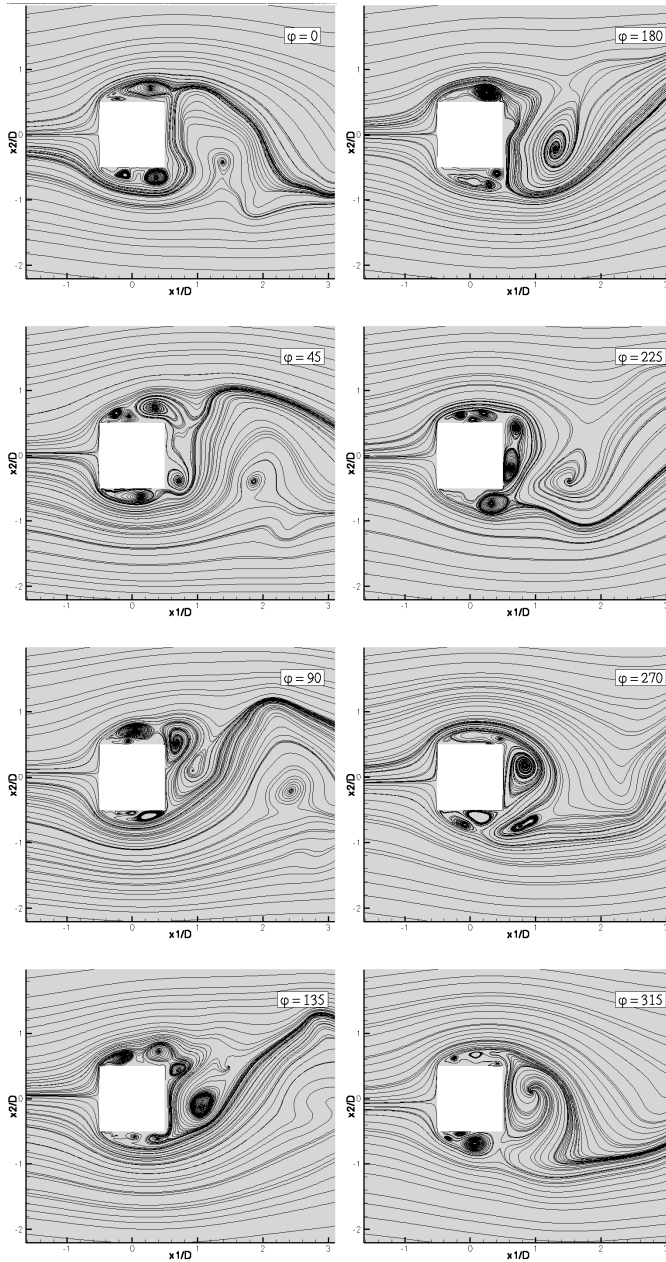


Figure 4.18: Instantaneous flow pattern. Angle of attack $\alpha = 0^\circ$. $\phi = 90^\circ$ at minimum lift.

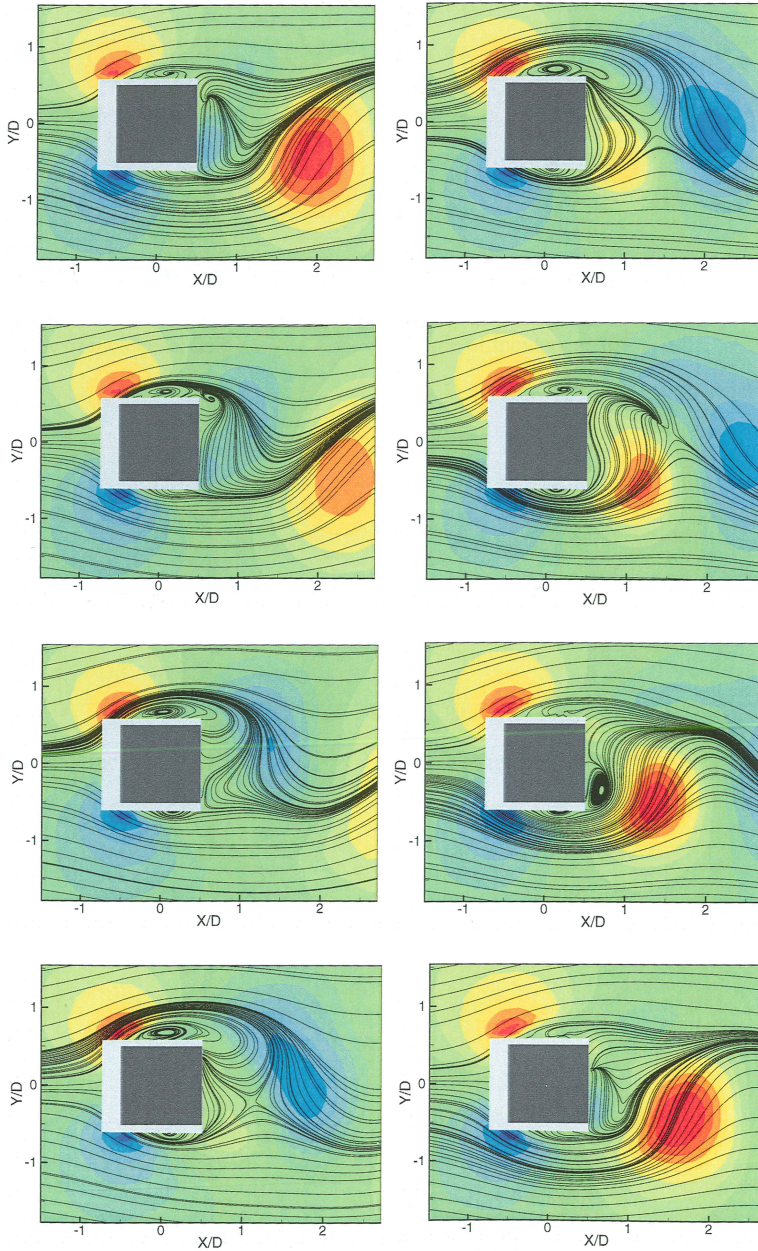


Figure 4.19: Low-order phase reconstructed flow obtained using PIV [52]. Angle of attack $\alpha = 0^\circ$. Time sequence increasing in columns.

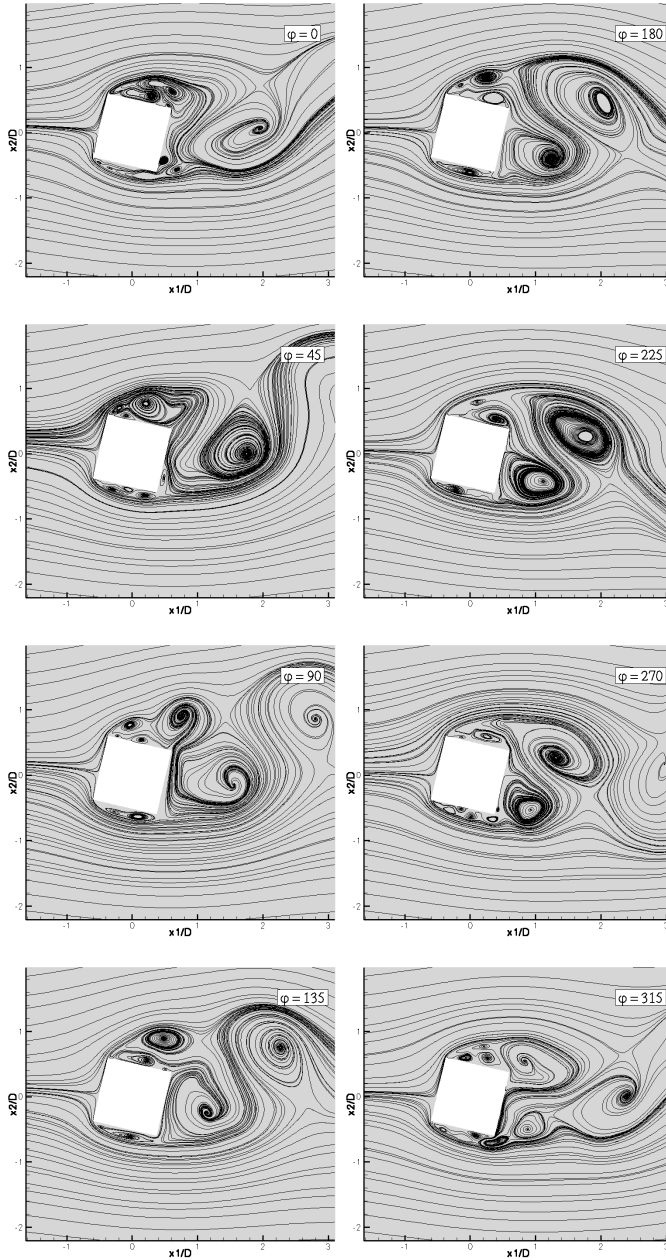


Figure 4.20: Instantaneous flow pattern. Angle of attack $\alpha = 13^\circ$. $\phi = 90^\circ$ at minimum lift.

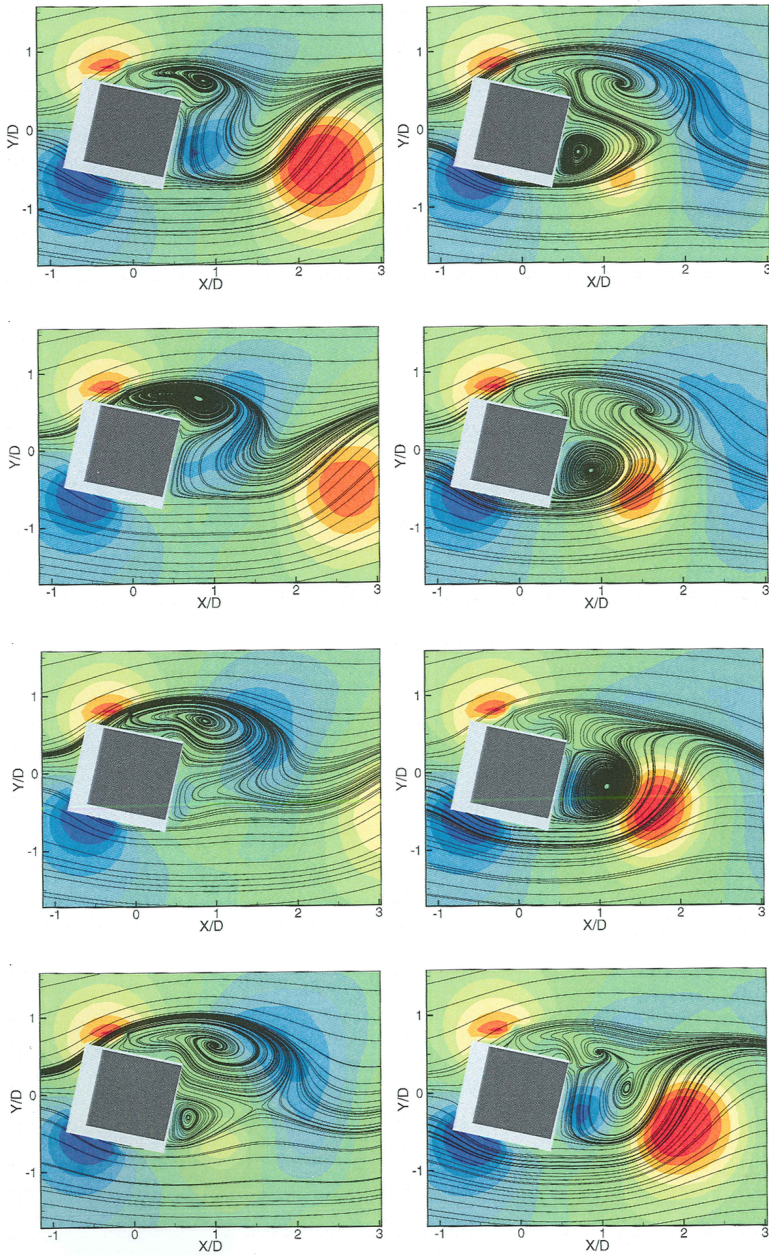


Figure 4.21: Low-order phase reconstructed flow obtained using PIV [52]. Angle of attack $\alpha = 12.5^\circ$. Time sequence increasing in columns.

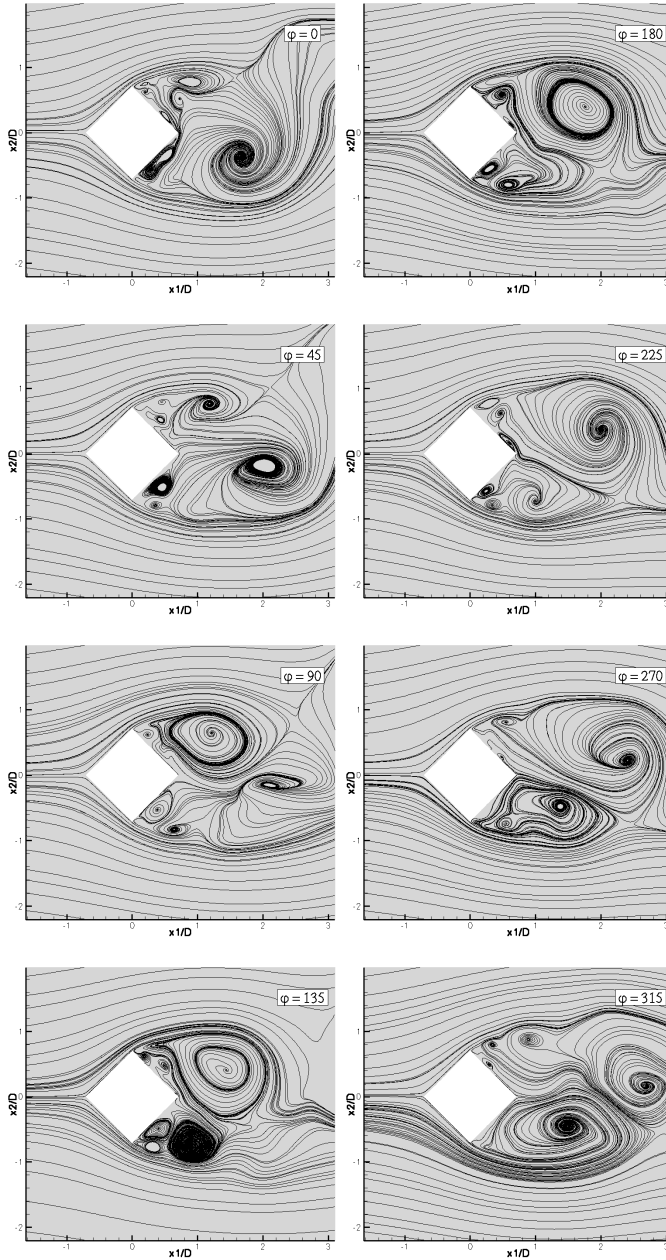


Figure 4.22: Instantaneous flow pattern. Angle of attack $\alpha = 45^\circ$. $\phi = 90^\circ$ at minimum lift.

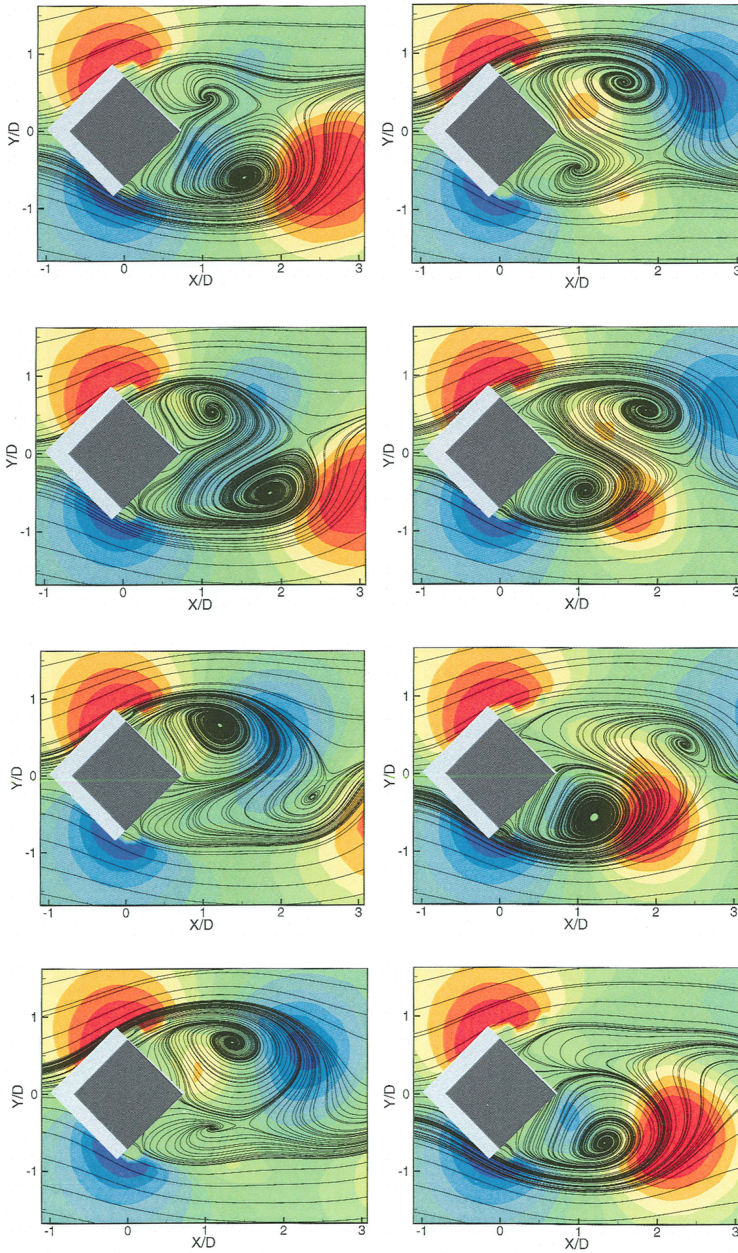


Figure 4.23: Low-order phase reconstructed flow obtained using PIV [52]. Angle of attack $\alpha = 45^\circ$. Time sequence increasing in columns.

4.5 Conclusion

We compared the velocity field measured experimentally by means of PIV by Roosenboom [52] to the numerical results.

The two-dimensional compressible uRANS calculation gives acceptable flow statistics only at zero degree angle of attack. The uRANS near-wake recirculation length is considerably smaller than observed in experiments.

Under-resolving the boundary layer (LES - G) causes some loss of flow features. At zero degree angle of attack having y_{min}^+ reaching 12 (LES - G) a secondary recirculation bubble on the rod side walls is not captured.

The wall resolved LES - F are in fair agreement with available PIV data [52]. However the cost of this simulation is considerably higher than case G.

The pressure and force analysis of the cases presented in this chapter will be described in the next chapter together with the sound prediction based on fluctuating lift.

Chapter 5

Aerodynamic tonal sound generated by square rod at incidence - experiment and numerical prediction

5.1 Introduction

Flow around bluff bodies is intrinsically unstable. This results into a fluctuating force exerted by the flow on the body. The reaction to this force acting on the fluid is a source of sound. It is a dipolar source of sound which will dominate at low subsonic flow speeds.

Under certain conditions the instability of the wake results in periodic vortex shedding characterised by a nondimensional Strouhal number $St_D = fD/U_o$, product of frequency f and convection time D/U_o , where D is the characteristic width of the body and U_o the main flow mean velocity. Whistling of cylinders in cross flow has been extensively studied since the early work of Strouhal[59]. More recently the sound produced by rods with rectangular or square cross sections have received considerable attention in view of applications in civil engineering. We consider here the generic case of a rod with square cross-section to explore our ability to predict the sound production by such complex unsteady flow using a commercial incompressible LES solver. On the longer term we would also like to predict the broad band noise, but we focus here on the tonal sound.

Computing aerodynamic sound by solving directly the compressible Navier-Stokes equations is still prohibitive for industrial problems [66]. Flows with high Reynolds number require very small time steps and very large grid resolutions. Furthermore, at low Mach numbers the acoustic far-field begins at large distances from the source region and requires the meshing of a large domain. We consider therefore an alternative hybrid approach suited to low-Mach number applications, where the computation of the flow is decoupled from the acoustic propagation problem.

We discuss here in detail the pressure and sound field of two cases already

described in chapter 4 where we analysed the velocity field. We call them LES - G and LES F. We have also the uRANS data obtained by van der Weide [63]. We compare our numerical simulations with data from the literature and our measurements obtained in the silent wind tunnel of UTwente [16].

The aerodynamic sound is generated by unsteady reaction forces of the rod on the fluid. These forces on the rod can be characterised by integral coefficients of lift (C_l) and drag (C_d). Mainly the configuration of a square cross section rod at zero angle of attack has been researched and there is information about mean and fluctuating drag as well as the characteristic frequencies available in numerous experimental and numerical papers [9, 27, 35, 47, 58]. Knisely [33], Norberg[45] and Taylor[61] provide the information on C_l and C_d as a function of angle of attack (see fig. 5.1). The oscillating forces are dominated by periodic vortex shedding at specific Strouhal numbers reported by Okajima[47], Norberg[45], Knisely[33] and Chen[13]. There is some information in literature on the amplitude of fluctuating C_l and C_d as a function of the angle of attack [33]. The sound generated by a square

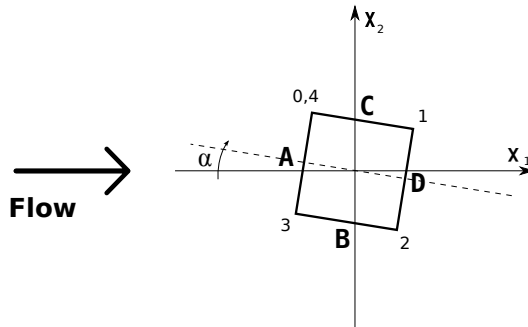


Figure 5.1: Definition of angle of attack α

rod at incidence was studied previously by Fujita[21] and Hutcheson[25]. For more complete literature review of the flow aspects see chapter 2.

In section 5.2 we describe the experimental facility and measurement procedure.

In section 5.3 we describe the numerical simulations: LES and uRANS.

In section 5.4 we compare the numerical results to the experimental data such as the time averaged pressure coefficient C_p , the whistling Strouhal number St_D , the amplitude of the fluctuating lift and drag forces and the coherence of these fluctuations along the rod. The flow field has been compared to PIV measurements of Roosenboom [52] in chapter 4.

In section 5.5 we describe a procedure for the prediction of the radiated tonal sound.

In section 5.6 we compare the predicted whistling tone amplitude and frequency to the measurements and literature data.

5.2 Experimental set-up

The aim of our experiment is to obtain quantitative information about the sound generated by a rod with square cross section placed with its axis normal to the flow. We focus on the whistling sound generated by the oscillation in the lift force. The rod cross section width is $D=0.036$ m. The rod length is $L = 12.5D = 0.450$ m. Its surface is polished and edges have been kept as sharp as possible. The surface of the rod has been painted in black to allow future PIV measurements. This paint limits the radius of curvature of the edges to 0.1 mm. The rod is hollow, with a wall thickness of 2 mm. 26 holes of diameter 0.5 mm are drilled in the rod in the plane $x_3 = -0.18$ m (figure 5.2a) and $x_3 = 0.09$ m (figure 5.2b). The positions of the static pressure holes are indicated in figure 5.2. The coordinate system (x_1, x_2, x_3) can be seen in figure 5.6. Each hole is connected to a metal tube and a silicon

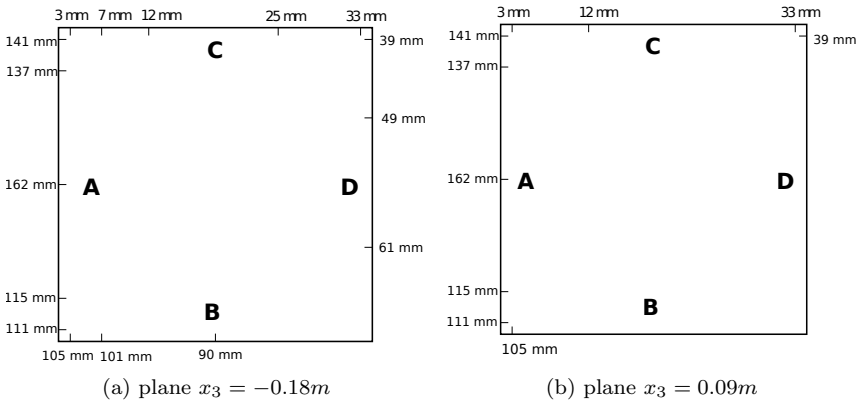


Figure 5.2: Position of static pressure holes. Upper left corner is where the surface coordinate S has origin.

hose connected to a manometer. This Esterline pressure scanner delivers the static pressure measurements to a Chell CANdap pressure acquisition sys-

tem. These static pressure measurements are used to characterize the flow. The rod is mounted horizontally to two vertical plexiglass plates fixed to

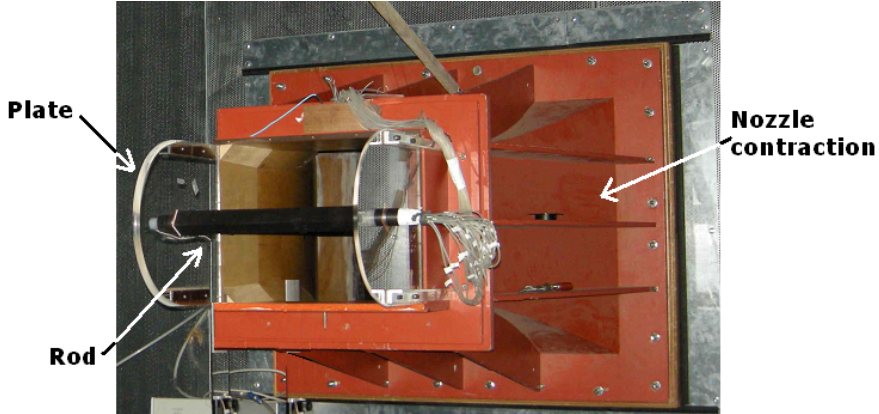


Figure 5.3: Set-up with plexiglas end-plates

the sides of the nozzle exit ($0.45 \text{ m} \times 0.35 \text{ m}$) of the silent wind tunnel of UTwente (Figure 5.3). The plates have a length in the flow direction of 0.575 m and a height of 0.350 m . The trailing edge of the plates forms a semi-circle of 0.175 m radius. The rod is placed at the centre of this circle, which corresponds to a distance of 0.400 m from the nozzle outlet. The trailing edges of the 12 mm thick side-plates are rounded in order to reduce broad band flow noise. The rod can be rotated around its axis to change its angle of attack α (for definition see figure 5.1). This angle is measured within 0.1 degree by means of an electronic level meter using the bottom plate of the nozzle as a reference.

The silent wind tunnel of UTwente (Figure 5.4) is a closed circuit free jet facility driven by a centrifugal fan. The noise from the fan is attenuated by two silencers located on either sides of the fan. Upstream of the downstream silencer a water cooling system controls the temperature of the flow. The small nozzle ($0.45 \text{ m} \times 0.35 \text{ m}$) allows reaching a velocity of 75 m/s . The turbulence level of the flow at the nozzle exit is 0.2% . The center of the nozzle exit is at 1.10 m from the vertical wall and at 1.70 m from the floor of the anechoic room ($V=4 \text{ m} \times 6 \text{ m} \times 6 \text{ m}$) used for the acoustical measurements. On the opposite vertical wall there is a flush circular intake. The intake has an edge radius of curvature of 0.5 m and leads to a duct of 1.4 m cross section radius.

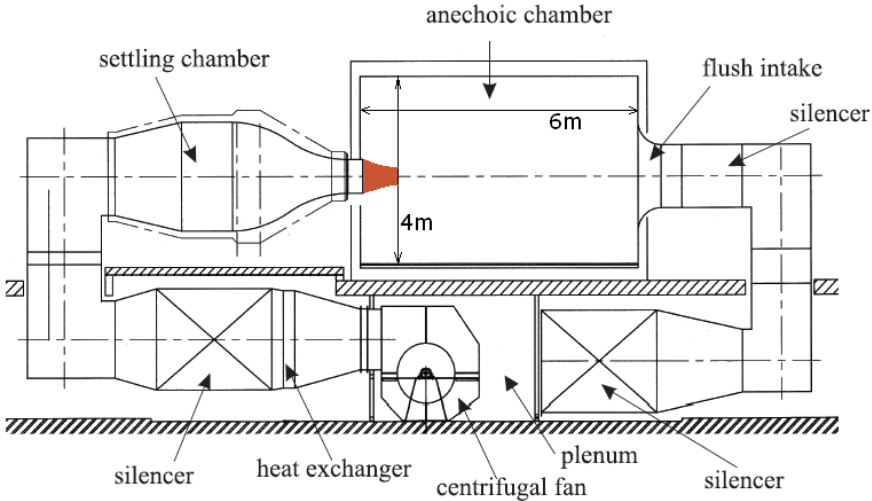


Figure 5.4: Silent wind tunnel and anechoic room of the Univeristy of Twente

The acoustic measurements are obtained by means of two LinearX microphones (type M51). The position $\vec{x} = (x_1, x_2, x_3)$ of the microphones is determined with respect of a coordinate system with the centre of the rod as origin. The x_1 axis is directed in the main flow direction. The x_2 axis is normal to the flow and the rod axis pointing in the vertical direction. The x_3 axis is along the rod axis following the right hand rule. The microphone positions are $\vec{x}_I = (0.21m, 0.55m, 0m)$ and $\vec{x}_{II} = (0.21m, -0.55m, 0m)$. These positions have been chosen within the reverberation radius of the anechoic room associated with the whistling frequencies. For the velocity range considered $20m/s \leq U_o \leq 75m/s$ the whistling frequency is in the range $63Hz \leq f \leq 315Hz$. The corresponding 60 dB reverberation time of the room is in the range $1.77s \geq T_{60} \geq 0.15s$. The reverberation radius r_r , within which the acoustic field corresponds to free field conditions, can be estimated from the formula $r_r \approx \sqrt{55.3V/(16\pi T_{60}c_0)}$, where c_0 is the speed of sound in air. We find $0.5m \leq r_r \leq 1.8m$. Placing an unflanged loudspeaker (representing a dipole) directed towards the x_2 axis, we found that indeed in the $x_3 = 0$ plane, the free field conditions are well approximated within a distance $r_r \approx 1m$. For this dipole in the x_2 direction reflections by the nozzle and the settling chamber were negligible ($0.1dB$). When the loudspeaker is placed in the flow direction, we observe a resonance of the settling chamber

around $f = 220Hz$, for which deviations of $3dB$ from free field conditions are observed. Reflections of sound on the side plates supporting the rod are significant. We propose a theoretical correction for this effect based on the method of images in section 5.5.

Microphones were calibrated by using a BK reference source (1 kHz) before each experiment.

By correlation of the signals of opposite microphone pairs as proposed by Blake [10] we are able to focus on the sound production by the rod.

$$S_{p_I p_{II}}(\omega) = p_I(\omega)p_{II}^*(\omega) \quad (5.1)$$

$S_{p_I p_{II}}$ is the cross-spectra density of the Fourier transforms of the pressures p_I and p_{II} registered by microphone x_I and x_{II} , respectively. Using Parseval's theorem the root mean square of the time dependent discrete signal p_{rms} can be expressed as:

$$p_{rms} = \sum_n \frac{|S_{p_I p_{II}}|}{n^2} \quad (5.2)$$

where n is the number of frequency samples. Without rod the broad-band Sound Pressure Level (SPL) measured by microphone x_I at a distance of 0.59m from the rod is $76dB$ at $20m/s$ and $97dB$ at $60m/s$. The sound pressure level is defined by:

$$SPL = 20\log_{10}\left(\frac{p_{rms}}{p_{ref}}\right) \quad (5.3)$$

where p_{rms} is the root mean square amplitude of pressure fluctuations and $p_{ref} = 20\mu Pa$

We will later discuss the broad band flow noise in absence of the rod in more detail. The SPL of the whistling tone is determined by integration of the cross-spectrum of the pressure measured by microphones x_I and x_{II} over the frequency range $0.5Hz < f < 100kHz$. The whistling peak SPL does not differ more than $0.5dB$ for all velocities (integrated within 10dB drop see figure 5.5) from the one integrated over the whole frequency range. We present the sound pressure level as integration of the complete spectrum, unless explicitly stated otherwise.

We performed hot-wire measurements in the wake in order to verify the spanwise coherence length of vortex shedding reported by Fujita [21].

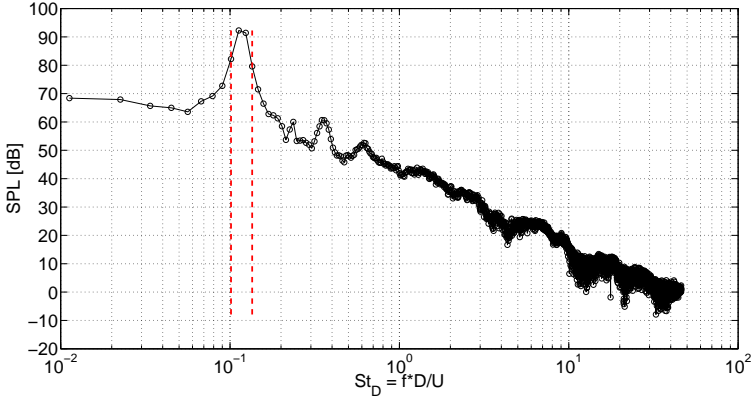


Figure 5.5: SPL of sound measured at $U_0 = 20\text{m/s}$ and $\alpha = 0^\circ$. Red lines show the region of integration. The difference between the power contained within that region and full spectrum is lower than 0.5dB .

5.3 Numerical simulations

Details of the simulations parameters are provided in chapter 3 and 4. We use here data corresponding to cases LES - G and LES - F described in chapter 4. We recall here some essential aspects.

We use a hybrid approach to predict the acoustic pressure. The incompressible Large Eddy Simulation (LES) provides time history of unsteady pressure and velocity fields around the rod. In the LES approach we solve the filtered Navier-Stokes equations resolving directly the most energetic flow features. The aerodynamic calculations were performed using Fluent version 6.3[1]. Filtering is accomplished implicitly by the mesh sizing. The smaller eddies are modelled by a Boussinesque-like analogy of subgrid scale viscosity. In this work we used a Wall-Adapting Local Eddy-Viscosity (WALE) model [44], which is suited for solving wall bounded flows (see section 3.1.3.1).

Geometry and Mesh

The computational domain of an LES case can be seen in figure 5.6. A rod with square cross section of width D and length L is positioned in a fluid domain extending X_{up} upstream the rod, X_{down} downstream + X_b of buffer zone. The angle of attack is set to 0, 13, and 45 degrees (see figure 5.1). The parameters are the same as in the previous chapter (see table 4.1 in chapter 4). Due to limited computational resources it was only possible

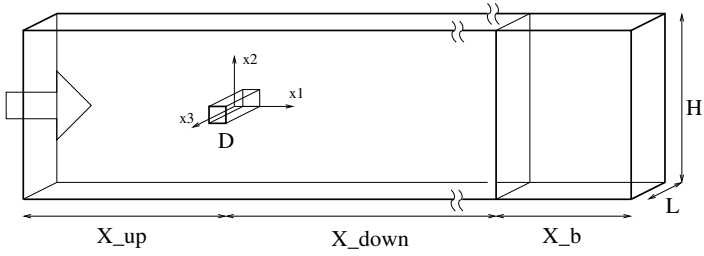


Figure 5.6: Computational domain for LES, dimensions relative to rod width D , fore details see table 4.1 in chapter 4.

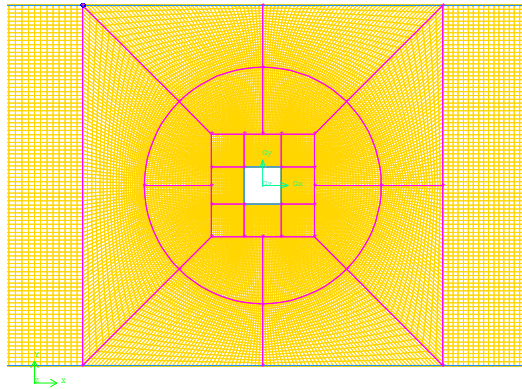


Figure 5.7: LES computational mesh topology near the rod

to run relatively short time series.

The mesh was generated using the Gambit code [8]. A detailed comparative study of mesh and domain size dependency can be found in chapter 3.

In order to use the required mesh resolution at the wall and having limited computing resources it was decided to perform calculations for Reynolds number = 5000. We have access to verification PIV data for $\alpha = 0^\circ$ for this flow regime [35].

Discretisation and boundary/initial conditions

We use a Fluent pressure-based solver to solve the unsteady incompressible Navier-Stokes equations. Velocity and pressure are coupled using the non-iterative PISO method. The discretisation in space and time is of the second order. In order to avoid wiggles a Bounded Central Differencing scheme for convective terms is used. The pressure term is discretised with second order interpolation.

The Courant-Friedrichs-Lewy condition (CFL) is a necessary condition for convergence of unsteady equations when using explicit timestepping. Implicit timestepping employed here is unconditionally stable (is not limited by CFL). Even so, we set the timestep such that the CFL number is lower than 1 for accuracy reasons.

The flow inlet is at the plane $x_1 = X_{up}$. Air at uniform velocity gives Reynolds number $Re_D = 5000$ (based on rod width D). Planes $x_2 = \pm H/2$ have a zero friction slip wall condition. In spanwise direction at planes $x_3 = \pm L/2$ and on the surface of the rod a non-slip wall condition is used. Finally the outlet at plane $x_1 = X_{down} + X_b$ has zero gauge pressure condition. Before the outlet a buffer zone of elongated elements is applied. It ensures that any vortical structure is damped before leaving the domain [40, 42].

The calculations were initialised with uniform velocity and atmospheric pressure in the whole computational domain.

5.4 Flow properties

5.4.1 Steady flow

In a recent paper Huang et al.[24] discussed the flow pattern around a square rod with incidence angle of attack α (see figure 5.1). Flow visualisations suggest the existence of three two-dimensional flow topologies depending on the angle α :

- $0^\circ < \alpha < \alpha_{cr}$ - Subcritical - stagnation point at the face A, separation at the front edges 0 and 3. Alternate vortex shedding in the wake.
- $\alpha_{cr} < \alpha < 45^\circ$ - Supercritical - stagnation point is still at the face A shifted downwards in direction of edge 3. Most of the times a recirculation bubble is formed at the face B. This reattachment is particularly strong around $\alpha = \alpha_{cr}$. Different authors indicate that a critical value of $\alpha = \alpha_{cr}$ varies from 11 to 17 degrees depending on Reynolds number and turbulence levels in the approaching flow [13, 45].
- $\alpha = 45^\circ$ - Wedge flow - bifurcation at the leading edge 3, the flow follows the rod surface and separates at the edges 0 and 2. This configuration is very sensitive to deviation from the symmetrical setting of the angle and the inflow non-uniformity.

Such rod placed in a cross flow generates sound whose level also depends on the angle of attack. Experiments carried out by Fujita [21] show a sharp decrease in SPL by about $15dB$ around $\alpha = 13$ degrees corresponding to α_{cr} .

5.4.2 Steady Pressure

In case of a sharp-edged body, for which the separation points are fixed at the leading edges, the aerodynamic characteristics are relatively insensitive to Reynolds number [11]. This was documented for Reynolds numbers up to order 10^4 [45, 47]. However, below $Re_D = 5000$ a significant Reynolds dependency has been observed by Chen[13]. Current experiments are carried out for the Reynolds number range $46000 < Re_D < 115000$. In this range the static pressure distribution is independent of Reynolds [16].

Figure 5.8 presents the circumferential distribution of mean pressure coefficient C_p at different angles of incidence. At angle 0 (fig. 5.8a), the current experiment agrees well with the data published by Chen[13]. The LES - G simulation gives accurate prediction of the base pressure at downstream side but presents lower pressure on the sides than both experiments (see table 5.1). LES - F shows good agreement with the experiment at zero angle of attack. Also uRANS predicts well the average pressure.

The pressure distribution on the upstream face changes with the rotation of the rod: as α increases, the position of the stagnation point moves from center to the lower corner (3).

In the experiment of Chen[13] the $\alpha_{cr} = 14^\circ$ for $Re_D = 5300$. Our LES was solved at $\alpha = 13^\circ$ at a similar Reynolds number. The mean pressure

predicted by LES - G at $\alpha = 13^\circ$ agrees fairly well with data of Chen. The LES - F agrees well with the experiments with exception of the reattachment wall ($2 < S/D < 3$) (fig. 5.8b). The LES - F at this angle of attack does not provide as high pressure recovery ($C_{p_{max}} - C_{p_{min}}$) on the reattachment wall C. The current experiment showed the critical angle to be $\alpha_{cr} = 13^\circ$ for $46000 < Re_D < 115000$. It seems that the fact that case F has poorer spanwise resolution than case G plays a major role at critical angle of attack α_{cr} .

At the angle $\alpha = 45^\circ$ (fig. 5.8c) there is no detailed Cp data for comparison in the literature. There is a significant difference in the downstream pressure predicted by uRANS and found in experiment. Both LES cases seem to cope with the prediction of average pressure at the rod surface at angle 45 degrees.

Case	α	Mean C_{pb}	Mean Cl	Mean Cd	blockage	Re_D
LES - G	0	-1.54	0.080	2.228	6.0%	5000
	13	-1.24	0.576	1.852	7.0%	5000
	45	-1.87	-0.039	3.088	8.3%	5000
LES - F	0	-1.54	0.080	2.228	6.0%	5000
	13	-1.24	0.576	1.852	7.0%	5000
	45	-1.87	-0.039	3.088	8.3%	5000
uRANS [63]	0	-1.32	0.024		2.0%	140000
	13	-1.50	0.401		2.4%	140000
	45	-1.97	-0.023		2.8%	140000
Current exp. [16]	0	-1.19	0.027	1.925	-	46000-115000
	13	-0.88	0.950	1.439	-	46000-115000
	45	-1.03	0.220	2.145	-	46000-115000
Bearman[9]	0	-1.59			5.5%	22000
Chen[13].	0	-1.44			6.6%	5300
	14	-1.17			8.0%	5300
Knisely[33].	0		0	2.017	2.0%	22000-62000
	13		0.876	1.437	2.4%	22000-62000
	45		-0.023	2.158	2.8%	22000-62000
Norberg[45]	0		0.0	2.197	5%	5000
	13		0.897	1.693	5%	5000
	45		0.01	2.261	5%	5000

Table 5.1: Comparison of mean coefficients, LES not corrected for blockage.

We define blockage as:

$$blockage = A_{wind-tunnel}/A_{rod} \quad (5.4)$$

Where $A_{wind-tunnel}$ is the area of cross-section of the windtunnel at constant

x_1 , and $A_{rod} = L * D * (\sin\alpha + \cos\alpha)$ is the effective area of the rod. While the values of C_p at the front of the rod are quite independent of the blockage effect, the values in the wake depend strongly on blockage effects [9, 58]. We corrected the LES data for blockage effects for all angles of attack using method proposed by Courchesne [14] described in paragraph 3.2.1 in chapter 3. The uncorrected C_p data for LES - F can be found in figure 3.18 (chapter 3).

There is however one very interesting deviation between our measurements and the literature: in the range $25^\circ < \alpha < 45^\circ$ we observe two meta-stable flow modes which we discuss in the next section.

5.4.3 Two wake modes

For angles of attack in the range $0^\circ < \alpha < 25^\circ$ the wake is always unstable and periodic vortex shedding occurs corresponding to whistling. We call this the tonal mode. For angles of attack in the range $25^\circ < \alpha < 45^\circ$ next to the tonal mode a stable silent wake mode is observed. The occurrence of this mode depends on the history of the flow. Pressure coefficient measured for two modes can be seen in figure 5.9 for $Re_D = 46000$ and $Re_D = 92000$. As we can see there is no significant dependence on the Reynolds number. However the difference in C_p between the modes is evident.

In figure 5.10 we show the spectra of the microphone signal at $U_0 = 20m/s$ and $U_0 = 60m/s$. We see that the tonal mode displays a sharp peak close to $St_D = \frac{fD}{U_0} = 0.1$. The silent mode does not show this peak and the broad noise in this case is close to the noise measured in the set-up when the rod has been removed. This is why we call this the silent mode.

For $25^\circ < \alpha < 45^\circ$ the silent mode prevails when the wind-tunnel is started. We can switch the tonal mode on by disturbing the flow upstream of the rod. The tonal mode is then stable. Perturbing the wake of the rod with the hand enables to switch back to the silent mode. Placing a tuft in the flow indicates that the wake is much broader in the silent mode than in the tonal mode.

None of the simulations described in this paper predicted the silent wake mode. It was present at the initial stage of the simulation for 45 degrees angle of attack. After a characteristic time $t^* \approx 56D/U$ the alternate vortex shedding appeared and remained stable.

The current experiment is semi-open, the rod is mounted between two endplates and is not constrained otherwise. Hutcheson [25] did experiments in a similar set-up but did not report the occurrence of a silent mode. Also

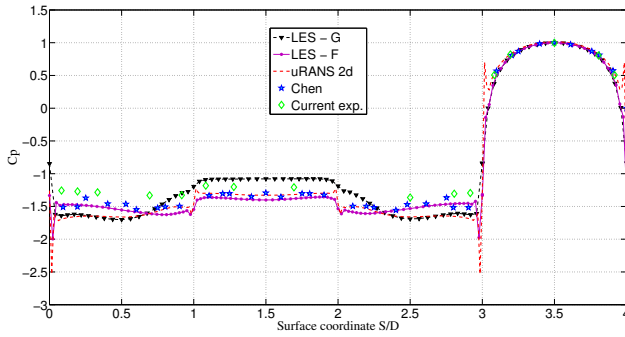
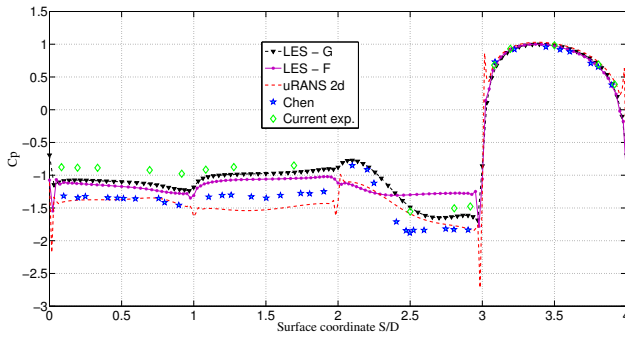
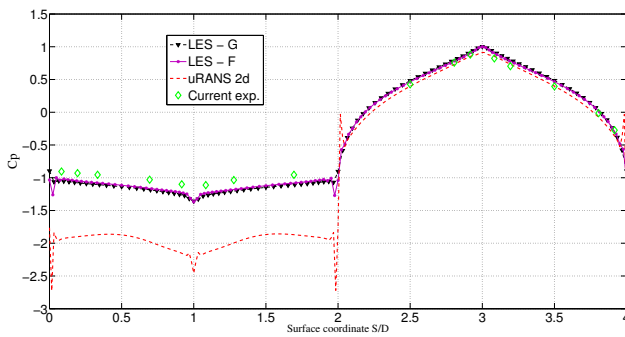
(a) $\alpha = 0^\circ$ (b) $\alpha = \alpha_{CR} = 13^\circ$ (c) $\alpha = 45^\circ$

Figure 5.8: Mean pressure coefficient C_p , tonal mode. Corrected for blockage effect. LES, $Re_D = 5000$, Chen [13], $Re_D = 5300$, Current experiment [16], $Re_D = 46000$.

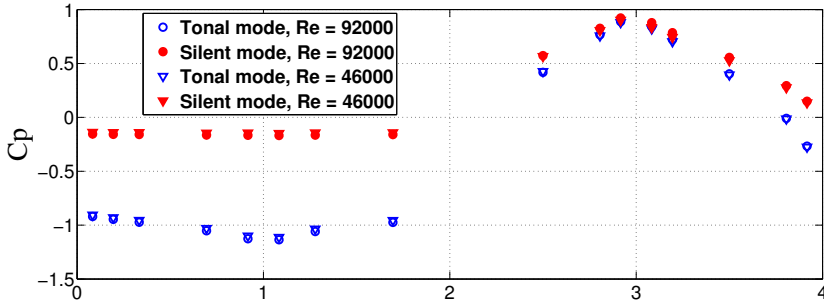


Figure 5.9: C_p at $\alpha = 45^\circ$, tonal and silent mode

NLR measurements in a similar set-up were not able to reproduce our silent mode in an experiment similar to ours[46].

5.4.4 Mean lift and drag

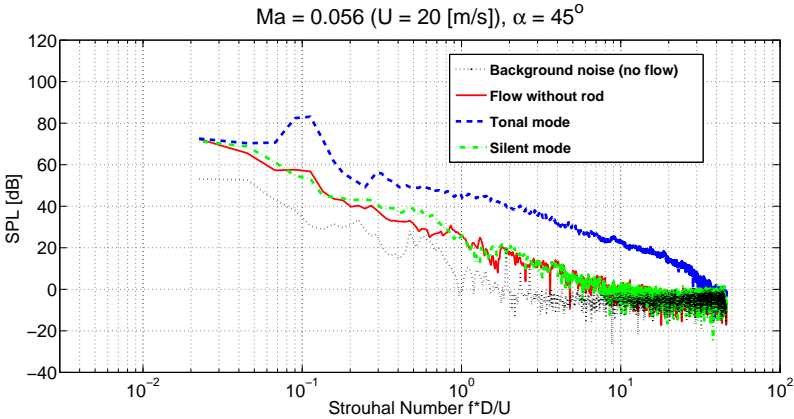
An overview of the results for the lift and drag is provided in table 5.1 for $\alpha = 0^\circ, 13^\circ$ and 45° .

Figures 5.11a and 5.11b present the mean lift and drag as a function of angle of attack calculated from signals of pressure at the rod surface obtained from numerical simulations. For $\alpha = 0^\circ$ there is an excellent agreement between numerical results and literature. As mentioned already while discussing the C_p distribution the reattachment at $\alpha = \alpha_{cr} = 13^\circ$ is not properly captured by our simulation F which results in 50% lower Cl_{mean} at $\alpha = 13^\circ$ (fig. 5.11a).

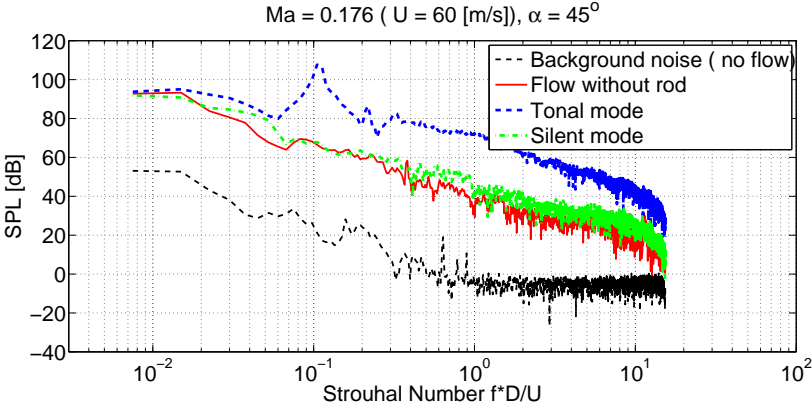
For $\alpha = 45^\circ$ there is a significant difference in the downstream pressure measured by uRANS and experiment which results in C_d (fig. 5.11b) 60% higher than the ones found in the literature[33, 45]. The resolved LES - F agrees well with the current experiment data [16].

5.4.5 Fluctuating part of lift and drag

To calculate the root mean square of the lift and drag as function of time, the mean is removed from the signals for lift or drag obtained from numerical simulation (see figures 5.12 and 5.13). Then it is clipped to contain full periods based on zero crossing. Integration of power spectrum distribution gives the overall rms value for all frequencies resolved in LES.



(a)



(b)

Figure 5.10: Comparison of tonal and silent mode

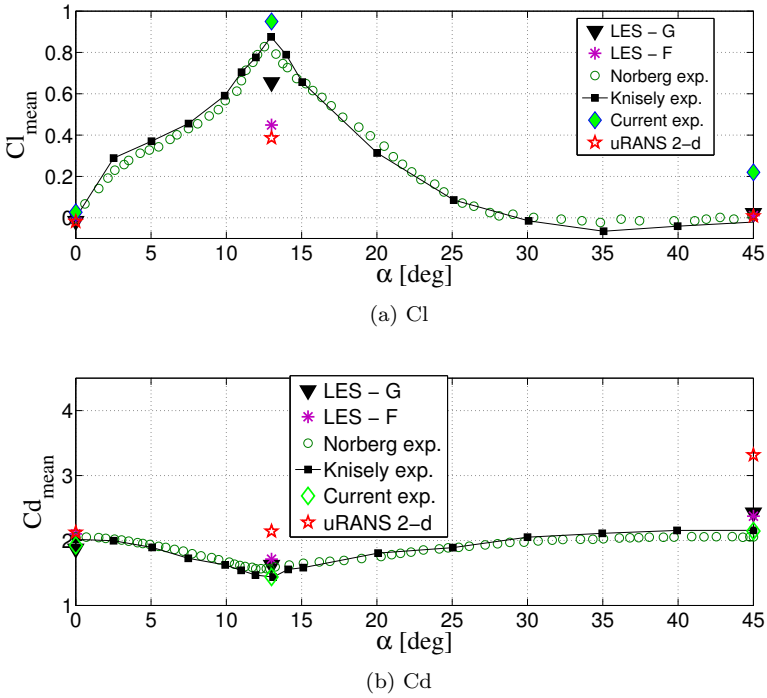
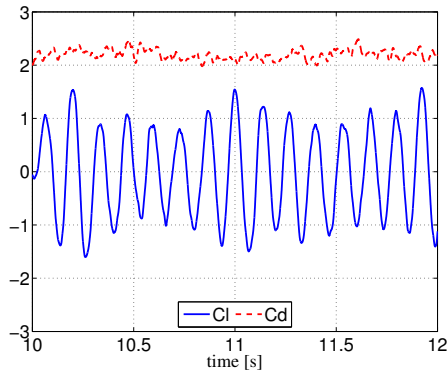
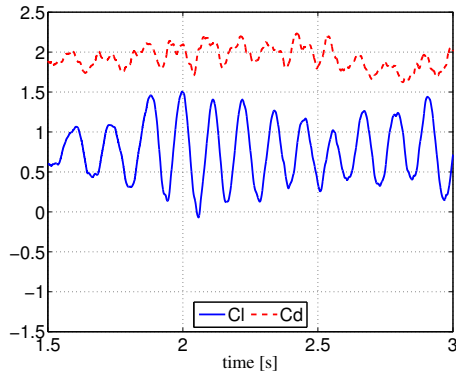


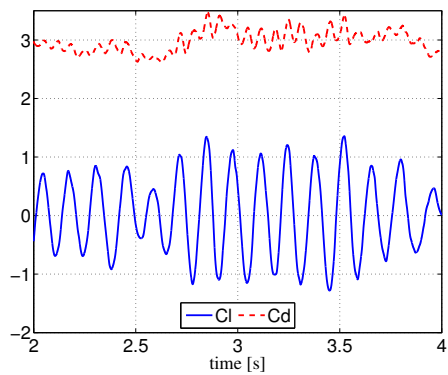
Figure 5.11: Mean lift and drag coefficients. Corrected for blockage effects. LES, $Re_D = 5000$ Norberg [45] $Re_D = 5000$, Knisely [33], $Re_D = 22000$ to 62000, Current experiment [16], $Re_D = 46000$



(a) $\alpha = 0^\circ$

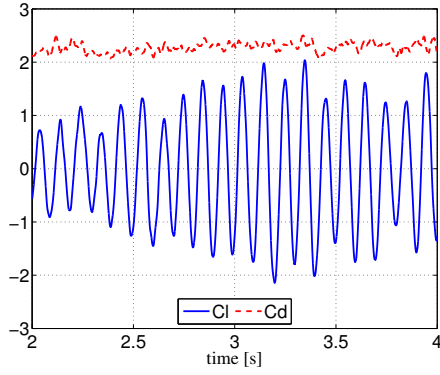


(b) $\alpha = 13^\circ$

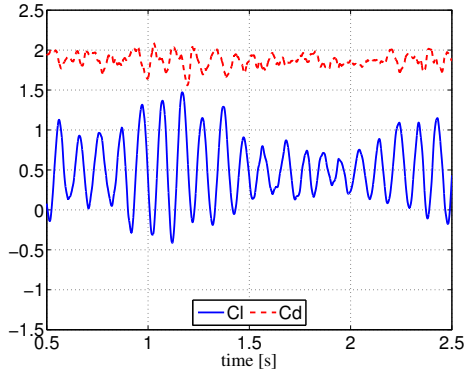


(c) $\alpha = 45^\circ$

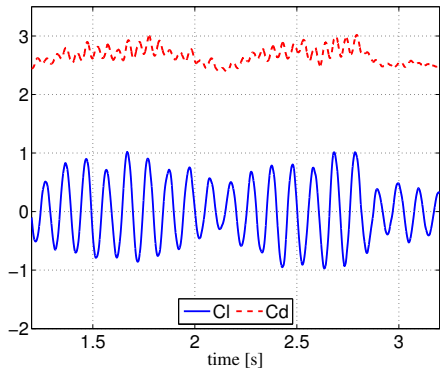
Figure 5.12: Lift and drag signals from LES - G, - - $C_d(t)$, - $Cl(t)$, $Re_D = 5000$



(a) $\alpha = 0^\circ$

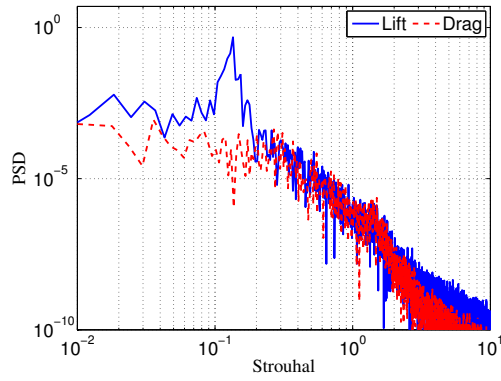
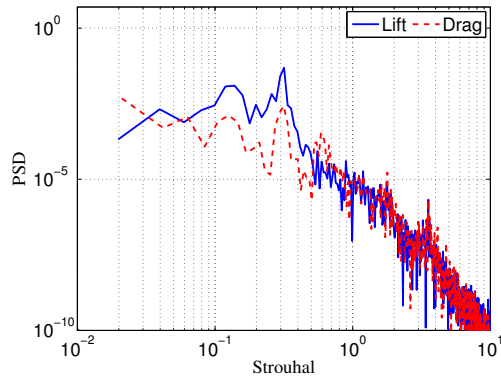
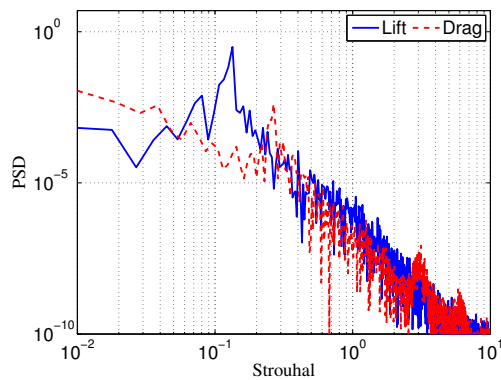


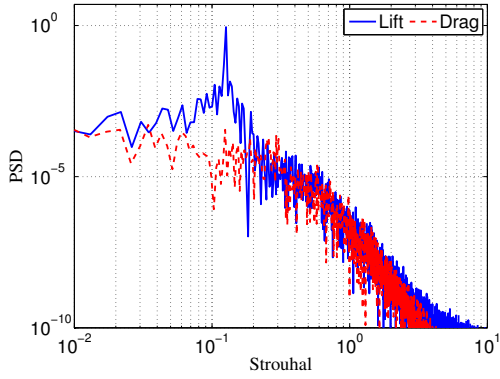
(b) $\alpha = 13^\circ$



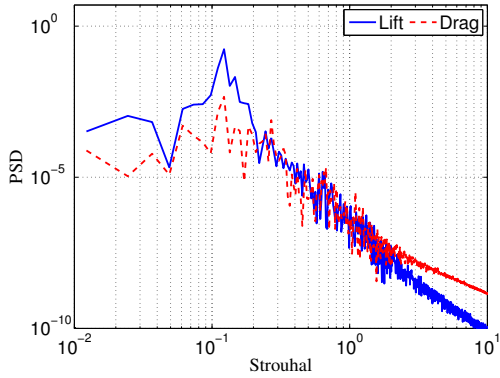
(c) $\alpha = 45^\circ$

Figure 5.13: Lift and drag signals from LES - F, - - $C_d(t)$, $-C_l(t)$, $Re_D = 5000$

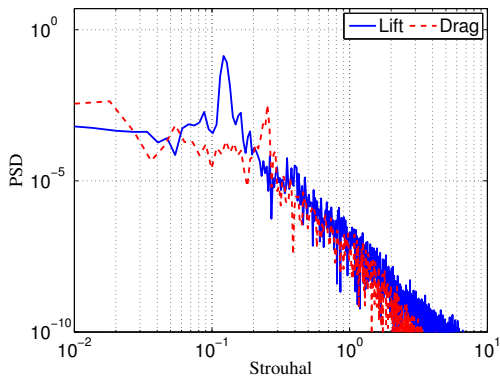
(a) $\alpha = 0^\circ$ (b) $\alpha = 13^\circ$ (c) $\alpha = 45^\circ$ **Figure 5.14:** Lift and drag spectrum from LES - G, $Re_D = 5000$ 107



(a) $\alpha = 0^\circ$



(b) $\alpha = 13^\circ$



(c) $\alpha = 45^\circ$

The LES-predicted lift fluctuations agree well with experimental data of Knisely[33] for all angles of attack investigated (see fig. 5.16a). The uRANS simulation performs especially poor for angle of attack of 13 degrees giving nearly 50% difference with the values measured by Knisely[33] and computed by LES. The overestimation of uRANS lift fluctuation at $\alpha = 45^\circ$ is 40%.

It is important to note that all the data from LES are corrected for blockage using the method of Courchesne [14] which was proposed for a rod at zero angle of attack. We use it for other angles as well. We did not correct the uRANS results because it was solved using a large domain ($b = 1/50$) and far field boundary condition. The corrected and uncorrected values can be seen in table 5.2.

	angle	blockage	Cl_{rms}	Cl_{rms} corrected	correction
LES - G	0	10%	0.9516	0.8263	15%
	13	12%	0.3660	0.3084	18.5%
	45	13.5%	0.6758	0.5509	22.5%
LES - F	0	6%	0.9523	0.8802	8%
	13	7%	0.3991	0.3629	10%
	45	8.3%	0.5286	0.4721	12%

Table 5.2: Cl_{rms} predicted with LES ($Re_D = 5000$) with and without corrections for blockage

The Cl_{rms} of Fujita [21] ($Re_D = 11000$) and the results from our experiment are computed from the tonal sound pressure level results using formula (3.30) explained in chapter 3. We will be looking at tonal noise originated by lift fluctuations at fundamental frequency. In figure 5.17 we compare the value of spectral peak of lift coefficient Cl (integrated in region $St_D(peak) \pm 0.02$) and its full spectrum integration which is the root mean square by definition. For numerical simulations the value of spectral peak is 40% to 50% lower than the full spectrum rms at $\alpha = 0^\circ$ and $\alpha = 45^\circ$, meaning 2-3dB lower sound pressure level. The situation is different for LES - G at $\alpha = 13^\circ$. The time-series of numerical simulations is relatively short in comparison with the experiment. The short time-series obtained in LES - G at $\alpha = 13^\circ$ (figure 5.12b) results in 80% difference which would result in 7dB difference in sound pressure level. Knisely [33] reports quite good agreement between peak and full spectrum rms for angles higher than 7°

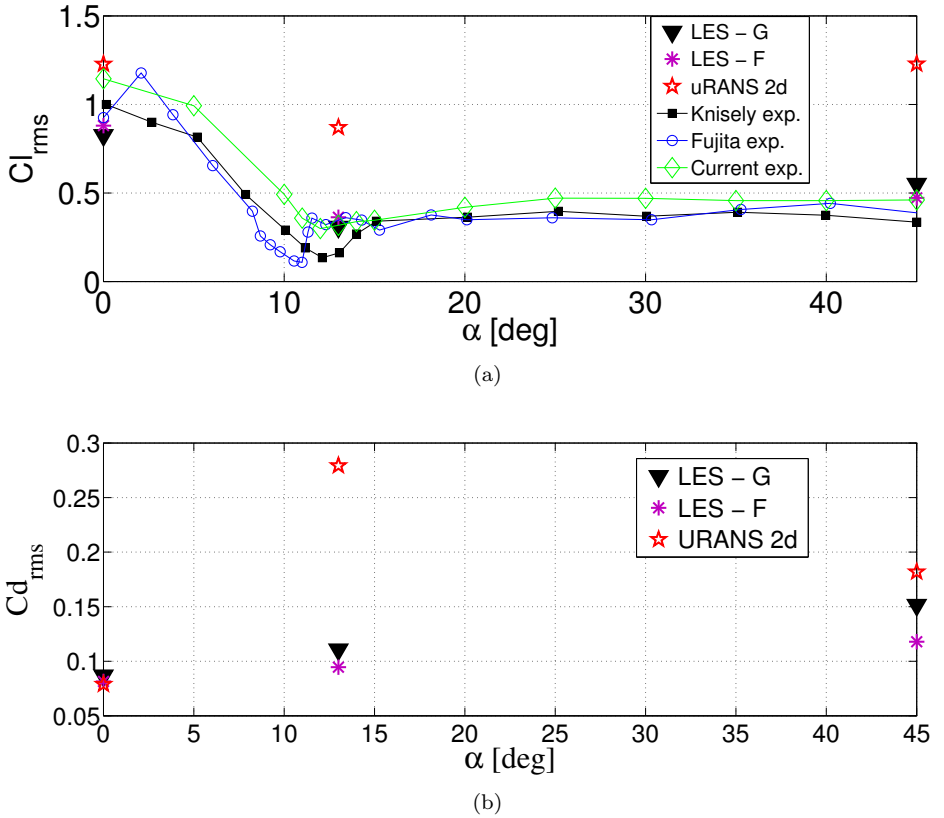


Figure 5.16: RMS of lift and drag vs. angle of attack. Corrected for blockage effects. LES, $Re_D = 5000$, uRANS [63], $Re_D = 144000$, Knisely [33], $Re_D = 22000$ to 62000 , Fujita [21], $Re_D = 10000$, Current experiment [16], $Re_D = 46000$.

(especially around critical angle α_{cr} this agreement is best). However at zero angle of attack Knisely reports the difference of 30% between the peak and full rms value.

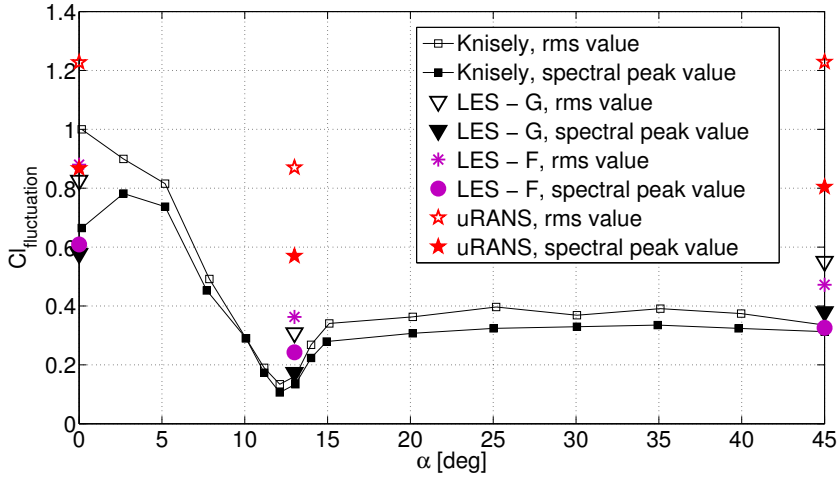


Figure 5.17: Comparison of Cl_{rms} and spectral peak value. Knisely [33] ($Re_D = 22000$), uRANS [63] ($Re_D = 144000$)

It is difficult to find literature data about drag fluctuations as a function of the angle of attack α . In principle in our acoustic experiment we could obtain for $\alpha = 0^\circ$ and $\alpha = 45^\circ$ the drag because due to symmetry the even harmonics of the fluctuating lift vanish and the drag oscillates with $2f$.

Unfortunately the acoustic reflection by the settling chamber is significant for the drag so that there is a large uncertainty in these results and we will not discuss them in detail.

The Strouhal number is based on the mean inflow velocity U_0 and rod width D . The influence of the angle of attack on the Strouhal number of vortex shedding (coincident with lift frequency) can be seen in figure 5.18. One can see a maximum around $\alpha = 13^\circ$ in all available data. The paper of Chen[13] indicates that the variation of the angle of attack corresponding to the maximum Strouhal number with the Reynolds number is important below $Re = 5000$. At $Re=5300$ he states that $\alpha_{cr} = 14^\circ$. Below $\alpha = 25^\circ$, our experiment agrees well with the one of Fujita[21]. However for the angles $25^\circ < \alpha < 45^\circ$ it is progressively lower than other literature data being 17%

α	LES - G	LES - F	uRANS	Current exp.	Literature
$St_D(C_l)$					
0	0.133	0.125	0.135	0.115	0.12 - 0.13
13	0.144	0.126	0.148	0.143	0.14 - 0.155
45	0.133	0.121	0.127	0.106	0.120 - 0.125
$St_D(C_d)$					
0	0.036	0.007	0.263	-	-
13	0.155	0.129	0.156	-	-
45	0.267	0.253	0.255	-	-

Table 5.3: Strouhal number $St_D = \frac{fD}{U_0}$ of C_l and C_d as a function of α , $Re_D = 5000$, uRANS [63], current experiment [16], literature [21, 33, 45]

lower than Fujita's at $\alpha = 45^\circ$. Table 5.3 shows also the Strouhal numbers of oscillation of drag force calculated by LES. We see that case F gives 20% lower Strouhal number at $\alpha = 13^\circ$. It is difficult to define the dominating frequency of C_d at 0° angle of attack (see also figure 5.15a) - it is not the expected double of vortex shedding frequency f . Interestingly at $\alpha = 13^\circ$ the oscillations in $C_d(t)$ are determined by the fundamental oscillation frequency close to $St_D(f)$ controlling the oscillations in $C_l(t)$ (see table 5.3 and figure 5.15b). This is in contrast with oscillation of the drag at $\alpha = 45^\circ$ which is dominated by the second harmonic $2f$ of the lift oscillation frequency.

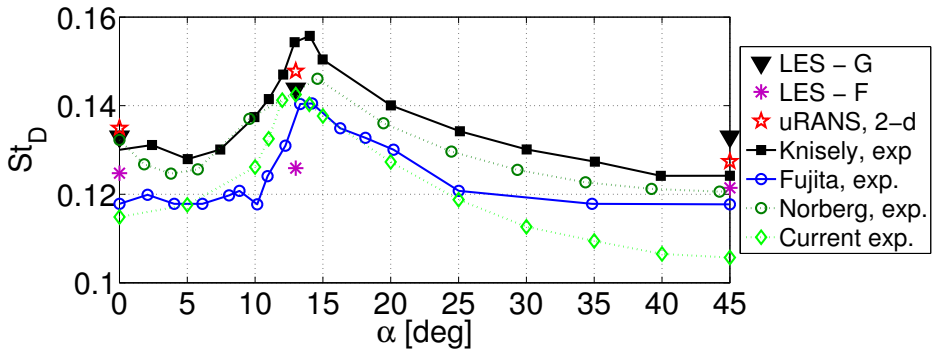


Figure 5.18: Strouhal numbers at different angles of attack for the lift force oscillation. uRANS [63] $Re_D = 144000$, Norberg [45], $Re_D = 5000$, Knisely [33], $Re_D = 22000$ to 62000 , Fujita [21], $Re_D = 10000$, Current experiment [16], $Re_D = 46000$

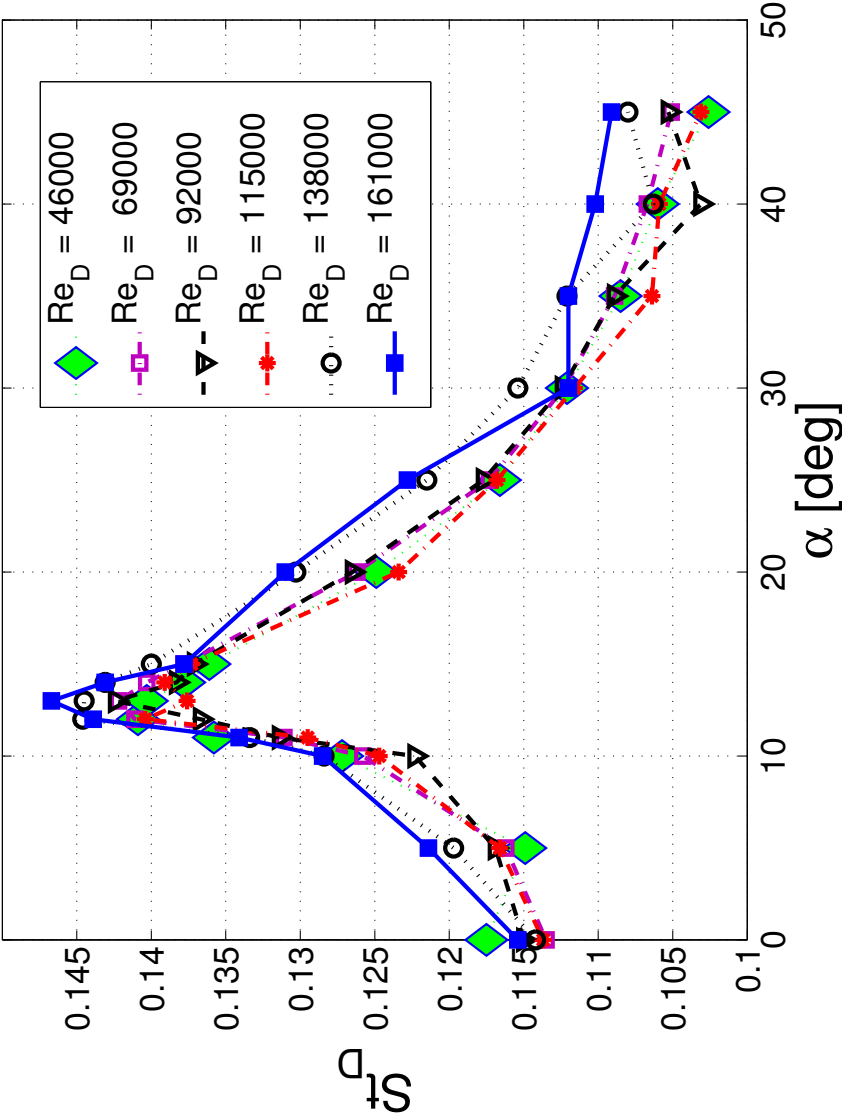


Figure 5.19: Strouhal numbers at different angles of attack for the lift force oscillation at different Reynolds numbers. Current experiment [16]

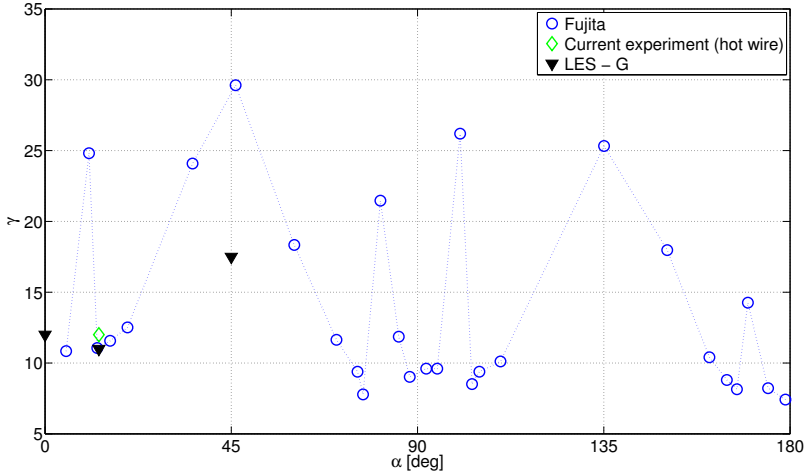


Figure 5.20: Coherent length coefficient γ vs. angle of attack α . Measured by Fujita [21] by means of wall pressure and our experiment based on a hot wire measurement.

Following Fujita[21] the lift fluctuations are coherent along the rod. The magnitude square coherence of velocities $v_1(t)$ and $v_2(t)$ at two points along the rod can be calculated using formula:

$$|C_k(f)|^2 = \frac{|S_{v_1 v_2}(f)|^2}{S_{v_1 v_1}(f) S_{v_2 v_2}(f)} \quad (5.5)$$

where $S_{v_1 v_2}$, $S_{v_1 v_1}$ and $S_{v_2 v_2}$ are cross- and auto-spectra of velocity. The peak value of $|C_k(f)|$ as a function of spanwise separation can be fitted with gaussian distribution. The value of parameter γ is determined as a width of the gaussian curve (at level 0.5) divided by the rod diameter. Our measurement at 13° confirms the coherent parameter γ measured by Fujita[21] (see figure 5.20). From the data of Fujita we conclude that:

$$\gamma = \begin{cases} 10 & \alpha = 0^\circ \\ 11 & \alpha = 13^\circ \\ 30 & \alpha = 45^\circ \end{cases}$$

The spanwise coherence of LES case G (seen also in figure 5.20) is comparable with Fujita [21] and current experiment at angles 0° and 13° , however

it is significantly lower than in the experiments of Fujita at $\alpha = 45^\circ$.

5.5 Sound propagation - theory

The sound production by a flow as observed by a listener immersed in uniform stagnant fluid with speed of sound c_0 , density ρ_0 and pressure p_0 , has been derived by Lighthill[37]. Lighthill starts from the exact mass and momentum equations written for convenience in the index notation:

$$\frac{\partial \rho}{\partial t} + \frac{\partial \rho v_i}{\partial x_i} = 0 \quad (5.6)$$

and

$$\frac{\partial \rho v_i}{\partial t} + \frac{\partial \rho v_i v_j}{\partial x_j} = -\frac{\partial p}{\partial x_i} + \frac{\partial \tau_{ij}}{\partial x_j} + f_i \quad (5.7)$$

where v_i is the flow velocity, τ_{ij} the viscous stress tensor and f_i the force density of an external field acting on the fluid. Repetition of an index implies summation following the convention of Einstein as in the divergence $\frac{\partial v_i}{\partial x_i} = \nabla \cdot \vec{v}$.

Taking the time derivative of the mass conservation law 5.6 and subtracting the divergence of the momentum equation 5.7 we obtain:

$$\frac{\partial^2 \rho}{\partial t^2} = \frac{\partial^2 (\rho v_i v_j - \tau_{ij})}{\partial x_i \partial x_j} + \frac{\partial^2 p}{\partial x_i^2} - \frac{\partial f_i}{\partial x_i} \quad (5.8)$$

A wave equation is obtained by subtracting from both sides of this equation the term $c_0^2 \frac{\partial^2 \rho}{\partial x_i^2}$ and introducing the perturbation in pressure $p' = p - p_0$ and density $\rho' = \rho - \rho_0$:

$$\frac{\partial^2 \rho'}{\partial t^2} - c_0^2 \frac{\partial^2 \rho'}{\partial x_i^2} = \frac{\partial^2 (\rho v_i v_j - \tau_{ij})}{\partial x_i \partial x_j} + \frac{\partial^2 (p' - c_0^2 \rho')}{\partial x_i^2} - \frac{\partial f_i}{\partial x_i} \quad (5.9)$$

With this choice of reference state the equation of Lighthill describes the acoustic wave propagation around the listener if the right hand side of the equation can be neglected, which is reasonable for the flow conditions considered. Because we consider low Mach number flows at high Reynolds numbers, the sound production by the rod is dominated by the reaction force of the rod to the force of the flow on the rod. Typically the sound pressure due to this force scales at M^3 while the other terms (due to the fluctuation in Reynolds stresses) scale as M^4 . We will use the force field f_i

to represent this reaction force. As we are focusing on the whistling due to periodic vortex shedding we have $St_D \leq 0.14$ and $M \leq 0.2$, hence the rod width D is small compared to the acoustic wave length $c_0/f = D/(MSt_D)$. Neglecting the variation of emission time in a cross section of the rod, we can lump the force field into a line force along the rod axis, represented by a line force density σ_i :

$$f_i(x, t) = \sigma_i(x_3, t)\delta(x_1)\delta(x_2). \quad (5.10)$$

where $\delta(x_i)$ is the Dirac delta function. Neglecting the effect of flow on the wave propagation, the formal solution of the wave equation for free field conditions is given by Dowling[17]:

$$p'(\vec{x}, t) = c_0^2 \rho'(\vec{x}, t) = -\frac{1}{4\pi} \frac{\partial}{\partial x_i} \iiint_V \frac{f_i(\vec{y}, t_e)}{|\vec{x} - \vec{y}|} dy_1 dy_2 dy_3 \quad (5.11)$$

where the retarded time is defined by:

$$t_e = t - \frac{|\vec{x} - \vec{y}|}{c_0} \quad (5.12)$$

and we use the assumption that at the position of the listener \vec{x} the acoustical approximation $p'(\vec{x}, t) = c_0^2 \rho'(\vec{x}, t)$ is valid. In terms of the line force density (5.10) we find:

$$p'(\vec{x}, t) = c_0^2 \rho'(\vec{x}, t) = -\frac{1}{4\pi} \frac{\partial}{\partial x_i} \int_{-L_{eff}/2}^{L_{eff}/2} \frac{\sigma_i(y_3, t_e)}{|\vec{x} - \vec{y}|} dy_3 \quad (5.13)$$

The integration in equation (5.13) extends from $-L_{eff}/2$ to $L_{eff}/2$. L_{eff} is so called effective rod length. It allows to take into account the reflection of the acoustic waves at the side plates supporting the rod and the spanwise correlation.

Neglecting diffraction effects at the edges of the plate we find L^* , which is an effective length allowing to account for reflections from the endplates, using the method of images (figure 5.22):

$$L^* = L + \frac{RL}{r - R} \quad (5.14)$$

where $r = \sqrt{x_1^2 + x_2^2} = 0.59m$ is the distance from the rod to the microphone and $R = 0.175m$ is the radius of the plates (figure 5.22).

Following the measurements of Fujita[21] the vortex shedding is coherent along the rod (see previous section). The effective length of the rod taking

into account the images and coherence can be expressed following Fujita [21] as:

$$L_{eff} = \sqrt{L_\gamma L^*} \quad (5.15)$$

We assume $L_\gamma = \gamma D$ if $\gamma D \leq L^*$ otherwise we assume $L_\gamma = L^*$. The line force density is only a function of the retarded time. For harmonic oscillations in the complex notation we have:

$$\sigma_2(\vec{x}, t) = \frac{1}{2} \rho_0 U^2 \sqrt{2} |Cl_{rms}| D e^{i\omega t} \quad (5.16)$$

where $\sqrt{2} Cl_{rms}$ is the amplitude of the lift fluctuations (figure 5.16a). Substitution into equation 5.13 yields:

$$p'(\vec{x}, t) = \frac{\rho_0 U^2 \sqrt{2} |Cl_{rms}| D}{8\pi} \frac{i\omega}{c_0} e^{i\omega t} \int_{-L_{eff}/2}^{L_{eff}/2} \left(1 + \frac{c_0}{i\omega |\vec{x} - \vec{y}|}\right) \frac{x_2}{|\vec{x} - \vec{y}|^2} e^{-i\frac{\omega}{c_0} |\vec{x} - \vec{y}|} dy_3 \quad (5.17)$$

where $|\vec{x} - \vec{y}| = \sqrt{x_1^2 + x_2^2 + (x_3 - y_3)^2}$.

We find the formula for the amplitude of sound pressure generated by $2N + 1$ point forces distributed along the rod axis:

$$p'(\vec{x}, t) = \frac{\sqrt{2} \rho_0 U^2 |Cl_{rms}| D}{8\pi} \frac{i\omega}{c_0} \sum_{n=-N}^N \left(1 + \frac{c_0}{i\omega r_n}\right) \frac{x_2}{r_n^2} e^{-i\frac{\omega r_n}{c_0}} \Delta y_3 \quad (5.18)$$

where

$$\Delta y_3 = \frac{L_{eff}}{2N + 1} \quad (5.19)$$

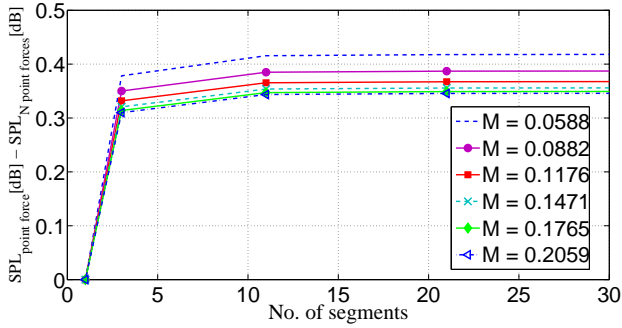
and using $x_3 = 0$:

$$r_n = \sqrt{x_1^2 + x_2^2 + (n \Delta y_3)^2} \quad (5.20)$$

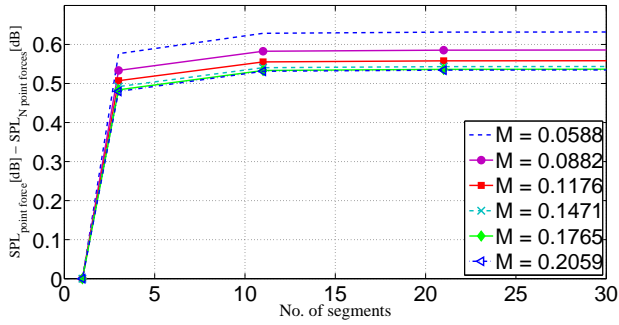
Then

$$p'_{rms} = \frac{|p'(\vec{x}, t)|}{\sqrt{2}} \quad (5.21)$$

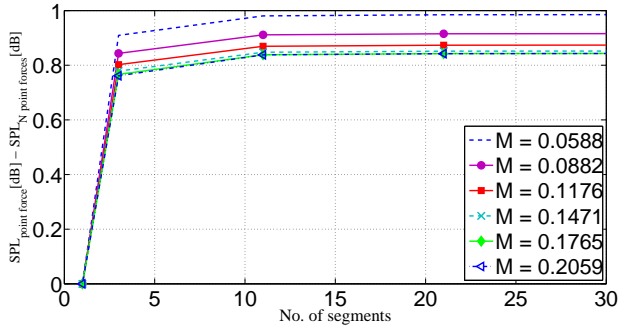
In figure 5.21 we find the difference of SPL computed for one point force ($SPL_{pointforce}$, $N = 0$) and n equal forces distributed along the rod axis ($SPL_{npointforces}$, $n = 2N + 1$). Lumping the oscillating force into one point leads to overestimation of SPL. It is enough to divide the point force into $n > 11$ equally spaced forces to obtain a result of converged numerical integral of equation (5.17).



(a) $\alpha = 0^\circ$



(b) $\alpha = 13^\circ$



(c) $\alpha = 45^\circ$

Figure 5.21: Convergence of numerical integration with increasing number of segments along the axis of the rod.

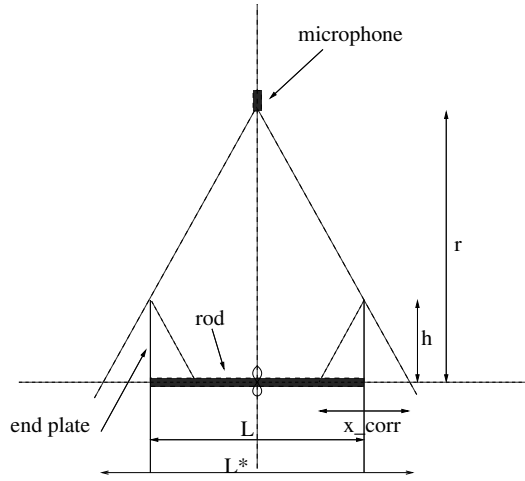


Figure 5.22: Determination of the corrected length of the rod L^* due to reflections of waves on the side plates. We use geometrical acoustics.

5.6 Sound pressure level

Figure 5.23 shows the angle of attack dependency of the SPL generated at all Mach numbers measured in our experiment. As expected it follows the same trend as the lift fluctuations (figure 5.16) and Strouhal number (figure 5.18). It can be scaled with $M^6(1 + (\frac{D}{2\pi r St M})^2)$ taking into account near and far field influence. All the scaled curves collapse within 1-2 dB accuracy for all angles of attack (figure 5.24).

The current experiments and the ones found in the literature were performed in different set-ups, at different velocities and the sound was registered at different position of the microphone \vec{x} . In order to compare the data we use the scaling to account for these differences:

$$SPL_{scaled} = SPL - 10 \log_{10} \left(\frac{num}{den} \right) \quad (5.22)$$

$$num = \frac{M^6 St^2 y^2 L_{eff}^2}{r^4} \left(1 + \left(\frac{D}{2\pi r St M} \right)^2 \right) \quad (5.23)$$

$$den = \frac{M_{Fujita}^6 St_{Fujita}^2 y_{Fujita}^2 L_{Fujita}^2}{r_{Fujita}^4} \left(1 + \left(\frac{D_{Fujita}}{2\pi r_{Fujita} St_{Fujita} M_{Fujita}} \right)^2 \right) \quad (5.24)$$

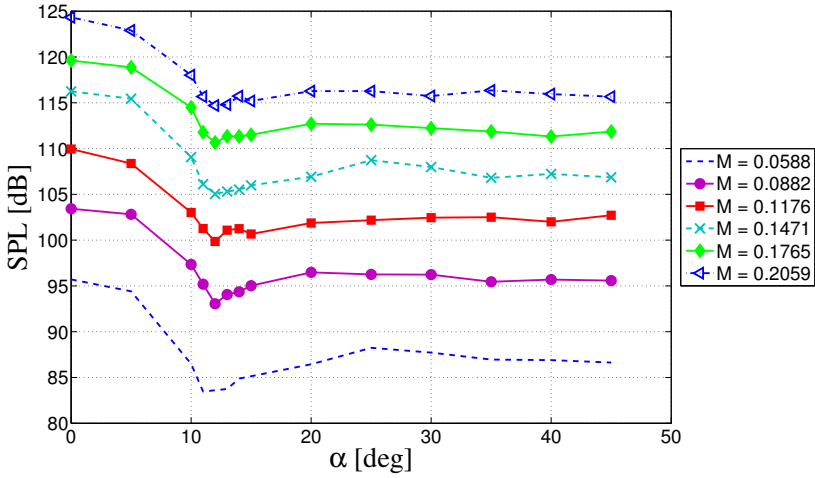


Figure 5.23: SPL vs. angle of attack - experiment [16]

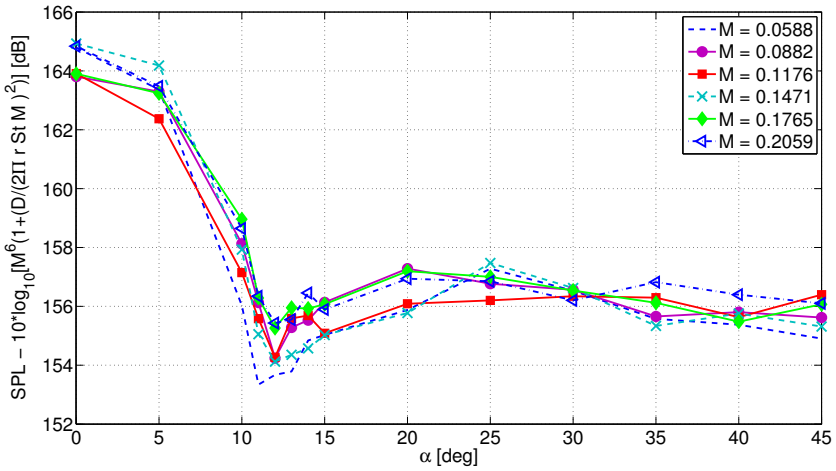


Figure 5.24: SPL vs. angle of attack - experiment [16] scaled with $M^6(1 + \frac{D}{2\pi r St M})^2$

In figure 5.25 we scale all the data with reference to the SPL of Fujita [21] using a formula (5.22). For this scaling we assumed that the experiments of Fujita [20] were performed at $M = 0.0235$ ($Re_D = 10000$) using rod of $D = 0.02m$ and $L = 0.2m$. The position of the microphone is $\vec{x}_f = (0, 1m, 0)$.

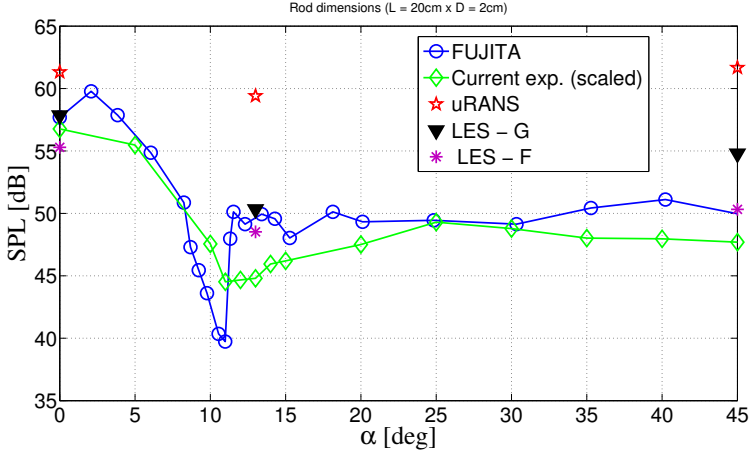


Figure 5.25: SPL vs. angle of attack - comparison with literature. Numerical results based on Cl_{rms} (by integration of the full spectrum). Fujita [21], Current exp. [16], uRANS [63]. All plots scaled to $Re_D = 10000$

We compare the resulting theoretical SPL based on the formula (5.18) (Cl_{rms} obtained by integrating respective full spectra seen in figure 5.16) with the measured sound level (also full spectra). We take into account L_{eff} defined in (5.15). The SPL generated by one oscillating point force placed in $\vec{y} = (0, 0, 0)$ is higher than the one computed by numerical integration in $2N + 1$ equal segments (details in figure 5.21). Figure 5.26 shows the theoretical value computed on $2N + 1 = 13$ segments. One can see the deviation between the measured sound pressure level and the theory at different angles of attack versus Mach number for LES G, LES F and uRANS. This is also summarised in tables 5.4 5.5 and 5.6 adding also the SPL computed using Cl_{rms} and St_D obtained in all numerical simulations described in this thesis. At zero angle of attack, the worse prediction of the tonal sound is obtained using the case with narrow domain and wall functions - case C. The best result is given by a periodic case F1. At critical angle of attack $\alpha_{cr} = 13^\circ$ we observe that uRANS and cases with narrow domain (A and B) overpredict the tonal sound by 9 and 5 dB respectively. Cases F and G

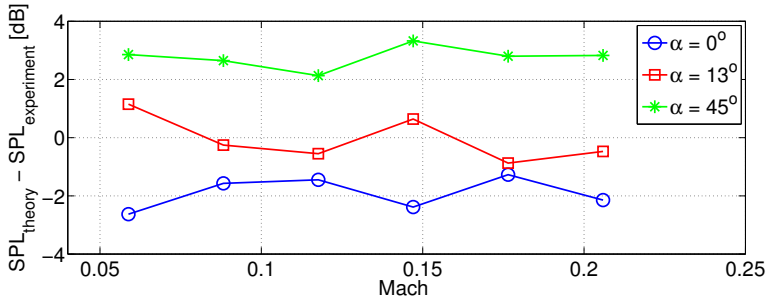
described in this chapter provide the sound prediction within 1dB difference from the measured one. At angle of attack $\alpha = 45^\circ$ the importance of spanwise dimension of the domain is even more crucial. uRANS overpredicts the SPL by 10dB. Considering the narrow domain LES cases A and B, we see also that the effect of under-resolving the boundary layer is important at this angle of attack. Best results are achieved using a wide domain (case F and G described in this chapter) with wall-resolved case F agreeing with measurements within 1dB.

	y_{min}^+	L/D	blockage	SPL_{diff} (full spectrum)	Notes
Section 3.3					
LES - A	1.5	3	10%	3.0dB	resolved BL
LES - B	7	3	6%	2.5dB	unresolved BL
LES - C	60	3	10%	-4.5dB	wall functions
Section 3.4					
uRANS	1.5	0(2d)	2%	2.0dB	two-dimensional
LES - D	1.5	1	6%	2.0dB	spanwise periodic
LES - E	1.5	8.5	6%	1.5dB	spanwise periodic
LES - F1	1.5	17	6%	-0.5dB	spanwise periodic
Section 3.5					
LES - F	1.5	17	6%	-2dB	end-plates
Section 4.1					
LES - G	12	12	10%	-2.5dB	unresolved BL

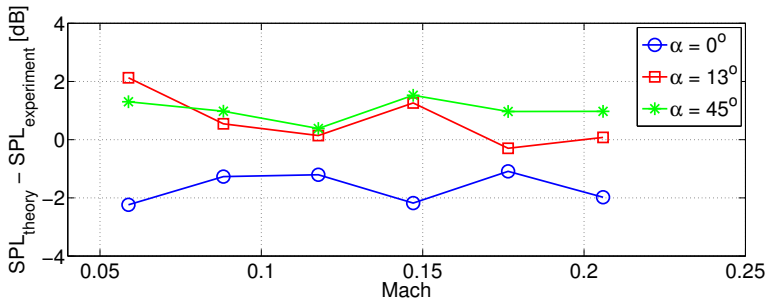
Table 5.4: Summary of SPL predicted by numerical simulations described in this thesis for $\alpha = 0^\circ$

	y_{min}^+	L/D	blockage	SPL_{diff} (full spectrum)	Notes
Section 3.3					
LES - A	1.5	3	10%	5.0dB	resolved BL
LES - B	7	3	6%	5.0dB	unresolved BL
Section 3.4					
uRANS	1.5	0(2d)	2%	9.0dB	two-dimensional
Section 3.5					
LES - F	1.5	17	6%	0.5dB	end-plates
Section 4.1					
LES - G	12	12	10%	-0.5dB	unresolved BL

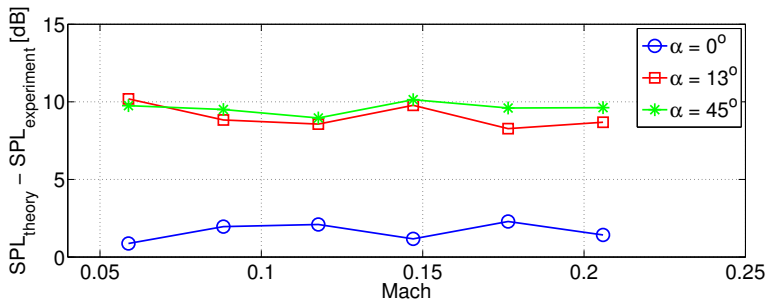
Table 5.5: Summary of SPL predicted by numerical simulations described in this thesis for $\alpha = 13^\circ$



(a) LES - G(coarse)



(b) LES - F(fine)



(c) uRANS

Figure 5.26: SPL difference between current experiment [16] and theory vs. Mach number. Theoretical level based on Cl_{rms} (full spectrum)

	y_{min}^+	L/D	blockage	SPL_{diff} (full spectrum)	Notes
Section 3.3					
LES - A	1.5	3	10%	5.0dB	resolved BL
LES - B	7	3	6%	9.5dB	unresolved BL
Section 3.4					
uRANS	1.5	0(2d)	2%	10.0dB	two-dimensional
Section 3.5					
LES - F	1.5	17	6%	1dB	end-plates
Section 4.1					
LES - G	12	12	10%	3dB	unresolved BL

Table 5.6: Summary of SPL predicted by numerical simulations described in this thesis for $\alpha = 45^\circ$

5.7 Conclusion

Using incompressible LES at Reynolds 5000 over a rod length 12D and 17D with no-slip end-plates boundary conditions we predicted the static pressure distribution on the rod, the fluctuating lift and drag forces and the Strouhal number for periodic vortex shedding.

5.7.1 Flow prediction

At zero angle of attack, $\alpha = 0^\circ$, the prediction agrees within the accuracy of the data presented with the literature. The Reynolds number dependency is marginal for $Re_D > 5000$.

At $\alpha = 13^\circ$ the flow is difficult to simulate because we are close to the critical angle α_{cr} at which reattachment of the flow occurs on the lower face of the rod. Yet the mean flow prediction is in fair agreement with the data from literature. For example the predicted Cl_{mean} is 20% (case F) lower than reported literature data at $Re_D = 5000$. We suspect the numerical method to be unable to describe accurately reattachment or practical differences such as the effect of inflow turbulence level.

At $\alpha = 45^\circ$ we observe spectacular difference between our experimental results, literature and numerical results. Firstly the experiments display two meta-stable flow modes: a silent mode and a tonal mode. Both can appear depending on the flow history in the range $25^\circ < \alpha < 45^\circ$. In literature there is no mention of a silent mode and the numerical results did not reproduce it.

Also for the tonal mode our experiments show significantly lower Strouhal

number in the range $25^\circ < \alpha < 45^\circ$ than data reported in the literature. The numerical model prediction is close to literature data. The Cd_{mean} and Cl_{rms} are overestimated by the uRANS numerical model.

5.7.2 Tonal noise

For 0° and 13° the predicted SPL based on LES flow calculations agrees within 2dB with our experiments. After corrections for scaling our experimental data agree well with results from literature (Fujita [21] and Hutcheson[25]) except for the strong dip of $-10dB$ displayed by Fujita's results around α_{cr} . This difference might be due to Reynolds number dependency.

At zero degree uRANS predicts SPL within 2dB. For 13° and 45° the SPL predicted using uRANS is $10dB$ higher than experimental results.

5.7.3 General conclusion

Except for the necessary correction for blockage the incompressible LES calculations provide a fair predictions of both mean flow and tonal noise production of a square rod.

The significant deviations between our experiment and literature for $25^\circ < \alpha < 45^\circ$ such as the appearance of a silent flow mode is not yet understood and deserves further study.

Chapter 6

Concluding remarks

The goal of this work was to provide some general guidelines for an industrial simulation predicting tonal sound generated by a bluff body in cross flow.

A review of literature concerning the flow around a square rod in cross flow has been provided (Chapter 2). Depending on the angle of attack α , between the main flow direction and the bottom wall of the rod, three types of flows have been identified. For $0^\circ \leq \alpha < \alpha_{cr}$ the flow separates at both front edges of the rod resulting into periodic vortex shedding along the bottom and the top walls. These vortices form in the wake a von Kàrmàn vortex street. For $\alpha_{cr} \leq \alpha \leq 45^\circ$ the flow reattaches at the bottom side wall, so that the wake is dominated by vortex shedding from the upper front edge and from the lower downstream edge. At $\alpha = 45^\circ$ the front stagnation point is at the front edge. Literature reports separation from the bottom and top side edges. This results into periodic vortex shedding forming a von Kàrmàn vortex street in the wake. For low flow speeds ($Re_D < 5000$) the critical angle of attack α_{cr} depends weakly on the Reynolds number. It also depends on the upstream turbulence level and on the sharpness of the edges. Rounded edges result into a lower critical angle than sharp edges. We focus here on the higher Reynolds numbers ($Re_D > 5000$), sharp edges and a low-turbulence, laminar incoming flow, corresponding to $\alpha_{cr} = 13^\circ$.

Dynamic wall pressure measurements by Fujita [21] indicate that the periodic vortex shedding is coherent over at least ten rod widths D . Furthermore Fujita [21] observes a sudden decrease of the radiated sound pressure level (SPL) by 10 dB around α_{cr} . Using the measured wall pressure fluctuations in combination with Curle's analogy [15], Fujita [21] predicts the radiated sound pressure level within 3 dB.

In chapter 3 we provided a study of the influence of various numerical parameters on the LES predictions of the flow and fluctuating forces. It appears that an accurate prediction of the drag and fluctuating lift can only be obtained by simulation of the flow over the entire rod length. Quasi two-dimensional numerical simulations of three rod widths with periodic lateral boundary conditions gave disappointing results. In Fluent it is sufficient to

use a size of the first cell in the boundary layer of $y_{min}^+ < 11$. However, the use of a law of the wall, which is automatically activated for larger y^+ , does not provide accurate results. The spanwise dimension of the computational domain should be at least of the order of the spanwise coherent length. The presence of side-walls supporting the rod appears to have a significant impact on the results especially at higher velocities, when the rod is not acoustically compact. Based on these results it was decided to carry on with an LES of the full rod with side walls. As a consequence only a limited number of simulations could be carried out with at most forty vortex shedding periods in the wall-resolving cases.

An extensive parametric study is not possible with the available computing power. We limited our calculations to $Re_D = 5000$ and three angles of attack ($\alpha = 0^\circ, 13^\circ, 45^\circ$) corresponding to three extreme flow types. We compare the LES and uRANS results in chapter 4 with the detailed PIV flow measurements of Roosenboom [52] at TUDelft for $\alpha = 0^\circ, 12.5^\circ$ and 45° . We consider time-averaged flow patterns, fluctuations and instantaneous flow patterns. LES provides good quantitative information, while uRANS results are rather poor. In chapter 5 the same LES and uRANS results are compared to the steady wall pressure data and acoustic radiation measured by Dorneanu [16] at UTwente. These pressure data agree globally well with the available literature data. However, there is a spectacular difference for the results in the range $25^\circ \leq \alpha \leq 45^\circ$. In contrast to the literature we observe two metastable wake modes, which can be reached depending on the history of the flow. Upon start of the wind tunnel the wake is in its silent mode; there is no periodic vortex shedding. Perturbation of the incoming flow in front of the rod triggers periodic vortex shedding. This whistling mode can be stopped by perturbing the wake within a few diameters of the rod. The silent mode prevails then. This silent mode is most stable for $\alpha = 45^\circ$. However it does not appear spontaneously in our LES. The LES results do predict reasonably well wall pressure and radiated sound pressure levels in the whistling mode at all angles of attack. A simplified model considering the sound source as a set of point forces (in phase) allows a prediction within 2 dB difference from the experiment. It is interesting to notice that uRANS at zero angle of attack gives similar accuracy of tonal sound prediction. It is much more efficient than LES, but does not perform well at higher angles of attack.

From these results we conclude that tonal noise from bluff bodies such as a square rod at low Mach number can be predicted fairly accurately by means of the proposed hybrid procedure: resolved incompressible LES simulation of the full-span geometry combined with Curle's analogy. This

has been accomplished with a commercial LES code as commonly available in industry. Such calculations are, however, still quite demanding in terms of required computational power, so that a parametric study is still very expensive. Furthermore the complex non-linear flow behaviour can involve different wake modes, which are not easily detected by means of numerical simulations. It is therefore essential to combine the numerical simulation with physical experiments. The advantage of numerical simulation is that it does provide access to extremely detailed flow information, which cannot be obtained experimentally. A further study should now assess the potential of this approach to predict broad-band noise. This is expected to be more difficult, as this corresponds to much lower sound pressure levels.

Bibliography

Each reference is followed by a list of the pages where it is cited.

- [1] ANSYS. *FLUENT 6.3 User Guide*. Fluent Inc., 09 2006. (2, 29, 33, and 95)
- [2] ANSYS. *FLUENT 6.3 User Guide, Section 25.3.1 Spatial Discretization*. Fluent Inc., 09 2006. (33)
- [3] ANSYS. *FLUENT 6.3 User Guide, Section 7.4 Velocity Inlet Boundary Conditions*. Fluent Inc., 09 2006. (32)
- [4] ANSYS. *FLUENT 6.3 User Guide, Section 12.9.2 Filtered Navier-Stokes Equations*. Fluent Inc., 09 2006. (28)
- [5] ANSYS. *FLUENT 6.3 User Guide, Section 7.8 Pressure Outlet Boundary Conditions*. Fluent Inc., 09 2006. (32)
- [6] ANSYS. *FLUENT 6.3 User Guide, Section 12.10.2 Standard Wall Functions*. Fluent Inc., 09 2006. (36, 37, 59, and 64)
- [7] ANSYS. *FLUENT 6.3 User Guide, Section 7.13 Wall Boundary Conditions*. Fluent Inc., 09 2006. (32)
- [8] ANSYS. *GAMBIT 2.4 User's Guide*. ANSYS, 2007. (31 and 97)
- [9] P. W. Bearman and E. D. Obasaju. An experimental study of pressure fluctuations on fixed and oscillating square-cross-section cylinders. *Journal of Fluid Mechanics*, 119:297–321, 1982. (14, 17, 90, 99, and 100)
- [10] D. A. Blake, W. K. Lynch. *Source characterization by correlation techniques*, volume Aeroacoustic Measurements. Springer, 2002. (94)
- [11] W. K. Blake. *Mechanics of flow-induced sound and vibration*. Academic Press, London, 1986. (1 and 98)
- [12] R. Blevins. *Flow-Induced Vibration 2nd edition*, volume Aeroacoustic Measurements. Van Nostrand Reinhold, 1990. (1)

- [13] J. M. Chen and C.-H. Liu. Vortex shedding and surface pressures on a square cylinder at incidence to a uniform air stream. *International Journal of Heat and Fluid Flow*, 20:592–597, 1999. (5, 13, 40, 46, 54, 90, 98, 99, 101, and 111)
- [14] J. Courchesne and A. Laneville. A comparison of correction methods used in the evaluation of drag coefficients measurements for two-dimensional rectangular cylinders. *Journal of Fluids Engineering*, 101: 506–510, 1979. (30, 31, 38, 100, and 109)
- [15] N. Curle. The influence of solid boundaries upon aerodynamic sound. *Proceedings of the Royal Society (London)*, 231:505–514, 1955. (2 and 127)
- [16] J. Dorneanu. Whistling of a rod in cross-flow: effect of angle of attack and reynolds number. Master’s thesis, University of Twente, 2010. (4, 34, 38, 39, 40, 41, 45, 46, 47, 48, 53, 54, 55, 56, 62, 63, 90, 98, 99, 101, 102, 104, 110, 112, 113, 120, 121, 123, and 128)
- [17] A. Dowling and J. Ffowcs Williams. *Sound and sources of sound*. Ellis Horwood Limited, 1983. (116)
- [18] P. Durbin. Near-wall turbulence closure modeling without damping functions. *Theoretical and Computational Fluid Dynamics*, Chap. 3: 1–13, 1991. (26)
- [19] S. Dutta, K. Muralidhar, and P. Panigrahi. Influence of the orientation of a square cylinder on the wake properties. *Experiments in Fluids*, 34: 16–23, 2003. (5)
- [20] H. Fujita. *Private communication*. (121)
- [21] H. Fujita, W. Sha, H. Furutani, and H. Suzuki. Experimental investigations and prediction of aerodynamic sound generated from square cylinders. In *4th AIAA/CEAS Aeroacoustics Conference*, number AIAA-98-2369, 1998. (20, 21, 22, 38, 41, 47, 48, 52, 53, 56, 90, 94, 98, 109, 110, 111, 112, 114, 116, 117, 121, 125, and 127)
- [22] M. Germano, U. Piomelli, P. Moin, and H. Cabot. Dynamic subgrid-scale eddy viscosity model. In *Summer Workshop, Center for Turbulence Research, Stanford, CA*, 1996. (29)
- [23] J. Hinze. *Turbulence*. McGraw-Hill Publishing Co., 1975. (28)

-
- [24] R. Huang, B. Lin, and S. Yen. Time-averaged topological flow patterns and their influence on vortex shedding of a square cylinder in cross-flow at incidence. *Journal of Fluids and Structures*, 26:406–429, 2010. doi: doi:10.1016/j.jfluidstructs.2010.01.003. (5, 8, 9, 10, 11, 12, 13, 66, and 97)
- [25] T. F. Hutcheson, F. V. Brooks. Noise radiation from single and multiple rod configurations. In *12th AIAA/CEAS Aeroacoustics Conference (Cambridge)*, 2006. (20, 21, 90, 100, and 125)
- [26] T. Igarashi. Characteristics of the flow around a square prism. *Bulletin of JSME*, 27(231):1858–1865, 1984. (5, 7, 8, 9, 13, 14, 15, 16, 17, 19, and 21)
- [27] T. Igarashi. Fluid flow and heat transfer around rectangular cylinders (the case of a width/height ratio of a section of 0.33–1.5). *International Journal of Heat and Mass Transfer*, 30, No. 5:893–901, 1987. (90)
- [28] R. Issa. Solution of the implicitly discretised fluid flow equations by operator-splitting. *Journal of Computational Physics*, 62:40–65, 1985. (33)
- [29] B. Kader. Temperature and concentration profiles in fully turbulent boundary layers. *International Journal of Heat and Mass Transfer*, 24(9):1541–1544, 1981. (36)
- [30] N. Kasagi, Y. Tomita, and A. Kuroda. Direct numerical simulation of passive scalar field in a turbulent channel flow. *Journal of Heat Transfer*, 114:598–606, 1992. (36)
- [31] R. B. Kazerooni and S. K. Hannani. Simulation of turbulent flow through porous media employing a v2f model. *Scientia Iranica, Transaction B: Mechanical Engineering*, 16(2):159–167, 2009. (27)
- [32] W.-W. Kim and S. Menon. Application of the localized dynamic subgrid-scale model to turbulent wall-bounded flows. *Technical Report AIAA-97-0210, American Institute of Aeronautics and Astronautics, 35th Aerospace Sciences Meeting, Reno, NV*, 1997. (29)
- [33] C. Knisely. Strouhal numbers of rectangular cylinders at incidence: a review and new data. *Journal of Fluids and Structures*, 4:371–393, 1990. (5, 13, 19, 20, 38, 41, 45, 47, 48, 53, 55, 56, 90, 99, 102, 104, 109, 110, 111, and 112)

- [34] A. Kolmogorov. Dissipation of energy in the locally isotropic turbulence. *Proceedings of the USSR Academy of Sciences*, 32:16–18, 1941. (26 and 27)
- [35] D. F. Kurtulus, F. Scarano, and L. David. Unsteady aerodynamic forces estimation on a square cylinder by tr-piv. *Experiments in Fluids*, 42:185–196, 2007. doi: DOI10.1007/s00348-006-0228-4. (43, 48, 50, 58, 62, 63, 90, and 97)
- [36] L. Larchevêque, P. Sagaut, and O. Labbé. Large eddy simulation of subsonic cavity flow including asymmetric three-dimensional effects. *Journal of Fluid Mechanics*, 577:105–126, 2007. (4)
- [37] M. J. Lighthill. On sound generated aerodynamically i: General theory. *Proceedings of the Royal Society (London)*, 211:564–587, 1952. (2 and 115)
- [38] M. J. Lighthill. On sound generated aerodynamically ii: Turbulence as a source of sound. *Proceedings of the Royal Society (London)*, 222:1–32, 1954. (2)
- [39] D. Lyn, S. Einav, W. Rodi, and J. Park. A laser-doppler velocimetry study of the ensemble-averaged characteristics of the turbulent near wake of a square cylinder. *Journal of Fluid Mechanics*, 304:285–319, 1995. (5, 13, 39, 42, 43, 48, 49, 50, 57, and 58)
- [40] P. Martinez-Lera, J. Christophe, C. Schram, and J. Anthoine. Effect of the boundary conditions and source truncation in the prediction of flow-generated sound. 2007. (97)
- [41] P. Moin and K. Mahesh. Direct numerical simulation: a tool in turbulence research. *Annual Review of Fluid Mechanics*, 30:539–578, 1998. (26)
- [42] A. Mueller, J. Anthoine, and P. Rambaud. Vortex shedding in a confined laminar flow past a square cylinder. In *ECCOMAS*, 2008. (2, 30, and 97)
- [43] F. Nicoud. Unsteady flows modeling and computation. *VKI Lecture Series*, 09, 2007. (29)
- [44] F. Nicoud, F. Ducros. Subgrid-scale stress modelling based on the square of the velocity gradient tensor. *Flow, Turbulence and Combustion*, 62:183–200, 1999. (29 and 95)

-
- [45] C. Norberg. Flow around rectangular cylinders: Pressure forces and wake frequencies. *Journal of Wind Engineering and Industrial Aerodynamics*, 49:187–196, 1993. (5, 19, 38, 41, 45, 55, 90, 98, 99, 102, 104, and 112)
- [46] S. Oerlemans. *Private communication*. NLR. (102)
- [47] A. Okajima. Strouhal numbers of rectangular cylinders. *Journal of Fluid Mechanics*, 123:379–398, 1982. (90 and 98)
- [48] Y. Otsuki. (in japanese). In *5th Symp. on Wind Effects on Structures*, page 169, 1978. (15)
- [49] O. M. Phillips. The intensity of aeolian tones. 1(06):607–624, December 1956. (20 and 44)
- [50] L. Prandtl. *Verhandlungen des dritten internationalen Mathematiker-Kongresses in Heidelberg*, page 484, 1904. (34)
- [51] W. Rodi. Comparison of les and rans calculations of the flow around bluff bodies. *Journal of Wind Engineering and Industrial Aerodynamics*, 69-71:55–75, 1997. (5 and 19)
- [52] E. Roosenboom. Experimental analysis of the flow around a cylinder with a square cross-section. Master’s thesis, TUDelft, 2005. (4, 5, 13, 15, 64, 65, 66, 67, 69, 70, 71, 72, 73, 74, 75, 76, 77, 78, 79, 80, 83, 85, 87, 88, 90, and 128)
- [53] P. Sagaut. *Large Eddy Simulation for Incompressible Flows: An Introduction, 3rd edition*. Springer, 2005. (27)
- [54] M. Sarioglu, Y. Akansu, and T. Yavuz. Control of flow around square cylinders at incidence by using a rod. *AIAA Journal*, vol. 43, No. 7: 1419–1426, 2005. (13 and 14)
- [55] F. Scarano and M. Riethmuller. Iterative multigrid approach in piv image processing with discrete window offset. *Experiments in Fluids*, 26:513–523, 1999. (64)
- [56] H. Schlichting. *Boundary-Layer Theory, 7th edition*. 1979. (4 and 34)
- [57] J. Smagorinsky. General circulation experiments with the primitive equations. i. the basic experiment. *Month. Wea. Rev.*, 91:99–164, 1963. (29)

- [58] A. Sohankar, L. Davidson, and C. Norberg. Large eddy simulation of flow past a square cylinder: Comparison of different subgrid scale models. *Journal of Fluids Engineering*, 122:39–47, 2000. doi: <http://dx.doi.org/10.1115/1.483224>. (5, 19, 39, 42, 43, 48, 49, 50, 57, 58, 90, and 100)
- [59] V. Strouhal. Über eine besondere art der tonerregung. *Annalen der Physik und Chemie*, October:216–251, 1878. (3 and 89)
- [60] T. Tamura and T. Miyagi. The effect of turbulence on aeroacoustic forces on a square cylinder with various corner shapes. *Journal of Wind Engineering and Industrial Aerodynamics*, 83:135–145, 1999. (5, 13, 16, 17, 18, 19, and 20)
- [61] I. Taylor and M. Vezza. Prediction of unsteady flow around square and rectangular section cylinders using a discrete vortex method. *Journal of Wind Engineering and Industrial Aerodynamics*, 82:247–269, 1999. (5 and 90)
- [62] T. Uffinger, S. Becker, and A. Delgado. Investigations of the flow field around different wall-mounted square cylinder stump geometries. In *14th Int Symp on Applications of Laser Techniques to Fluid Mechanics, Lisbon, Portugal*, 2008. (20 and 21)
- [63] E. van der Weide. Private communication. *University of Twente*. (26, 31, 34, 46, 48, 64, 67, 69, 70, 71, 72, 73, 74, 75, 76, 77, 78, 79, 80, 90, 99, 110, 111, 112, and 121)
- [64] B. Vickery. Fluctuating lift and drag on a long cylinder of square cross-section in a smooth and turbulent stream. *Journal of Fluid Mechanics*, 25:481–494, 1966. (5, 18, 19, and 20)
- [65] C. Wagner, T. Huttl, and P. Sagaut. *Large-Eddy Simulation for Acoustics*. Cambridge University Press, 2007. (37)
- [66] M. Wang, J. B. Freund, and S. K. Lele. Computational prediction of flow-generated sound. *Annual Review of Fluid Mechanics*, 38:483–512, 2006. (89)
- [67] D. Wilcox. *Turbulence Modeling for CFD, 2nd edition*. DCW Industries, Inc., 2004. (26 and 35)

Glossary

Each entry is followed by the list of the pages where it is referred.

α

Angle of attack [*deg*] [5, 7-9]

α_{cr}

Critical angle of attack [*deg*] [i, 8, 13]

a

Speed of sound [*m/s*] [39]

C_{pb}

Base pressure coefficient (pressure coefficient at the middle of the rear side of the rod) [-] [17]

C_d

Drag coefficient [-] [15]

$C_{d_{rms}}$

Root mean square of drag coefficient [-] [18, 19]

C_l

Lift coefficient [-] [15]

$C_{l_{rms}}$

Root mean square of lift coefficient [-] [18]

C_p

Pressure coefficient [-] [6, 13]

C_p'

Fluctuating pressure coefficient [-] [8]

γ	Spanwise correlation length coefficient [-] [6, 21]
D	Rod width [m] [7]
D_{proj}	Rod width projected in wind direction [m] [19]
$\delta(x_i)$	Dirac delta function [-] [118]
η	Kolmogorov scale [-] [27]
f	Dominating vortex shedding frequency [Hz] [19]
H	Computational domain dimension in direction x_2 [m] [30]
k	Wave number [-] [27]
L	Computational domain dimension in direction x_3 , or rod length [m] [7, 30]
L^*	Length of the rod taking into account the correction of sound reflected from the side-walls [m] [118]
L_{eff}	Effective length of the rod [m] [118]
M	Mach number [-] [39]

ν	Kinematic viscosity [m^2/s] [25]
ν_t	Subgrid-scale turbulent viscosity [m^2/s] [28]
$p(\vec{x}, t)$	Pressure [Pa] [25]
p_I	Pressure signal registered by microphone I [Pa] [96]
p_{II}	Pressure signal registered by microphone II [Pa] [96]
p_{ref}	Reference pressure [Pa] [39]
p_{rms}	Root mean square amplitude of pressure fluctuations [Pa] [96]
Re_D	Reynolds number based on inlet velocity and rod width D [-] [6]
ρ	Density [kg/m^3] [25]
r	Distance from rod axis to the microphone [m] [39]
r_r	Anechoic room reverberation radius [m] [95]
S	Surface coordinate [m] [38]
SPL	Sound pressure level [dB] [21]

St

Strouhal number based on inlet velocity and projected width of the rod ($St = fD_{proj}/U_o$) [-] [20]

St_D

Strouhal number based on inlet velocity and width of the rod ($St = fD/U_o$) [-] [6, 20]

St_b

Strouhal number based on velocity along free streamlineat separation point and projected width of the rod ($St = fD_{proj}/U_s$) [-] [20]

\bar{S}_{ij}

Rate of strain tensor for the resolved scale [m/s] [28]

σ_i

Line force density [N/m] [118]

T_{60}

Anechoic room reverberation time [s] [95]

τ_{ij}

Subgrid scale stress [Pa] [28]

t

Time [s] [25]

U_o

Inlet velocity [m/s] [19]

U_s

Velocity along free streamline at separation point, $U_s = U_o\sqrt{1 - C_{pb}}$ [m/s] [19]

\bar{u}_i

Resolved velocity vector component in direction i [m/s] [28]

\overline{u}_i

Average velocity vector component in direction i [m/s] [26]

u'_i	Fluctuating velocity vector component in direction i [m/s] [26]
$u_i(\vec{x}, t)$	Velocity vector component in direction i [m/s] [25]
U_{mean}	Mean streamwise velocity [m/s] [39]
U_{rms}	Root mean square of streamwise velocity [m/s] [39]
V_{rms}	Root mean square of velocity in direction x_2 [m/s] [39]
W_{rms}	Root mean square of velocity in spanwise direction x_3 [m/s] [39, 42]
X_b	Length of the buffer zone [m] [30]
X_{down}	Computational domain dimension downstream the rod [m] [30]
X_{up}	Computational domain dimension upstream the rod [m] [30]
\vec{x}_I	Position of microphone I [Pa] [95]
\vec{x}_{II}	Position of microphone II [Pa] [95]
x_1	Streamwise coordinate [m] [7]
x_2	Transverse coordinate [m] [7]
x_3	Spanwise coordinate [m] [7]

Summary

We consider the prediction of the flow around a square rod as a generic bluff body at low Mach number (below 0.3) and high Reynolds number (above 5000) and the corresponding tonal noise. Instability of such flow is crucial for potential mechanical vibrations and noise production.

Due to the presence of sharp edges the flow separation along a square rod is relatively easy to predict. The flow remains however quite complex as it involves re-attachment and secondary vortex shedding. Depending on the angle of attack, between the main flow direction and the bottom side wall of the rod, three flow types are observed. Firstly at low angles of attack the flow separating from both upstream edges forms a periodic vortex street in the wake. Secondly above a critical angle of attack around 13° , the flow re-attaches to the bottom side wall. The wake is dominated by vortex shedding from the upper front edge and the lower downstream edge. At 45° the stagnation point is on the front edge and flow separation occurs from the two lateral edges. In the literature the wake is reported to display a von Kàrmàn vortex street corresponding to a whistling mode. For angle of attack between 25° and 45° , we observe experimentally a second mode in which the wake is stable and the rod does not whistle. We call this the silent mode. One can switch from one mode to the other by perturbing the flow in front or behind the rod.

Direct Numerical Simulation of the radiated sound is extremely difficult and certainly not feasible for industrial applications. We assess the potential of a hybrid method in which the flow is modelled by means of an incompressible Large Eddy Simulation (LES). The flow data is then used to estimate the sound radiation by using the Lighthill-Curle aeroacoustical analogy. Incompressible resolved LES obtained with a commercial code provides a fair prediction of the flow if the full length of the rod is taken into account including the side walls used to support the rod in the experiments. Combining the LES results with the aero-acoustical analogy provides a prediction of observed tonal noise within 2 dB. The prediction of broad band noise was not considered.

The use of quasi two-dimensional LES calculations or two-dimensional Unsteady-Reynolds Averaged Navier Stokes (URANS) models appears to

be much less accurate. These LES calculations are unfortunately still much too demanding to allow a systematic parametric study. They also do not capture the observed silent mode.

Curriculum Vitae

Born on 24.09.1978 in Cieszyn, Poland

- Oct 2006 – Jun 2011:
PhD Candidate. Thesis title: *Large Eddy Simulation of cross-flow around a square rod at incidence with application to tonal noise prediction.*
von Karman Institute for Fluid Dynamics, Belgium
Univeristy of Twente, The Netherlands.
- Oct 2005 – Jun 2006
Post-graduate diploma course in fluid mechanics research. Individual project: *Study of Turbulent Transport of a Passive Scalar Applying Large Eddy Simulation.*
von Karman Institute for Fluid Dynamics, Belgium.
- Sept 2003 – Aug 2005
Postgraduate fellow in the Detector Cooling section, CFD Studies team.
CERN Switzerland
- Jan 2002 – Aug 2003
Technical Student internship. Master thesis preparation. Detector Cooling section, CFD Studies team.
CERN Switzerland
- Oct 1997 – Feb 2003
MSc. degree in Computational Mechanics in Environmental Engineering. Thesis title: *Thermal analysis of the ALICE L3 magnet environment using StarCD code.*
Cracov University of Technology, Poland

Publications:

- A. Mueller, J. Anthoine and P. Ramabaud, Vortex shedding in a confined laminar flow past a square cylinder, ECCOMAS 2008, June 30 - July 5, 2008, Venice, Italy

- P. Martinez-Lera, A. Mueller, C. Schram, P. Rambaud, J. Anthoine, W. Desmet, Robust aeroacoustic computations based on Curle's and Powell's analogies, ISMA 2008 Leuven

Acknowledgements

This work would not be possible without the contribution and support from many people.

First of all I would like to thank Mico for his ideas and constant encouragement in work and writing. Words cannot describe how grateful I am. You are the most patient person that I know.

The suggestions from prof. Hoeijmakers, prof. Lopez and dr. van der Weide helped to improve the contents of this thesis and 'un-Polish' my English. Prof. Hoeijmakers supported morally and financially the experiment (University of Twente), which was in line with the work of this thesis.

Here again, thank you Mico for supervising two students that performed measurements: Justin Dorneanu (pressure and acoustic measurements) and Imanuel Geesing (hot wire correlation measurement). This experiment was supported by the technicians at UTwente: Herman Stobbe, Paul Niel, Wouter den Breeijen. During the experimental campaign dr. van der Weide kindly provided the uRANS results which were used for comparison in this thesis.

The set-up for the experiment was built at the von Karman Institute with the support of Guillaume Diquas and Karl Colussa.

I would like to thank prof. Fulvio Scarano and his team for providing essential PIV data and the discussions I had with him.

My PhD started with the support of prof. Jerome Anthoine, when he left VKI I was supervised by prof. Patrick Rambaud. To both of them go my sincere thanks for supervision and special arrangements that allowed me to combine my work with family life.

During this PhD I had a unique opportunity to take part in the European project AETHER led by prof. Christophe Schram who was the main engine and source of enthusiasm to many young researchers that I met during that time. Here I should also mention the Aetherians: Devis, Manohar, Paula, Kerstin, Thomas, Lilla... It was a pleasure to meet you and exchange ideas.

LMS provided the computer cluster on which I was able to perform my simulations. This cluster was managed by dr. Raimondo Giammanco of VKI who made always sure that everything was working smoothly.

Finally my greatest thanks go to my family. At first to my parents that provided me with happy childhood, freedom and education - Mamo, Tato -

dziękuję za szczęśliwe dzieciństwo, swobodę i edukację!

Tiago, it is not very often that a mother of two young children finishes her PhD, you are the best partner! Thank you for your loving support and patience. And my children, Lucas and Marta, you make me proud! I need to acknowledge your grandmother Vóvó Rute for helping me to take care about you during the last month of writing my thesis - obrigada.

The work is supported through the Marie Curie Research Training Network Project AETHER (contract no MRTN-CT-2006-035713).